# UNIVERSITY OF NAPLES FEDERICO II

DEPARTMENT OF INDUSTRIAL ENGINEERING


PH.D. COURSE IN INDUSTRIAL ENGINEERING

COORDINATOR PROF. MICHELE GRASSI

*XXXV CYCLE*

*PH.D. THESIS*

# ADVANCED ASTRODYNAMICS MODELS AND APPROACHES FOR SPACE SURVEILLANCE AND EXPLORATION

By


Giorgio Isoletta


Supervisors:

Prof. Roberto Opromolla

Prof. Giancarmine Fasano

*A volte manca il coraggio*
*di avere paura*
*altre volte è più dura*
*se il coraggio ce l'hai*

*Ho lasciato un messaggio*
*scritto sul pavimento*
*dice "Spero tu possa*
*non leggermi mai."*

# Table of contents

# Abstract

The main objective of this PhD activity is the development of innovative astrodynamics techniques to enable advanced functionalities for a wide range of applications in the space domain. In this respect, two different research areas have been addressed, one related to the development of algorithms to support Space Surveillance and Tracking (SST) services, the other related to the space exploration domain, and, in particular to investigating the potential of aerocapture maneuvering for future Mars missions. As different as these applications could seem, the activity has the general purpose to provide tools and algorithms to deal with astrodynamics problems.

In the SST context, operations involving detection and monitoring of space objects as well as avoidance of possible collision between them require the accurate knowledge of the objects' position over time, achievable only by means of numerical propagators when frequent enough measurements from ground-/space-based sensors are not available. Indeed, a fully configurable numerical orbit propagation tool is presented here, which includes the main Earth orbital perturbation and exploits an high-order Runge-Kutta scheme to solve the perturbed equations of motion. The developed propagator is conceived to be easily coupled to other algorithms to support various SST tasks. In this perspective, the main contribution of this thesis is the development and performance assessment of an innovative approach to evaluate the medium-term collision frequency for space objects in LEO, taking the propagation uncertainties into account. At the same time, a novel algorithm is also proposed to estimate the position errors coming from environmental and object-related uncertainties, based on relative motion equations. Furthermore, the modularity of the proposed orbital propagation environment makes it a useful tool to support other SST applications. To demonstrate this point, the propagator is integrated within algorithmic architectures to perform calibration of ground-based sensors and to carry out coverage analysis of satellites over areas of interest to support sensor tasking and Recognized Space Picture activities respectively.

As regards the Space Exploration context, the research activity focused on the investigation of the feasibility of Mars aerocapture for small satellites exploiting the adaptable aperture of a particular deployable drag device. The study, which has been carried out first for a simplified 2D scenario and then for a complete 3D Mars mission, aims at understanding the conditions leading to successful aerocapture and at assessing the impact of the main uncertainties on its success.

**Keywords**: astrodynamics; orbit propagation; space situational awareness; space surveillance and tracking; collision risk assessment; uncertainty estimation; sensor calibration; space exploration; aerocapture

# 1. Introduction

This PhD activity has the main goal to develop innovative astrodynamics models and approaches for a wide range of applications in the space domain. The general objective is to provide tools and algorithms to deal with various astrodynamics problems. In this respect, two different research areas have been addressed, one related to the development of algorithms to support Space Surveillance and Tracking (SST) services, the other related to the space exploration domain, and, in particular to investigating the potential of aerocapture maneuvering for future Mars missions.

## 1.1 Space Surveillance and Tracking context

The region of space around the Earth is getting increasingly crowded and is becoming a fast-changing environment, with more and more causes for rapid increment of the number of orbiting objects, e.g., fragmentation events and launches of many large satellite constellations. Up to now, it is estimated that around 36000 trackable debris objects larger than 10 cm, and over 1 million of debris objects larger than 1 cm, are orbiting Earth [1].

Clearly, this over-population of the circumterrestrial space environment can produce a risk not only for space-based assets, which are constantly threatened by collisions with other operational spacecraft or debris objects, but also for the safety of assets and people on ground, which may be endangered by re-entry of large uncontrolled objects. Mitigating these risks means to acquire the capability to survey and track such objects and to provide the resulting information to a variety of stakeholders, reaching a broad knowledge of the near-space environment, with the overall objective of achieving harmonization of space activities on a global level. In this light, Space Traffic Management (STM) represents a key concept, consisting in the planning, coordination and synchronization of activities to make space operations more safe, stable and sustainable. In turn, STM systems rely on the Space Situational

Awareness (SSA) of the space operating environment [2]. Several SSA programs arose in the last years [3], also following the space debris mitigation guidelines defined by the Committee on the Peaceful Uses of Outer Space (COPUOS) [4]. The European Space Agency (ESA) lists three segments of knowledge in SSA [5]:

- Space surveillance and tracking (SST), to monitor objects in Earth orbit including active and inactive satellites, spent rocket bodies and other debris fragments (either breakup-event related or mission-related);
- Space weather (SWE) to monitor conditions at the Sun's surface and in the solar wind, and in Earth's magnetosphere, ionosphere and thermosphere, that can affect space-borne and ground-based infrastructures or endanger human life or health;
- Near-Earth objects (NEO), to detect natural objects that can potentially impact Earth and cause damage.

In order to prevent collisions between space objects from happening and to perform re-entry analysis adequately, special attention is paid to the SST segment. Within the SST framework, orbit propagation is crucial in many activities, especially those related to collision risk assessment (CRA), in which high accuracy predictions of the objects' orbital states are required. Unfortunately, propagation accuracy is affected by several sources of errors, arising from uncertainties depending on object-related and environmental factors, especially in Low-Earth Orbit (LEO) scenarios. First, orbital perturbation modelling represents a major issue, mostly concerning the estimation of the Earth's atmospheric density. Indeed, under the same orbital conditions, different atmospheric models output different density values, which can undergo additional significant variations due to the solar activity. Another critical source of uncertainty is related to the accuracy in the knowledge of the physical parameters of space objects, such as the area-to-mass ratio ($A/M$), typically unknown for debris, also due to the limits of ground-based sensors on the minimum detectable size. In this context, the uncertainty evaluation process consists in assessing how the input uncertainties on the environment and the objects' characteristics affect the propagation error in output as a function of propagation time.

Clearly, the good outcome of a collision risk analysis is strongly related to the uncertainties involved and, therefore, to the magnitude of the position and velocity errors accumulated when propagating the space objects' trajectories. Collision risk assessment is performed by various methods, both covariance and non-covariance based. While the former represent the standard approaches to evaluate the probability of collisions between two objects in short-term encounter [6], the latter, such as Orbit Trace and Cube methods, are mainly used to assess the collision rates of assets of interest in long-term propagation scenarios, also considering large populations [7], [8]. In particular, the Cube method seems to be the most suitable to deal with close approach frequency in medium/long-term scenarios, being easy to couple with numerical orbit propagators. Its flexibility and ease of integration, make it a useful algorithm also for medium-term collision risk analyses, although it does not consider the uncertainties and, thus, the resulting errors in the estimation of objects' state vector.

Within this PhD thesis, a numerical orbit propagation environment has been developed. The building of an in-house orbit propagator, fully customizable and easy to integrate with other algorithms, has represented a starting point and a useful tool to address several SST applications. Indeed, since the global purpose lies in the implementation of innovative astrodynamics models to be used in various current and future activities, one key outcome of this research work is the design, development and performance assessment of algorithms for the evaluation of the medium-term collision frequency for space objects in LEO, taking the environmental and object-related propagation uncertainties into account. The new algorithm, called Uncertainty-aware Cube method, is a modified version of the Cube and it can be seen as an hybrid between covariance-based and non-covariance-based methods. This approach aims at providing a more realistic picture of the potential conjunctions that the objects could experience in the near future, being helpful also in operative context, e.g., to foresee in advance which assets can be most endangered in the next month, labelling them at different levels of priority or to support sensor tasking focusing the attention on potentially dangerous debris objects. Furthermore, for the uncertainty evaluation process, an algorithm has been developed and integrated with the Uncertainty-aware Cube to estimate the position errors, based on the Hill's equation expressed in terms of differential orbital parameters (DOPs).

The development of a configurable and modular propagation environment has enabled the possibility to explore other SST applications, thus tailoring the propagation and perturbation settings depending on the different operational scenario. For instance, algorithms have been developed to perform ground-based sensor calibration, implementing an iterative method to compute the sensor time bias. Also an application related to the Recognized Space Picture (RSP) service has been investigated, developing an algorithm to carry out coverage analysis of a satellite over an user-defined Area of Interest (AOI).

## 1.2 Aerocapture technique for Space Exploration

The growing scientific interest in Mars exploration and the recently renewed plans for large-scale unmanned and manned missions to the Red Planet have led to several studies on the feasibility of aerocapture for orbit insertion with aerodynamic decelerators, such as deployable or inflatable drag devices [9]–[11]. Aerocapture is an aero-assisted orbital maneuver that exploits the drag generated during a single atmospheric passage to decelerate a probe and transfer it from a hyperbolic trajectory to an elliptical orbit. For missions to planet with an appreciable atmosphere, the benefit of this technique lies in its intrinsic time and propellant savings [12]. Since the thermal shielding weighs less than the propellant needed to perform an orbit insertion maneuver, opting for aerocapture leads in general to a larger payload mass and, therefore, a potentially higher scientific return [13].

The state-of-the-art method for Mars orbit insertion (MOI) consists in adopting a large propulsive maneuver to insert the spacecraft into a highly elliptical orbit around Mars. The target orbit is then reached by means of additional burns or with aerobraking. The first Mars missions (e.g., Mariner9 [14]) reached the science orbits with all-propulsive strategies corresponding to a total maneuver cost of about 1.6 km/s. In more recent missions, such as Mars Global Surveyor (MGS) in 1996 [15] and Mars Reconnaissance Orbiter (MRO) in 2005 [16], a MOI maneuver of 1 km/s was supplemented by aerobraking campaigns of several months to circularize the orbit and reduce the orbital period. So, a significant amount of propellant mass must be stored on board to employ this strategy, which constitute a challenging constraint from an operational point of view. In this respect, the aerocapture approach fits particularly well for small satellites, since it allows overcoming the challenges associated to the design of an adequate propulsion system. Indeed, not only no chemical propulsion system capable to perform the maneuver needed for propulsive MOI currently exists for small platforms, but the required propellant mass fraction would result in on-board storage issues [17], [18].

However, despite all its potential benefits, aerocapture has never been implemented to date to perform the MOI, because of the uncertainties in Mars' atmospheric density and its variation, as well as navigation errors [19]. Therefore, the purpose of this part of the thesis is to investigate the feasibility of aerocapture at Mars for small satellites employing a deployable drag device, whose aperture can be modulated in flight, and to assess the effects of the uncertainties on the success of the maneuver. The numerical orbital propagator has been modified ad hoc and simplified to propagate the trajectory of the spacecraft under Mars gravitational attraction and within Mars atmosphere. First, a parametric bidimensional analysis is considered, for which a wide range of uncertainty levels in the atmospheric density and ballistic coefficient are taken into account. Then, an application to real mission scenario is discussed, including navigation errors in form of errors in the targeting maneuver performed at the limit of the sphere of influence of Mars.

## 1.3 Thesis organization

The thesis is organized as follows:

- Chapter 2 presents an overview of the state of the art of SST applications, with a particular focus on the applications of interest for this thesis. A section is dedicated to the collision risk assessment, to discuss advantages and disadvantages of both covariance and non-covariance-based methods.

Furthermore, brief introduction to other SST tasks of interest within this thesis are presented, such as the modelling of propagation uncertainties, the sensor tasking and sensor calibration problem and the definition of the RSP.

- Chapter 3 introduces the numerical orbit propagation environment. First, a brief review of orbit propagation is provided, then the implementation and validation of the developed orbit propagator are described, paying special attention to the perturbation modelling. Finally, the accuracy-computational cost trade-off is discussed, also showing an application to propagation of fragments coming from a simulated breakup event.

- Chapter 4 presents the algorithms developed for the SST applications of interest and their performance assessment. First, the concept and implementation of the Uncertainty-aware Cube method are illustrated and the results of some synthetically generated LEO scenarios are shown and discussed. Later, the coupled uncertainty evaluation algorithm is presented, together with the discussion of some test cases. Then, the Chapter continues with the description of the sensor calibration tool and the discussion of some calibration examples. Finally, as regards the RSP context, the algorithm developed for the analysis of overflight of an AOI is presented and results are shown.

- Chapter 5 is dedicated to the feasibility study of Mars aerocapture. After a brief literature review, the aerocapture modelling and implementation are described and the applications to Mars scenarios are discussed, starting from general considerations (i.e., bi-dimensional analysis) to finally apply the method to a simulated mission scenario (i.e., three-dimensional analysis).

- Chapter 6 contains the conclusions, to summarize the results and anticipate further developments of the research activity.

# 2. State of the art of Space Surveillance and Tracking applications

Regarding the space-based situation, the guidelines defined by COPUOS provide suggestions on how to limit the probability of accidental collisions and explosions in orbit. Within this framework, collisions between space objects are among the most dangerous and potentially catastrophic fragmentation events, since they can produce a large number of debris, which in turn could pose a risk to other objects, with a consequent cascading effect. The phenomenon of collisional cascading, known in the literature as “Kessler’s syndrome”, was initially theorized by Kessler in 1978 [20] and then widely discussed and demonstrated in the following years [21], [22] also by means of many space debris evolutionary models [23]–[26]. It is clear that, in such a risky environment, it is necessary not only to protect the space assets of interest, i.e., operative satellites, but also to monitor with growing attention the possible conjunctions between debris objects, in order to avoid the space around our planet becoming inhospitable and many orbital regions becoming unsuitable for human activity, especially in LEO [27].

That’s why, in the last years, growing attention is given to the SST segment, which is in charge of monitoring objects in Earth orbit, i.e., active satellites, spent rocket bodies and other debris fragments, and the related fragmentation events. In Europe, the SST Support Framework was established by the European Union (EU) in 2014, entailing the creation of an SST Consortium (EU SST) of EU member states fusing their respective SST capabilities. Currently, the Consortium includes 15 EU member states: Italy, France, Germany, Poland, Portugal, Romania, Spain, Austria, Czech Republic, Denmark, Finland, Greece, Latvia, the Netherlands and Sweden. Three types of services are provided to users:

- Re-Entry Analysis (RE) consists of risk assessment of uncontrolled re-entry of dangerous space objects into the Earth’s atmosphere and generation of related information, including estimation of timeframe and likely location of possible impact.

- Fragmentation Analysis (FG) consists of the detection and characterization of in-orbit fragmentations due to explosions or collisions. It provides short-term information, such as detected number of objects and their size, as well as medium-term/long-term information including the fragments cloud evolution.
- Collision Avoidance (CA) consists of risk assessment of collisions between space objects and the generation of collision avoidance alerts, thus playing the main role in preventing the *Kessler syndrome* scenario from happening.

Within the Italian context, the Italian Space Agency (ASI) serves as National Entity, in a group including Italian Ministry of Defense and the Italian National Institute for Astrophysics (INAF). Italy is responsible for the re-entry and fragmentation services, which are carried out by Italian SST Operation Centre (ISOC). It is worth noting that Italy plays a prominent role also in the ESA’s SSA/Space Safety program, being the first country to establish an asteroid risk monitoring system, with ASI supporting the operations of the NEO Coordination Center established at the European Space Research Institute (ESRIN) in Frascati.

The rest of the chapter provides, first, a description of the existing methods to perform collision risk assessment, focusing on their suitability for medium-term applications. Then, an overview of the techniques to model propagation uncertainty is presented, followed by a description of the problem of sensor tasking to introduce the sensor calibration application. Finally, a brief mention to the RSP concept is provided.

## 2.1 Collision Risk Assessment

In the ambit of the collision risk assessment, two main groups of methods can be distinguished: covariance-based and non-covariance-based methods. The first ones represent the traditional approach to evaluate the risk: they examine the predicted miss distance (MD) between two objects at their closest point of approach (CPA), determining if its value is “acceptable” or not. It is clear that, in this context, there is not a value that is “acceptable” in absolute terms, but it depends on the magnitude of the uncertainties in the knowledge of the positions of the two objects. If, for instance, the MD value is small, but the position uncertainties are sufficiently smaller than the MD, one can consider the close approach to be safe from a potential collision. On the other hand, if the uncertainties are too large, it could be difficult to exclude a possible collision, even in presence of high MD values. For this reason, when computing the probability of collision (PC) between two objects, the uncertainties, which can be expressed mathematically as covariance matrices, must also be considered. To better understand the relationship between the probability of collision, the MD and the position covariance, Figure 1 reports the graphical representation proposed by Hejduk, Snow and Newman [28]. Here, the PC is plotted against the ratio of covariance size to MD and two different regions can be distinguished, i.e., the robust region and the dilution region. The plot is useful to visualize the behavior of the PC during a typical conjunction's event scenario, assuming constant MD. Indeed, when a possible conjunction event is detected, in general 5-7 days before the time of closest approach (TCA), the covariance size is large because of the long propagation time to TCA, so the PC value is small and the event is in the dilution region. After some days, more accurate information could be available thanks to additional tracking and the propagation time to TCA is shorter, thus reducing the size of the covariances. Therefore, when the MD remains the same or tends to have small variations, the PC increases and reaches a peak. Finally, when approaching TCA, the covariances shrink, the event is in the robust region and the PC drops off. This represent the common process, but clearly, if a collision is actually detected and no remediation is implemented, the PC would grow up to unity.

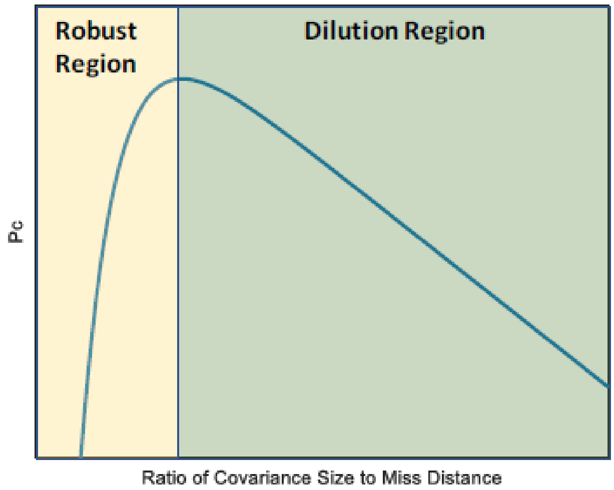


Figure 1 Probability of collision vs the ratio of covariance size to MD [28]

Over the years, several methods to assess the collision probabilities have been developed [29]–[34], but they all start from common assumptions made on the objects and on their position and velocity uncertainties [6].

Although these covariance-based methods proved to be rather accurate in the evaluation of the collision probabilities between two bodies, they have two main drawbacks. They can be quite computationally heavy and they need much information to be exploited. In fact, uncertainty estimation and, thus, the calculation of the covariance matrices, could be a not straightforward process for some objects, like space debris. Moreover, challenges can also arise in the propagation of the covariance matrices over a medium/long-term period, on the one hand for the computational burden that an accurate propagation could imply, on the other for uncertainty realism issues, when trying to linearize the problem [35], [36].

In this perspective, non-covariance-based methods have been developed, in particular the Cube method and the Orbit Trace method. The latter is based on a method developed by E.J. Öpik [37], originally implemented to evaluate the collision rates between asteroids and other celestial bodies. The method was initially applicable only to objects on circular orbits, but then it was generalized by first Wetherill [38] and later Kessler [7], introducing the possibility of dealing with non-circular orbits and overcoming some singularity problems due to specific close-encounter geometries.

Customized versions of this algorithm have been implemented in several space debris evolutionary models, such as the Long-term Utility for Collision Analysis model (LUCA, and LUCA-2) [39], [40], the Italian Space Debris Mitigation long-term analysis program (SDM) [41] as well as the Aerospace Debris Environment Projection Tool (ADEPT) by Aerospace Corporation [42], [43]. Basically, in the Orbit Trace, the collision probability between two objects is proportional to the time interval that each object spends in the region around the orbits' intersection point. The main assumption of this method is that the semimajor axis, $a$, the eccentricity, $e$, and the inclination, $i$, of each object are fixed, while the other Keplerian orbital parameters are distributed randomly between 0 and $2\pi$. This assumption ceases to be valid when considering objects which experience strong non conservative forces, with fast-changing semimajor axis and eccentricity.

In this respect, the Cube method was initially designed to overcome the limitations of Orbit Trace, building an algorithm which can be easily coupled to numerical orbital propagators, thus considering the updated orbital elements of the objects as they evolve in time. While the successive implementations of Orbit Trace have considered this aspect, the Cube method still provides significant advantage in dealing with large populations, as it requires a lower computational time [8], [44]. The work logic of Cube is quite simple: a region of space around the Earth is divided into cubes of fixed dimension and, at each time instant of interest, it is checked whether two or more objects are in the same cube. If so, the collision probability is computed by means of the particle-in-the-box equation [8]. Cube has also been implemented in orbital debris evolutionary models, such as LEO-to-GEO Environment Debris model (LEGEND) [25] and the Space Objects Long-term Evolution Model (SOLEM) [45] in a modified version, as well as for the assessment of close approach frequency for satellites in large constellations [46]. Thus, up to now its application has been limited to long-term propagation scenarios, the interest being in estimating the collision rates over periods of many years.

### 2.1.1 Review of the Cube method

The Cube method is a non-covariance-based conjunction analysis method, initially intended to estimate the long-term collision probabilities by means of uniform sampling in time of an N-body system [8], [44]. It was included in the National Aeronautics and Space Administration (NASA) orbital debris evolutionary model LEGEND as a three-dimensional collision probabilities evaluation module. The main output of the algorithm is the number of collisions between objects over a long period of time. The assumption of the Cube is that two objects could collide only when they are within a small volume element. Therefore, the three-dimensional space is divided into many cubes, whose dimension can be user-defined. Given a time interval of interest and the timestep of the analysis, at each time instant the state vectors of the objects are calculated and the cubes in which the objects are placed are uniquely identified. The collision rate between objects $i$ and $j$, $P_{i,j}$, can be evaluated, when two objects occupy the same cube, as:

$$P_{i,j} = s_i s_j V_{rel} \sigma dU \tag{2.1}$$

where $s_i$ and $s_j$ are the spatial densities of the objects in the cube, $V_{rel}$ is the relative velocity, $\sigma$ is the collision cross-sectional area and $dU$ is the cube volume. The spatial densities are considered as $1/dU$ for co-located objects and the collision cross-sectional area, $\sigma$, can be expressed as $\pi(r_i + r_j)^2$, with $r_i$ and $r_j$ being the hard body radii of the objects. By multiplying the collision rate for the time interval between two sampling times, $dt$, the collision probability can be calculated. Thus, within a cube, the collision probability is evaluated using the kinetic theory of gas, meaning that the probability does not depend on the relative distance of the objects while being mainly determined by the cube dimension.

Since Cube was designed to compute the number of collisions between space objects over a period of many years, this formulation of the collision probability is not accurate enough to characterize the risk associated to conjunctions between objects subject to close approaches [47]. Therefore, Cube can be used as a filter for conjunctions, and, in case of close approach, the collision probability can be computed by means of classical covariance-based methods, taking assumptions on the uncertainties into account [46].

However, even when Cube is used only as a filter, the results in terms of number of conjunctions detected is largely affected by the dimension of the cube and the timestep selected for the analysis [47], [48]. In this regard, there can be cases of missed detections when two objects that are very close in terms of position occupy two different cubes by chance. This problem has been faced and solved by the implementation of the Improved Cube (I-Cube) model within SOLEM [45]. Actually, in the I-Cube the concept of the cubes is abandoned, as the authors consider as conjunction each situation in which two objects are at a distance lower than a given threshold (e.g., equal to the diagonal of the original cube). Basically, the algorithm considers a sphere centred in one of the objects with a radius equal to the distance threshold and, when another object enters the sphere, a conjunction is detected. Therefore, in equation (1) the term $dU$ is not the cube volume, but the volume of the sphere with radius equal to $\sqrt{3}h$, where $h$ is the dimension of the cube.

## 2.2 Other tasks

### 2.2.1 Modelling of propagation uncertainties

In general, uncertainties affecting the accuracy of the propagations may depend on many factors. The propagation accuracy can be determined not only by the type and modelling of involved orbital perturbations, as well as by the choice of the error tolerance within the numerical solver, but also by the lack of knowledge in the physical parameters of the space objects, such as the *A/M*. In LEO, the parameters which mainly impact the propagation are the object's ballistic coefficient and the atmospheric density. With regards to the area-to-mass ratio, while it is typically known for active satellites, it can either be time-varying, e.g., for large space debris characterized by a significant tumbling motion, or be known only statistically for space debris produced by fragmentation events (i.e., collisions and explosions) [49]–[51]. This uncertainty in the knowledge of fragments *A/M* distribution is also related to the limits in the minimum size that ground-based sensors can actually detect to improve data fitting.

Concerning the atmospheric density modelling, the space weather (SW) indices, namely the solar Extreme Ultraviolet (EUV, e.g., the F10.7 index of solar radio flux) and the geomagnetic (e.g., Kp and Ap) indices, represent the main model drivers [52]. Indeed, while different models (i.e., Jacchia-Roberts, NRLMSISE-00, Jacchia-Bowmann) agree to some extent when fed by the same SW indices, the output of a model can exhibit significant fluctuations due to variable exposure to Sun and/or solar activity. In general, the uncertainty associated to density forecast represents the main contributor to drag uncertainty in most of the cases. In fact, errors in the estimation of the frontal area are equal to or greater than density-related errors in around 10% of the cases, while being much smaller in the 80% of the cases [53], [54]. So, for the vast majority of Earth orbiting objects, assuming a constant mass, the average frontal area shows very small variations with respect to density modeling error and the global uncertainty is dominated by inaccurate predictions of the SW indices.

Therefore, uncertainty evaluation is a complex process, but it can be crucial to improve the orbit prediction estimation. In the last years, several studies dealt with the modelling of the uncertainties, especially those related to atmospheric density, and how they may affect the orbit prediction of the space objects. Emmert et al. [55] demonstrated that EUV 10-day forecast errors approximately follow a Brownian motion process and they presented approximated analytical expressions linking atmospheric density errors to those in mean motion and mean anomaly. Specifically, they proved that the error variance of the latter grows as a fifth-order exponential function of the time for a Brownian motion density error process. Sagnieres and Scharf [56] instead modelled uncertainties related to the intrinsic variability of the density model as a stochastic process known as Ornstein-Uhlenbeck process (OUP), adapted to this specific application. Schiemenz et al. [57], starting from the formulation proposed by Sagnieres and Scharf, demonstrated that the long-term along-track error due to the modified OUP grows as a third-order exponential function of the propagation time.

Other works address the subject from a more operational point of view, referring to the collision avoidance task. For instance, Hilton et al. [58] proposed a mathematical method based on least-square formulation which exploits real-time navigation and tracking information to build an uncertainty volume around a Resident Space Object (RSO), and analyzed the impact that such uncertainties may have on the development of Cognitive human-machine systems required for SSA and Space Traffic Management (STM) operations. Bussy-Virat et al. [59] instead described the approach to derive the probability density functions (PDFs) associated to the collision risk between space objects, starting from the distributions of historical forecast errors in the solar and geomagnetic indices. Such approach may assist the operators in evaluating the true collision risk. A more analytic approach is proposed by Hao et al. [60], which exploited analytical formulations typical of the relative motion to estimate the along-track position error due to uncertainties in the atmospheric density and the *A/M*, considering a 2-day time span, commonly used for collision avoidance analysis.

In sum, many studies in this field focus on short-term application, mainly aimed at assessing the effect of the uncertainties on the PC between space objects [53], [59], [61], [62].

### 2.2.2 Sensor tasking and sensor calibration

As already said, EU SST contributes to ensure the sustainable access to space for all, the primary objective being to provide space-safety services [63], such as assessing the risk of on-orbit collisions, monitoring uncontrolled re-entry of space debris into Earth's atmosphere, and detect and characterize in-orbit fragmentation events. Therefore, optical, radar and laser sensors are among the most critical components of SST infrastructure since they enable the continuous monitoring of man-made objects orbiting the Earth [64]. Indeed, EU SST can rely on a robust ground-based sensors network, as shown in Figure 2, providing measurements for each service [65].

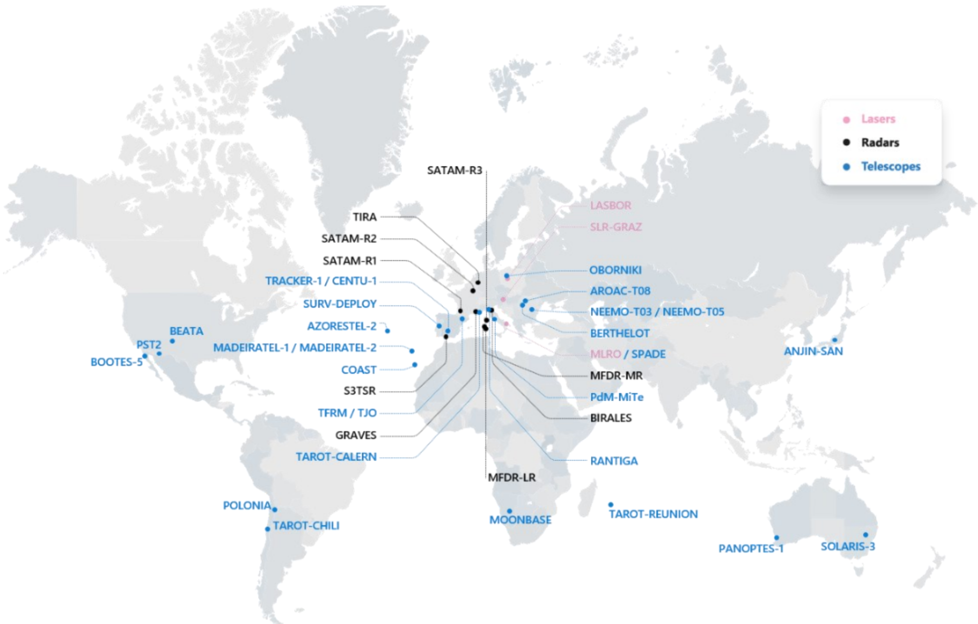


Figure 2 EU SST Sensors Network (as of July 2022)

The proper characterization and calibration of the ground sensors is crucial for the right functioning of the whole SSA system [66]. A prime example of this is the role the sensors play in the orbit determination, when optical and radar measurements at different times are used to reconstruct the orbits of natural objects and satellites [67], [68]. Orbit determination is closely linked with the problem of correlation, which can be a very difficult and computationally heavy task when the number of unknown objects is large [69], [70]. Another useful application is then related to the anomaly and maneuver detection task [70]. Finally, sensors are also required to adequately monitor the uncontrolled re-entry of massive spacecraft and upper stages, as happened for instance with the Italian SST ground sensors network monitoring the re-entry of the first Chinese Space Station, Tiangong-1, in 2018 [71].

Clearly, studying the performance of different sensor configurations is of outmost importance to develop a sensor network providing data for SST services. Therefore, a number of SST sensor network simulation frameworks have been developed in the last years, to better understand actual capacity of the existing sensor networks and to define how to evolve and improve them. Currently, three sensor network simulation tools are available at European level: the BAS3E (Banc d'Analyse et de Simulation d'un Systeme de Surveillance de l'Espace) [72], developed by Centre National d'Etudes Spatiales (CNES), the S3TOC (Spanish Space Surveillance and Tracking Operations Center) [73], and the SENSIT (Space Surveillance Sensor Network Simulation Tool) [74], developed by Politecnico di Milano in collaboration with SpaceDyS company and the Italian Space Agency.

While SENSIT, in its first version, is mainly conceived to perform a statistical analysis of the observational and cataloguing capabilities of sensor networks, thus assessing their performance in terms of catalogue build-up and maintenance, the BAS3E tool implements a sensor scheduling capability, to generate an observation plan for a network of tracking sensor, to meet accuracy requirement for the catalogued objects. In this respect, it is worth recall that observations of a RSO are usually performed using sensors whose field of view (FOV) can be either fixed or steerable. Survey sensors typically have fixed FOV, pointed toward specific sky regions to maximize the number of observations. Tracking sensors, instead, have to observe and follow a specific RSO, thus improving the knowledge of its current and future positions. Therefore, optimization of the tasking strategy is required to define the continuously changing pointing direction of the FOV, in order to maximize the performance of the whole SST system. The BAS3E scheduler solves this tasking problem for a network of tracking sensors, also considering information obtained from survey sensors [72].

The S3TOC tool has the main objective to maintain the quality of the space objects catalogue and to provide collision risk assessment as part of the EU SST consortium, by sending planned observation requests each night to the S3T sensor network, i.e., the Spanish national SST sensors network. Urdampilleta et al. [73] point out that 35% of the 1200 planning requests sent to the nine telescopes of the S3T sensor network between 2018 and 2021 have been identified as unsuccessful tracking requests, meaning that observation is not performed by the telescope or the measurements are not sent back to the operation center. They highlights the need to find an underlying pattern for the failed observations using machine learning (ML) techniques, and to estimate the probability that a tracking request results to be successful, thus improving the observation tasking process and identifying the guidelines for future tasking operations.

Artificial Intelligence (AI) seems to be a promising approach to deal with the sensor tasking problem, as many recent works suggest [75], [76]. For instance, Siew and Linares [75] observed that improved sensor management algorithms are required to allocate the sensing resources efficiently, in particular for long-term sensor tasking problem, whose complexity increases exponentially with the number of targets and observation windows. They proposed an approach based on deep reinforcement learning (DRL) methods to overcome the curse of dimensionality and showed that the four DRL agents, trained within an in-house SSA environment, outperformed myopic policies, achieving higher number of unique RSOs observed over a 90-min observation window. Purpura et al. [76], instead, recently added scheduling capability to the SENSIT tool, by exploiting a genetic algorithm to produce optimal observation schedules.

In the last years, the discussion is shifting towards the idea of Space Domain Awareness (SDA) [77]. Jah [78] individuates the basis of the SDA in the introduction of protocols and procedures to regulate the use of space depending on the availability of quantifiable and timely information regarding the RSOs' behavior. So, the objective of SDA is to surpass the idea of "simple" catalog maintenance, to achieve a comprehensive understanding of the motion of RSOs. To do so, a combination of space surveillance data with other information to help decision-making processes is required, thus increasing the need of data fusion techniques for such application and the need for developing a SDA ontology [79].

### 2.2.3 Recognized Space Picture

The term Recognized Space Picture (RSP) refers to a continuous representative service which provides the presentation of the following [80]:

- Detection, orbital tracking, classification (space surveillance) of artificial space objects
- Identification of space objects of interest (space reconnaissance)
- Ground and space threats assessment on space related activities, services and operations (threats assessment)
- Recognition, display and analysis of environmental phenomena (space weather), supported by a multi-layered multimedia information architecture.

In the space defense context, RSP designs the requirements of Space Forces for a surveillance function needed to carry out space operations, such as defensive/offensive counterspace or missile defense. In a way, RSP is the equivalent for the space domain of the Recognized Air Picture (RAP) commonly used in North Atlantic Treaty Organization (NATO) air control centers [81]. That is why, in this framework, the analysis of both friendly and unfriendly satellites' coverage over particular AOI is of outmost importance to identify the time intervals in which it is advisable to perform particular military operations.

# 3. Orbit propagation

## 3.1 Literature review

As is well known, orbit propagation is a fundamental aspect of almost all SSA and SST applications, representing one of the main “problem” to deal with. To be rigorous, orbit propagation can be defined as the determination of position and velocity of a space object at future time instants, starting from its initial condition at a given instant. Indeed, the capability to accurately propagate the orbit of the objects, being confident enough in the prediction of their state vectors, is crucial, especially to allow the forecast of possible collisions between them. Clearly, to perform early detection of such events, also the computational speed has become an important need, thus pushing the scientific community to look for improvements in the orbit propagation methods, both in terms of accuracy and efficiency.

When considering perturbations, the two-body equation is not accurate enough to describe the orbit. To remove the error of the Keplerian solution, a perturbing acceleration is added to the equation and the problem can be written as

$$\begin{cases} \ddot{\boldsymbol{r}} = -\dfrac{\mu}{r^3}\boldsymbol{r} + \boldsymbol{a}_{\boldsymbol{Perturbed}} \\ \boldsymbol{r}(t_0) = \boldsymbol{r_0} \\ \dot{\boldsymbol{r}}(t_0) = \boldsymbol{v_0} \end{cases} \tag{3.1}$$

where $\boldsymbol{r}$ is the position vector of the space object, $r$ its magnitude, $\mu$ is the Earth standard gravitational parameter and $\boldsymbol{a}_{Perturbed}$ is the total acceleration produced by the perturbing forces acting on the space object, while $\dot{\boldsymbol{r}}$ is the velocity vector of the space object, $t_0$ the initial time instant and $\boldsymbol{r_0}$ and $\boldsymbol{v_0}$ the initial position and velocity vector respectively.

Three main approaches have been generally considered to deal with the orbit propagation problem, differing for the perturbation model considered, the formulation of the equations of motion and the method used to solve them, which can be analytical or numerical:

1) general perturbation techniques, which use analytical methods to solve the problem;
2) special perturbation techniques, which numerically integrate the equations of motion including all the required perturbing accelerations;
3) semi-analytical techniques, that represent a combination of analytical and numerical methods.

General perturbation techniques provide an analytical solution by applying perturbation methods ([82]–[84]). They consist in replacing the original equations of motion with analytical approximation, relying on series expansions of the perturbing accelerations, truncated to simplify the expressions. They produce approximated results, valid for a limited time interval, but the results come as explicit functions of time and other physical constants, thus implying fast evaluations and better understanding of the nature of the orbital motion and the perturbations source. Therefore, these approaches speed up the computation, but decrease the accuracy, the analytical solutions being low-order approximations obtained considering only the most significant forces.

As regards the effect of the perturbations, they can result in secular and periodic variations of the orbital elements (Figure 3). Secular variations vary proportionally to a power of time, and errors in secular terms generate a continuous growth of the propagation error, thus being the main responsible for the degradation of analytical solutions over time. Periodic variations, instead, consist in the repetition of an effect and can be either short-periodic, when the effect repeats on the order of the orbital period, or long-periodic, when the effect repeats on periods one or two order of magnitudes longer than the orbital period. A distinction can be made also between fast and slow variables. Slow variables are those experiencing small changes during an orbital revolution, i.e., semi-major axis, eccentricity, inclination, right ascension of the ascending node and argument of perigee. Fast variables, instead, are those changing a lot during an orbital revolutions, such as the true anomaly, or the cartesian coordinates.

Furthermore, slow variables change only in presence of perturbations, while fast variables obviously change also in their absence.

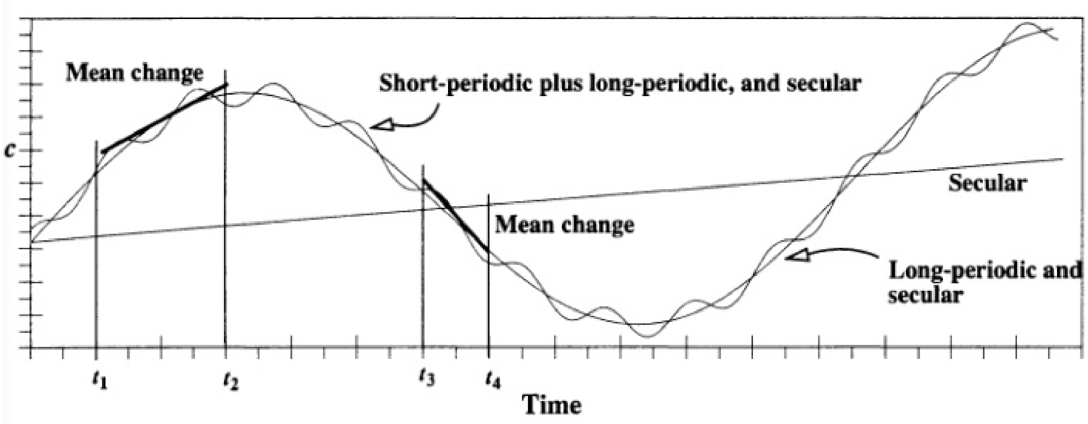


Figure 3 Effect of perturbations on a generic orbital element, *c*. [85]

Most of the existing analytical solutions relies on the variation of parameters (VOP) form of the equations of motion,. This form was first developed by Euler and then improved by Lagrange in 1873, and its basic concept is that, if the constants in the solution can be generalized to be time-changing parameters, the solution for the unperturbed system, i.e., the Keplerian two-body system, can still be used for the perturbed one. So, the VOP equations of motion form a system of first-order differential equations describing the rates of change of the time-varying elements. Two main VOP formulations exist: Lagrangian VOP, which only considers conservative perturbing forces, and Gaussian VOP, which applies to both conservative and nonconservative forces. In 1959, Kozai [86] proposed a method to solve Lagrangian VOP equations using an ad hoc averaging technique, considering only non-sphericity of the Earth (up to J5 only) as perturbation, thus neglecting drag effects. In the same year, Brouwer [82] proposed another approach to solve them, based on the method of canonical transformation and using Delaunay elements, still neglecting drag (drag was then included in successive refinements of the method [87]). For a complete treatment of the VOP formulations and of Kozai's and Brouwer's methods, the reader can also refer to [85] (Chapter 9, pp. 621-637).

However, the most common model in operational applications is the Simplified General Perturbations (SGP4) model. It is a simplified version of the original SGP model [88], whose analytical formulation was based on the works of Brouwer and Kozai, developed in the 1960s. Specifically, it included from Brouwer only the short- and long-period terms in position not containing eccentricity as a factor, and from Kozai the non-Keplerian relation between mean motion and semimajor axis. The main SGP4 simplification with respect to the original model consist in considering only the main terms modelling the secular effect of drag perturbation. Details of the SGP4 derivation were documented in 1979 in Lane and Hoots [89], while source code and algorithmic considerations can be found in the Spacetrack Report #3 by Hoots and Roerich [90] (1980) in its first version, then again in Hoots, Schumacher Jr. and Glover [91] (2004) and in Vallado et al. [92] (2006) in updated versions.

The SGP4 propagator is specially adapted to Two-Line Element (TLE) specifications and represents the standard for dealing with TLE sets. A TLE set contains information about orbital elements of an Earth-orbiting object at a given epoch, in form of mean elements based on the Kozai's theory [83]. TLEs are generated almost continuously by the Joint Space Operations Center (JSPOC) operated by the US Air Force Space Command (AFSPC) and, about every 8 hours, the TLEs catalog of the unclassified objects is shared with SpaceTrack [93] and Celestrak [94] websites for public dissemination. For its ease of accessibility, several SSA applications rely on the TLE catalog, deriving useful information, despite  the accuracy issue of both the SGP4 propagator and the TLEs themselves [95]–[97], which also do not contain covariance information needed in conjunctions operations. A clear and detailed example of a TLE is given in [98] and reported in Figure 4.

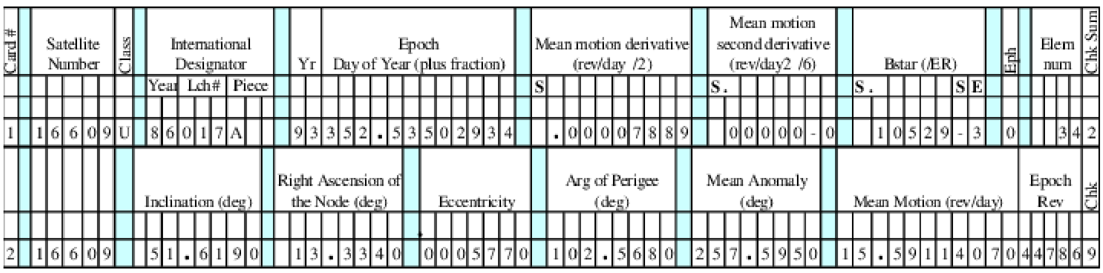


Figure 4 Example of a TLE set, with description and units of each field. [98]

Despite the accuracy issues, analytical theories have represented the standard for orbit propagation for many years, because of their speed and their simplicity. Numerical methods, instead, are characterized by an higher complexity and required computational power, but are the most accurate way to propagate perturbed orbits. Therefore, when modern computers became capable to deal efficiently with numerical integration, special perturbation techniques arose as the most reliable for many applications.

Special perturbation techniques numerically integrate the equations of motion including all necessary perturbing accelerations. Two formulations are mainly used, Encke's and Cowell's formulations. The former, less employed and popular than the other, instead of integrating all the forces acting on the satellite, only integrates the difference between the perturbed and the two-body accelerations, thus dealing with smaller magnitudes. When the difference becomes too large, the orbit is re-initialized at a given point and at a given time. This operation is called "rectification" and proved to be quite advantageous in controlling the errors [99] (Chapter 9, pp. 447-450).

In Cowell's formulation, instead, the single second-order vectorial differential equation of the system of equation (3.1) is written in form of two first-order differential equations, i.e., six scalar equations, thus enabling a wider class of integration methods to solve the problem, i.e., single integration methods.

Indeed, numerical methods can be classified in two groups (see Chapter 8 in [85] and Chapter 4 in [100]):

- single step methods, which start from the single-state value at time $t_0$ and obtain the solution at time $t_0 + \Delta t$, by combining the state at one time with the derivatives computed at several other times. Explicit Runge-Kutta methods are common examples of single-step and they are often used, because they do not need a sequence of back values to start the integration and they meet the propagation needs of most orbital scenarios. However, other single-step methods are known and discussed in the literature, such as collocation integration methods [101] or implicit Runge-Kutta scheme [102], [103], which have been demonstrated to perform better than explicit Runge-Kutta methods, but requiring a higher design complexity.

- multi-step methods, also called predictor-corrector methods, since they perform an initial estimate (prediction) using previous estimates of the states, and then they refine the result using a second series of calculations (correction). These methods can be more accurate, but they are more complex, requiring information of previous conditions. Typical examples of multi-step methods are the Adams-Bashforth-Moulton and the Shampine-Gordon. A detailed discussion about multi-step methods can be found in Berry and Healy [104].

As anticipated before, there is another class of methods to solve the equations of motion, known as the semi-analytical techniques, which represent a combination between the numerical and the analytical methods. The typical approach of these techniques is to separate the short-periodic effects, which are modelled analytically using Fourier series, from the secular and long-periodic contributions, which are numerically integrated with larger step size, since the short-periodic constraints on the step size of the integration is no more present. Then, the contributions are combined at the integration times or using an efficient interpolation [85], [105].

Several semi-analytical methods have been developed. A prominent example is the Draper Semianalytical Satellite Theory (DSST) developed by Cefola and his colleagues in the 1970s. A detailed discussion of the theory behind DSST is reported in Cefola [106] and Danielson et al. [107]. DDST includes an extensive treatment of the perturbations, using Lagrange's VOP equations to model conservative forces and Gauss's VOP equations for non-conservative forces, and shows great flexibility, thus being configurable depending on the different application. Example of its use in SSA/SST applications, especially for orbit determination, are reported in Setty et al. [108] and Cazabonne and Cefola [109].

Other methods exist in the literature. An interesting approach is the one presented by San-Juan et al. [97], which propose an hybrid SGP4 orbit propagator as an improvement to the original TLE-SGP4 system, requiring the modeling of the error associated to the SGP4 propagation during an initial control interval by means of the Holt-Winters algorithm that also provide the error correction.

Other approaches are, instead, based on alternative formulations of the integrals of motion, such as the DROMO propagator conceived by Peláez, Bombardelli and Baù [110]–[112], which implemented a new formulation of the VOP method, or new formulations of the orbital parameters, such as methods based on non-averaged regularized formulations [113] and generalized equinoctial orbital elements [114], [115], that have also been applied in SSA context for collision avoidance [116] and uncertainty propagation [117].

## 3.2 UNINA numerical propagator

A key part of this research activity has been the development and performance assessment of a numerical orbital propagation environment, which represented a useful tool to deal with SST applications in general. In this section, first details about the theory behind and the implementation of the orbit propagator is presented, and then its validation against the propagation environment of the NASA General Mission Analysis Tool (GMAT) is shown. Finally, an accuracy-computational cost trade-off study is carried out and an application to the propagation of fragments coming from a breakup event is reported as an example.

### 3.2.1 Theory and implementation

The developed numerical propagator integrates and solves the equation of motion in Cowell's formulation by using a Runge-Kutta scheme of the $8^{th}$-$9^{th}$ order. As already said, in Cowell's formulation, the perturbing accelerations are added to the two-body equation to obtain the following equation of motion [85],

$$\ddot{\boldsymbol{r}} = -\frac{\mu}{r^3}\boldsymbol{r} + \boldsymbol{a}_{Perturbed} \tag{3.2}$$

The numerical propagator solves the equations of motions and outputs the state vectors in the Earth's Mean Equator and Equinox of epoch J2000 reference frame (EME2000). The propagator takes as inputs the physical characteristics of the object (i.e., *A/M*, drag coefficient, $C_D$, and reflectivity coefficient, $C_R$), the initial conditions (in form of TLE, Keplerian orbital elements or Cartesian vectors of position and velocity), the perturbations' settings and the propagation parameters (i.e., duration and desired time step of the propagation). It outputs the position and velocity vectors of the object at each time step and the corresponding osculating orbital elements. The propagation environment, coded in MATLAB, is easy to integrate with other algorithms. Indeed, the main propagation *function* can be called taking as input a series of MATLAB *structure arrays* containing the input information required.

It is worth noting that also the backward propagation of the orbits has been implemented within the propagation environment, with the same performance of forward propagation. This feature can be very useful in many SST applications, in particular those involving propagation of fragments coming from break-up events.

## Orbital perturbations

The main orbital perturbations are included in the propagation environment, i.e., perturbations due to non-sphericity of the Earth, atmospheric drag, solar radiation pressure and luni-solar third-body gravitational attraction. All the information regarding the perturbations are stored in a *struct* variable taken as input by the propagation function, in which a series of on/off flags must be set by the user, defining the perturbations to be included. The orbital perturbations available and their implementations are discussed in the following.

### Earth gravitational attraction and non-sphericity perturbation

The perturbation due to the gravity field of the Earth is implemented following the procedure described by Vallado [85] (Chapter 8, pp. 538-550), based on Legendre polynomials. The main equations are recalled here.

The components of the acceleration in the Earth-Centered Earth-Fixed (ECEF) reference frame are expressed as

$$a_{g_x} = \left(\frac{1}{r}\frac{\partial U}{\partial r} - \frac{r_z}{r^2\sqrt{r_x^2 + r_y^2}}\frac{\partial U}{\partial \phi_{gc_{sat}}}\right) r_x - \left(\frac{1}{\sqrt{r_x^2 + r_y^2}}\frac{\partial U}{\partial \lambda_{sat}}\right) r_y$$

$$a_{g_y} = \left(\frac{1}{r}\frac{\partial U}{\partial r} - \frac{r_z}{r^2\sqrt{r_x^2 + r_y^2}}\frac{\partial U}{\partial \phi_{gc_{sat}}}\right) r_y + \left(\frac{1}{\sqrt{r_x^2 + r_y^2}}\frac{\partial U}{\partial \lambda_{sat}}\right) r_x \tag{3.3}$$

$$a_{g_z} = \frac{1}{r}\frac{\partial U}{\partial r} r_z + \frac{\sqrt{r_x^2 + r_y^2}}{r^2}\frac{\partial U}{\partial \phi_{gc_{sat}}},$$

where $r_x$, $r_y$ and $r_z$ are the components of the position vector in the ECEF reference frame, while $\frac{\partial U}{\partial r}$, $\frac{\partial U}{\partial \phi_{gc_{sat}}}$ and $\frac{\partial U}{\partial \lambda_{sat}}$ are the partial derivatives of the Legendre potential function $U$ with respect to the position vector, the geocentric latitude and the longitude respectively, which are known as the spherical coordinates. The partial derivatives of the potential function $U$ can be written as

$$\frac{\partial U}{\partial r} = -\frac{\mu}{r^2}\sum_{n=0}^{N}\sum_{m=0}^{n}\left(\frac{R_E}{r}\right)^n (n+1) P_{n,m}\left[\sin\phi_{gc_{sat}}\right] \cdot \left\{C_{n,m}\cos(m\lambda_{sat}) + S_{n,m}\sin(m\lambda_{sat})\right\}$$

$$\begin{aligned}\frac{\partial U}{\partial \phi_{gc_{sat}}} = \frac{\mu}{r}\sum_{n=0}^{N}\sum_{m=0}^{n}\left(\frac{R_E}{r}\right)^n &\left\{P_{n,m+1}\left[\sin\phi_{gc_{sat}}\right]\right. \\ &\left. - m\tan\left(\phi_{gc_{sat}}\right) P_{n,m}\left[\sin\phi_{gc_{sat}}\right]\right\} \\ &\cdot \left\{C_{n,m}\cos(m\lambda_{sat}) + S_{n,m}\sin(m\lambda_{sat})\right\}\end{aligned} \tag{3.4}$$

$$\frac{\partial U}{\partial \lambda_{sat}} = \frac{\mu}{r}\sum_{n=0}^{N}\sum_{m=0}^{n}\left(\frac{R_E}{r}\right)^n m P_{n,m}\left[\sin\phi_{gc_{sat}}\right] \cdot \left\{S_{n,m}\cos(m\lambda_{sat}) - C_{n,m}\sin(m\lambda_{sat})\right\},$$

where $R_E$ is the mean equatorial radius of the Earth, $n$ and $m$ are the degree and order of the gravity field harmonics, $P_{n,m}$ is the associated Legendre function, $C_{n,m}$ and $S_{n,m}$

are coefficients representing the mathematical model of Earth's shape using spherical harmonics. The equations are general and allow to compute the accelerations due to Earth gravity field, by including both the central body attraction and the perturbations due to non-sphericity.

The gravity model selected for this numerical propagator is the Earth Gravity Model 2008 (EGM2008) [118], which is one of the most accurate models and is widely used in the literature. The EGM2008 version implemented contains harmonics up to 70 in degree and order, but the number of harmonics to consider for a specific propagation can be set by the user and depends on the accuracy-speed trade off. It is worth noting that a new version of the EGM, i.e., EGM2020, is expected to be released shortly, and the version implemented in the developed environment will be updated.

**Atmospheric drag perturbation**

The equation of the acceleration due to the atmospheric drag perturbation is

$$\boldsymbol{a_D} = -\frac{1}{2}\rho\frac{C_D A_{Drag}}{M} v\boldsymbol{v}, \tag{3.5}$$

where $C_D$ is the drag coefficient, $A_{Drag}$ is the cross-sectional area, i.e., the area exposed to drag and normal to the object's velocity vector, $M$ is the object's mass, $\rho$ the atmospheric density, $\boldsymbol{v}$ the relative velocity vector between the object and the atmosphere and $v$ its magnitude.

The drag coefficient is a dimensionless quantity whose value is usually around 2.2 for Earth orbiting objects. The group $\frac{C_D A_{Drag}}{M}$ is usually called the ballistic coefficient and it describes how much the object is affected by drag forces. In other applications, such as space exploration, the ballistic coefficient is defined as the reciprocal, $\frac{M}{C_D A_{Drag}}$.

The relative velocity vector, $\boldsymbol{v}$, is expressed in the ECEF reference frame. It is worth specifying here that the transformation matrix for positions and velocities between ECI and ECEF reference frames is computed by means of the *sxform*[1] routine of the NASA's SPICE toolkit, whose kernels[2] are constantly updated.

As regards the atmospheric density, $\rho$, it represents the most critical parameter to model. Indeed, atmospheric density changes because of complex interactions between three aspects: the atmosphere's molecular structure, the incident solar flux and the geomagnetic interactions. A brief description of the main issues related to atmospheric density modelling has been reported in Section 2.2.1 and it is out of the scope of this section. However, interested readers can find more comprehensive treatments in Vallado [85] (Chapter 8, pp. 553-574), Vallado and Finkelman [52] and Emmert [119].

For what is of interest here, four different density models have been implemented within this propagation environment:

- The Jacchia-Roberts 1971 model (JR71), conceived by Jacchia in 1970 [120] and then revised and refined by Jacchia and Roberts in 1971 [121], [122]. This model includes analytical expression for exospheric temperature as function of position, epoch and solar and geomagnetic indices. The density is then computed from empirically determined temperature profiles.
- The NRLMSISE-00 model [123], an empirical atmospheric model developed as major update of the MSISE-90 model. This model is very popular for several applications and has shown good results, in particular for re-entry applications. In general, it runs slightly slower than Jacchia models [85].
- The Jacchia-Roberts 1977 model (JR77), which is an updated version of the Jacchia-Roberts proposed by Jacchia in 1977 [124].
- The Jacchia-Bowman 2008 model (JB2008) [125], an empirical atmospheric density model based on Jacchia's diffusion equation, which uses new solar and geomagnetic indices and implements new equations for the exospheric temperature and geomagnetic storms.

---

1 Documentation related to the "sx_form" routine can be found in https://naif.jpl.nasa.gov/pub/naif/toolkit_docs/C/cspice/sxform_c.html. The transformations are performed from "J2000" (ECI) to "ITRF93" (ECEF) reference frames and viceversa.

2 The updated kernels required by the NASA's SPICE toolkit can be found in https://naif.jpl.nasa.gov/pub/naif/generic_kernels/ .

The user can select not only which model to use for the propagation, but also if space weather effects has to be taken into account (except for JB2008, which only runs considering SW indices). Indeed, if SW effects are considered, the propagator takes as input the "*sw19571001*" file containing the solar and geomagnetic indices (e.g., 3-hour Kp and Ap, F10.7 solar flux index) required for Jacchia-Roberts and NRLMSISE00 models, from 1st October 1957, constantly updated and downloadable from Celestrak[3]. If SW effects are not considered, standard default values are assumed for the indices, i.e., Kp = 3, Ap = 15 and F10.7 = 150 Solar Flux Unit (SFU). The JB2008 model, instead, needs two different files ("DTCFILE"[4] and "SOLFSMY"[5]), containing information about solar and geomagnetic storms.

**Solar Radiation Pressure perturbation**

SRP is a non-conservative perturbation whose impact increases as the altitude increases. Differently from atmospheric drag, which acts only in the direction opposite to the along-track direction, the SRP acts in the anti-solar direction, and in general its contribution distributes itself over the three position components and not only along-track. The equation of the acceleration due to SRP perturbation, $\boldsymbol{a_{SRP}}$, can be expressed as [85]:

$$\boldsymbol{a_{SRP}} = -\frac{P_{SRP}\, C_R A_{SRP}}{M} \frac{\boldsymbol{R_{Sat\odot}}}{\left\|\boldsymbol{R_{Sat\odot}}\right\|}, \tag{3.6}$$

where $P_{SRP}$ is the solar pressure per unit area (equal to $4.57 \times 10^{-6}\ \frac{N}{m^2}$), $C_R$ is the reflectivity coefficient, $A_{SRP}$ the area exposed to the Sun and $\boldsymbol{R_{Sat\odot}}$ is the relative position vector from the satellite to the Sun. The cylindrical model for SRP is implemented, in which the expression of the acceleration is pre-multiplied by a factor, which acts as an on/off factor, assuming only two values: 0 if the satellite is in eclipse with respect to the Sun, 1 otherwise.

---

[3] https://celestrak.org/SpaceData/SW-All.txt
[4] https://sol.spacenvironment.net/jb2008/indices/DTCFILE.TXT
[5] https://sol.spacenvironment.net/jb2008/indices/SOLFSMY.TXT

To evaluate if the satellite is in the Sun, the perpendicular distance between the centerline of the Sun and the satellite is computed, as

$$Dist = r_{ECEF} \cos(90° - \zeta), \tag{3.7}$$

where $r_{ECEF}$ is the position vector expressed in the ECEF reference frame and $\zeta$ is the angle between the Sun and the satellite, as defined in [85] (Chapter 5, pp. 281-282 and Chapter 11, pp. 908-913). If $Dist$ is larger than the Earth radius, the satellite is in the Sun.

**Third-body perturbation**

The third-body perturbation consists in the gravitational attraction that bodies other than the central one have on satellites orbiting Earth. The perturbing acceleration due to third-body effects can be written as:

$$\boldsymbol{a_{TB}} = \mu_{TB} \left( \frac{\boldsymbol{R_{TB}} - \boldsymbol{r}}{\|\boldsymbol{R_{TB}} - \boldsymbol{r}\|^3} - \frac{\boldsymbol{R_{TB}}}{\|\boldsymbol{R_{TB}}\|^3} \right). \tag{3.8}$$

where $\mu_{TB}$ is the standard gravitational parameter of the third-body and $\boldsymbol{R_{TB}}$ is the position vector of the third-body in ECI reference frame. It is worth recalling here that $\boldsymbol{r}$ is the position vector of the satellite in the ECI reference frame.

The third-body perturbation has been implemented for both Moon and Sun, which clearly represent the most disturbing third-bodies for Earth orbiting objects.

## <u>Numerical solver</u>

The integrator selected and implemented to solve the Cartesian formulation of the equations of motion is the Runge-Kutta 8(9). It uses a 8$^{th}$ order Runge-Kutta scheme with a 9$^{th}$ order error control to propagate the object's orbit. The integrator proceed through sixteen intermediate stages, accumulating data from each stage and using them to produce a final integration step. The coefficients used in this explicit Runge-Kutta scheme are derived from Verner [126].

The solver implements a variable step-size technique. At each iteration, two different state estimates are performed using both 8th and 9th order formulations and the difference between them is computed. If the difference is over a given threshold, the time step is corrected and the procedure is repeated. If the difference is lower than the threshold, the higher order estimate is accepted as initial condition for the next step.

To sum up, the workflow of the propagation environment is shown in Figure 5.

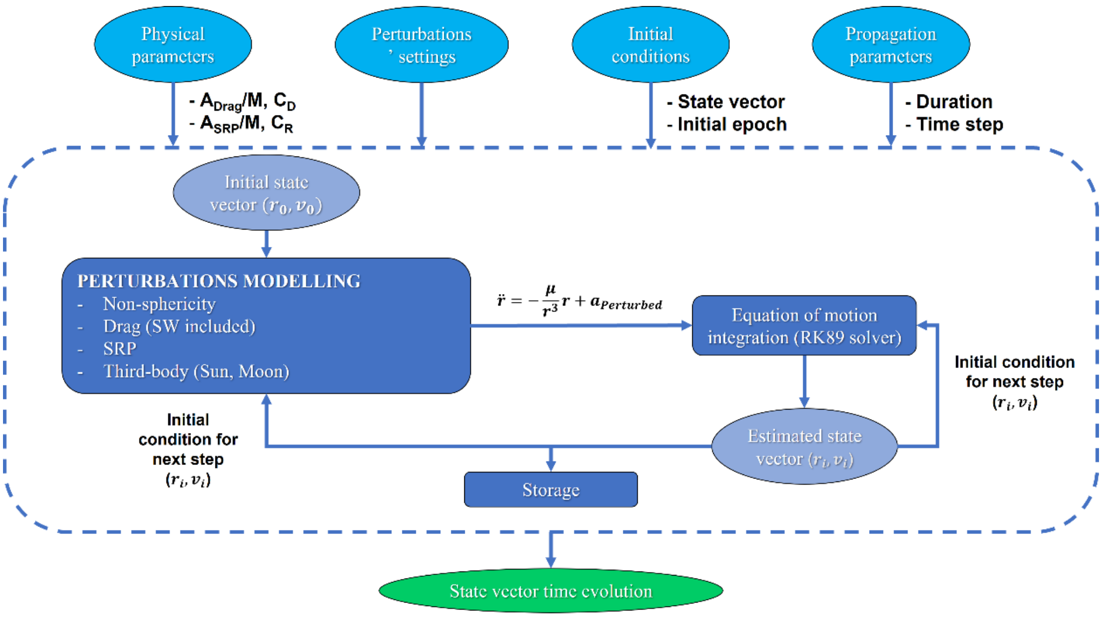


Figure 5 Workflow of the UNINA numerical orbit propagator

### 3.2.2 Validation

The performance of the developed propagator has been tested against GMAT propagator. GMAT is an open source[6] space mission analysis software developed by NASA and private industry. Its first release was in 2007 and the current stable version is the R2020a of July 2020, which is the one adopted to perform the validation. GMAT's numerical propagator allow to define the force model, by selecting which

[6] https://sourceforge.net/projects/gmat/files/GMAT/

perturbations to consider, and the type and settings of the integrator. For more details about GMAT's propagator see the dedicated documentation[7].

Three different real test case scenarios have been considered for the validation, two in LEO, one at lower altitude (International Space Station, NORAD ID: 25544) and the other at higher altitude (Maroc-Tubsat, NORAD ID: 27004), and one in Geostationary Earth Orbit (GEO) (Intelsat-22, NORAD ID: 38098). The orbital characteristics of the three orbits are extracted from TLE data and are shown in Table 1. The performance is evaluated in terms of the position errors evolution during a 30-days propagation, considering both the global error and its components in a classic Radial/Along-track/Cross-track (RSW) reference frame. The position error is computed as the difference between the position vector of the UNINA propagator and the position vector of the GMAT's propagator. For each scenario, the same object's characteristics have been set and they are reported in Table 2.

Table 1 Characteristics of the orbits selected for validation

| | **Low LEO** | **High LEO** | **GEO** |
|---|---|---|---|
| **UTC epoch** | 29/04/2020<br>13:09:32 | 07/06/2020<br>19:50:50 | 03/06/2020<br>11:59:53 |
| **Semi-major axis** | 6803.23 km | 7371.05 km | 42165.6 km |
| **Eccentricity** | 0.0013251 | 0.0029313 | 0.000309 |
| **Inclination** | 51.58° | 99.41° | 0.108° |
| **RAAN** | 228.9° | 293.2° | 86.47° |
| **Argument of perigee** | 136.7° | 37.7° | 13.11° |

[7] https://gmat.sourceforge.net/docs/nightly/html/Propagator.html

Table 2 Characteristics of the space object selected for validation

| **Parameter** | **Value** |
|---|---|
| Mass (kg) | 100 |
| $A_{Drag}$ $(m^2)$ | 1 |
| $C_D$ | 2.2 |
| $A_{SRP}$ $(m^2)$ | 1 |
| $C_R$ | 1 |

It has been possible to select the same perturbation and propagation settings for both the developed numerical propagator and the GMAT's propagator. All the perturbations have been considered, including all the 70 harmonics of the EGM2008, both Moon and Sun as third-bodies, and selecting the JR77 as density model. The "JacchiaRoberts" model has been chosen in GMAT, since it is the most similar to the JR77 implemented in the UNINA propagator, although the implementation is not exactly the same because of discrepancies in some internal time variables computation. Furthermore, the same integrator has been used, thus selecting the Runge-Kutta 8(9) also in GMAT's propagator.

The results for the low LEO scenario are shown in Figure 6 and Figure 7. It is clear that a significant error is accumulated in the along-track direction, because of the slight differences between the atmospheric density models. The impact of the atmospheric density model is even more evident when looking at the position errors of the high LEO scenario, depicted in Figure 8 and Figure 9.

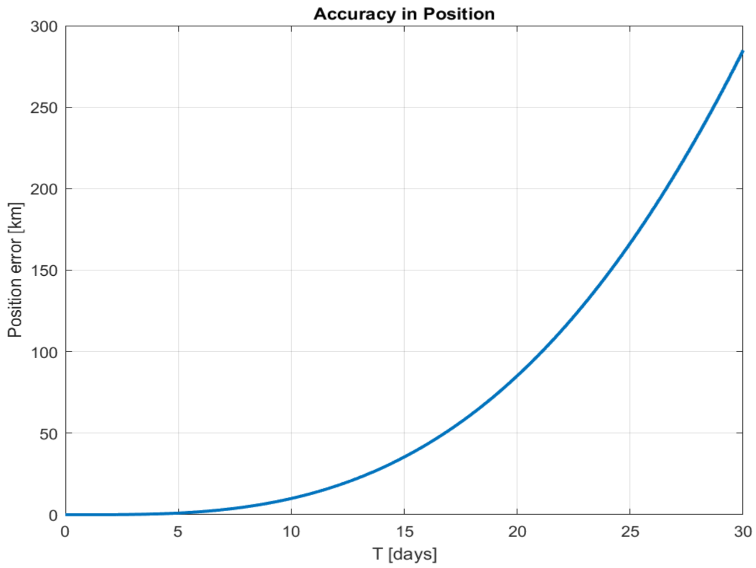


Figure 6 Trend of the position error for a 30 days propagation in the low LEO scenario

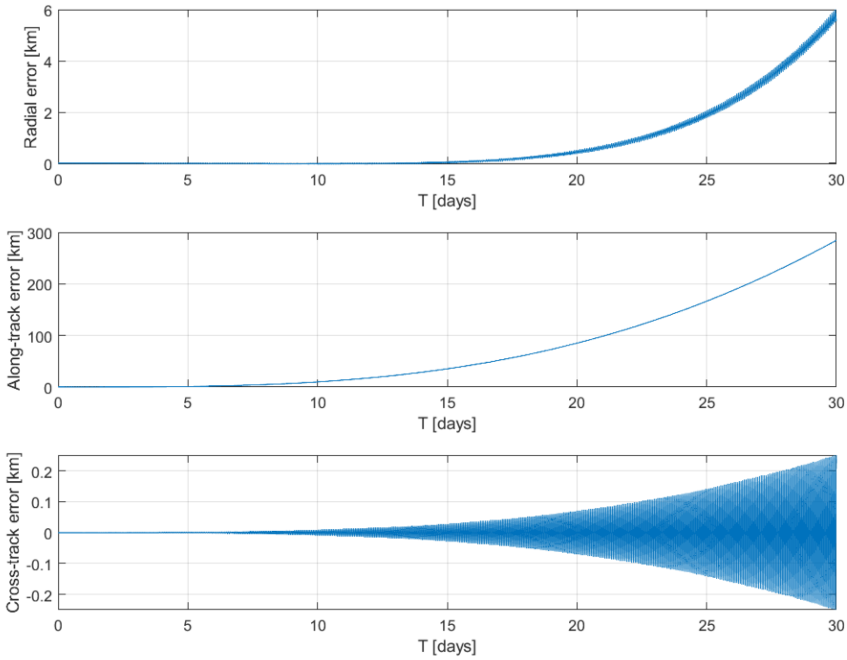


Figure 7 RSW components of the error for a 30 days propagation in the low LEO scenario

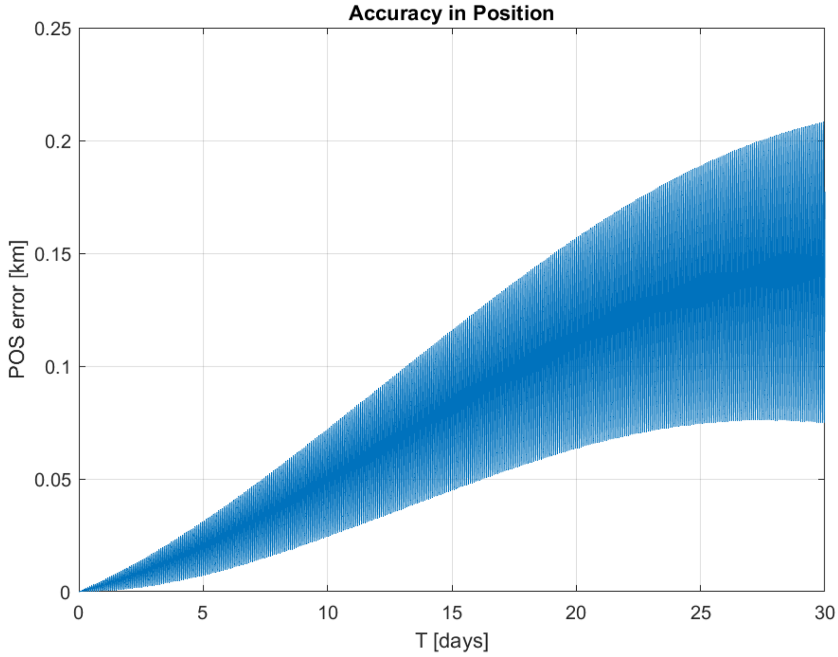


Figure 8 Trend of the position error for a 30 days propagation in the high LEO scenario

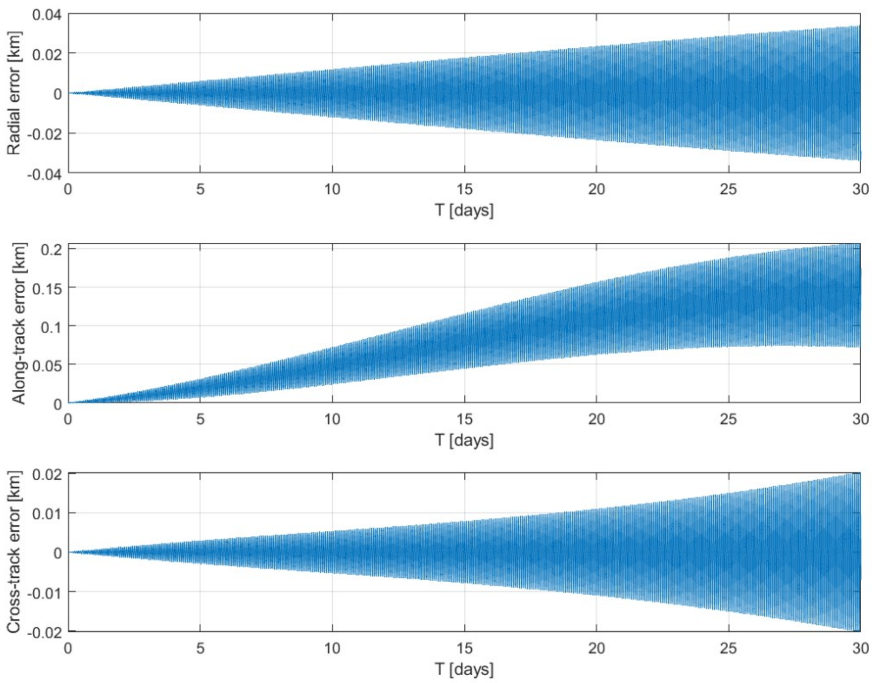


Figure 9 RSW components of the error for a 30 days propagation in the high LEO scenario

Indeed, the error after 30 days drops down from around 280 km in the low LEO scenario to less than 0.2 km in the high LEO scenario, where the atmospheric density is much more rarefied and the atmospheric drag contributes quite little to the perturbing acceleration. Therefore, neglecting the differences related to the atmospheric modelling, the propagator has shown very good performance in terms of accuracy, with errors of few hundreds of meters after 30 days.

Finally, Figure 10 and Figure 11 illustrate the results of the performance assessment for the GEO scenario. Here, the atmospheric drag is negligible and has not been considered for the analysis. Again, the UNINA propagator performed well, with errors of few hundred of meters reached after 30 days. Differently from the previous scenarios, the error is distributed among the three directions, the main perturbation being the solar radiation pressure with acts in anti-solar direction. Indeed, the radial and along-track error components are of the same order of magnitude.

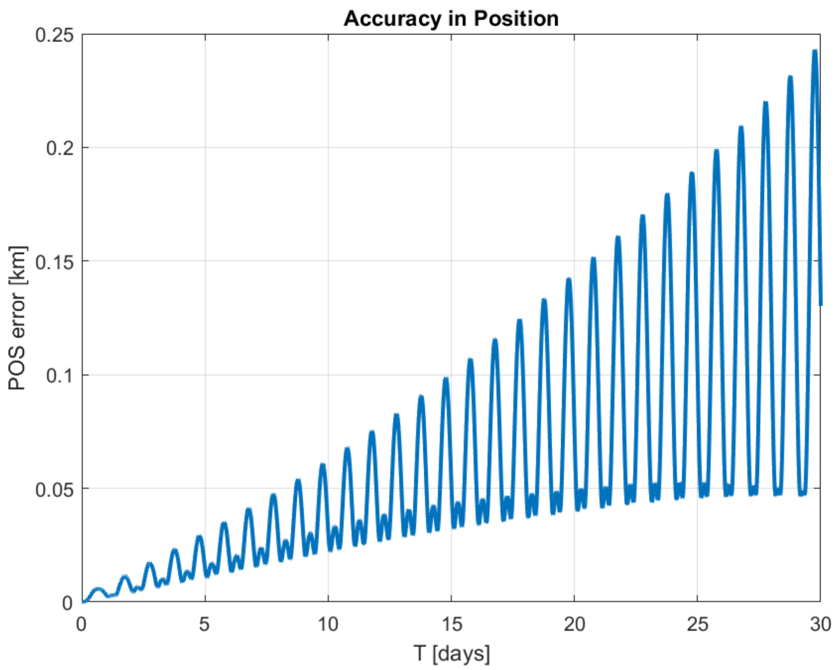


Figure 10 Trend of the position error for a 30 days propagation in the GEO scenario

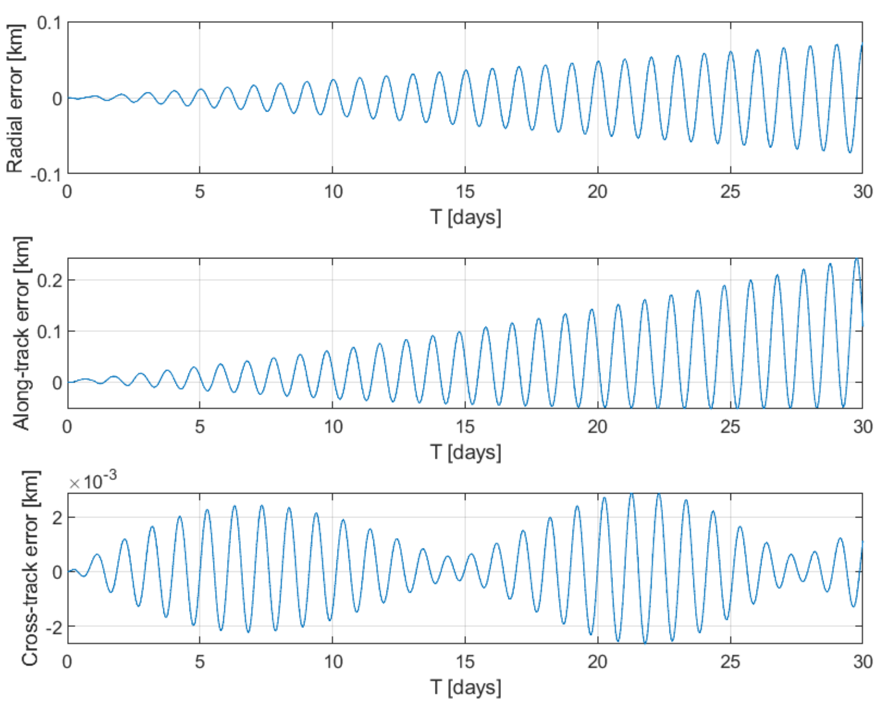


Figure 11 RSW components of the error for a 30 days propagation in GEO scenario

### 3.2.3 Accuracy-computational cost trade-off

The development of an in-house numerical propagation environment allowed to perform some analyses concerning the trade-off between accuracy and computational time. The final goal was to build an adaptive orbital propagation environment integrated in a modular architecture, capable to take both the requirements of the specific SST task and the involved uncertainties into account. To build such a flexible orbital propagator, adaptability criteria need to be identified. To properly select these criteria, it is important to identify task-oriented requirements and to separate the effects of the sources, studying the relative importance of the errors. So, this preliminary part of the work has been faced in the research activity up to now, and, in particular, the impact that area-to-mass (A/M) uncertainty has on the propagation accuracy has been investigated, by comparing errors deriving from such uncertainty with the ones deriving from neglecting some perturbations (i.e., gravitational perturbations due to non-sphericity and third bodies, atmospheric drag and solar radiation pressure).

To this aim, a set of test cases (mainly differing in terms of altitude and inclination) is selected. For each of them, a nominal propagation has been carried out considering all the available perturbations, selecting the Jacchia-Bowman 2008 as density model, as suggested in [52] for LEO propagations, and gravity field harmonics up to 70 in both degree and order, and considering the space object's characteristics reported in Table 3. Both the area-to-mass ratios will be hereinafter referred to as *A/M*, assuming the two values equal for the sake of simplicity. Reference values for *A/M* are taken from literature [127].

Table 3 Nominal physical characteristics of the space object

| **Parameter** | **Value** |
|---|---|
| $A_{Drag}/M\ (m^2/kg)$ | 0.01 |
| $C_D$ | 2.2 |
| $A_{SRP}/M\ (m^2/kg)$ | 0.01 |
| $C_R$ | 1 |

The results of this nominal propagation are then compared with those obtained by

- removing some perturbation terms,
- reducing the gravity field harmonics,
- introducing the *A/M* uncertainty,
- or combining all the above-mentioned actions.

Clearly, the different perturbations' settings to select depend on the specific test case and are mainly influenced by the altitude of the orbit. The *A/M*, instead, has been varied around the nominal value, ranging from a minimum of 0.001 $m^2/kg$ to a maximum of 1 $m^2/kg$, depending again on the test case. For all the propagations, the time span has been set to 7 days, which is a typical time interval of interest for short-term collision risk analysis. The time step was set to 60 seconds for LEO and 1200 seconds for GEO.

The propagation accuracy is evaluated by computing the difference between the position vectors of objects propagated considering all the perturbations (i.e., nominal perturbations' setting) and those obtained when removing perturbations and/or accounting for error in the A/M. Then, to evaluate how the position errors are distributed with respect to the nominal trajectory, the error vectors are rotated from ECI reference frame to RSW reference frame, expressing its components along the radial, along-track and cross-track directions.

In order to identify the adaptability criteria, three different test cases have been analyzed, two in LEO and one in GEO. In all the cases, near-circular orbits have been considered and the initial epochs were in the first days of June 2021. The accuracy and the computational cost of the propagations have been evaluated.

**First test case**

The initial conditions of the first test case are summarized in Table 4. They represent a prograde orbit with an altitude between 477 km and 510 km.

Table 4 Initial conditions of the first test case

| Parameter | Value |
|---|---|
| UTC Epoch | 3 June 2021 11:31:13 |
| Semi-major axis (km) | 6868.5 |
| Eccentricity | 0.00298 |
| Inclination (°) | 86.18 |
| Right ascension of the ascending node (°) | 145.1 |
| Argument of perigee (°) | 91.45 |
| True anomaly (°) | 268.6 |

The orbit is in the thermosphere region of the Earth atmosphere, where the atmospheric density is still significant. Therefore, three different propagation's settings have been selected and tested to evaluate the impact of the perturbations with respect to the nominal case:

- removal of third-body and SRP perturbations (NO TB/SRP)

- reduction of the gravity field harmonics to 20x20 (EGM_20x20)
- both the actions above, resulting in the fastest propagation setting (*FastProp*).

As regards the introduction of the uncertainty in the *A/M* parameter, only two different values have been chosen: twice (i.e., $A/M = 0.02$ m$^2$/kg) and half (i.e., $A/M = 0.005$ m$^2$/kg) the nominal value. For each value of *A/M*, two propagations have been run: the first one considering all the perturbation, as in the nominal scenario, and the second removing third-body and SRP perturbations and reducing the gravity field harmonics to 20x20.

Figure 12 shows the 7-days evolution of the position errors considering the perturbation settings mentioned above. Figure 13, instead, reports the position errors in the along-track direction. The smaller global error characterizing the propagation done reducing the number of harmonics and removing the third-body and SRP perturbations highlighted in Figure 12, can be explained considering that errors related to these two actions are very similar in magnitude, but have opposite signs in the along-track direction as shown by Figure 13. In this case, the errors due to neglecting perturbations are small because the drag perturbation is dominant at this altitude.

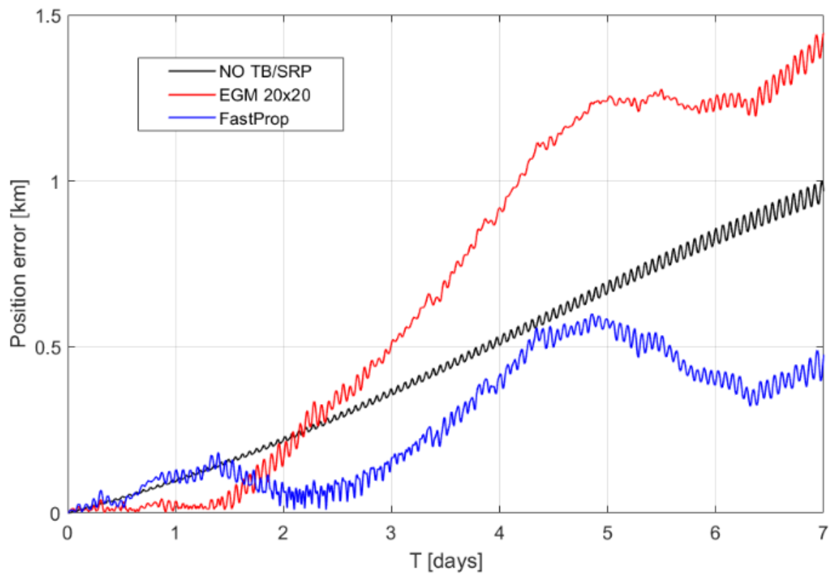


Figure 12 Evolution of the position errors with respect to the nominal propagation's setting when removing Third-Body and SRP perturbation (black line), reducing the gravity field harmonics to 20x20 (red line) and combining both actions (blue line) for the first test case.

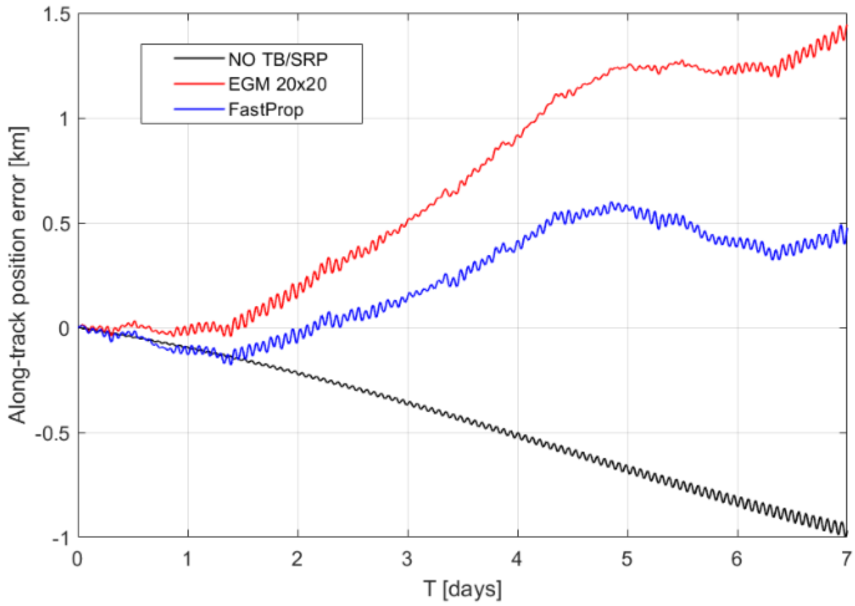


Figure 13 Evolution of the along-track position errors with respect to the nominal propagation's setting when removing Third-Body and SRP perturbation (black line), reducing the gravity field harmonics to 20x20 (red line) and combining both actions (blue line) for the first test case.

Figure 14 presents the evolution of the position errors when introducing the *A/M* uncertainties, also in combination with removals of the perturbations and reduction of the harmonics. The errors due to the uncertainties in the *A/M* are way larger than those obtained when neglecting perturbations. The position errors after 7 days are of about 35 km, when increasing the *A/M* to 0.02 $m^2$/kg, and 17 km, when decreasing the *A/M* to 0.005 $m^2$/kg. Even when considering the *FastProp* setting, the errors remain almost equal, since it introduces an error of 0.5 km only, as shown in Figure 13.

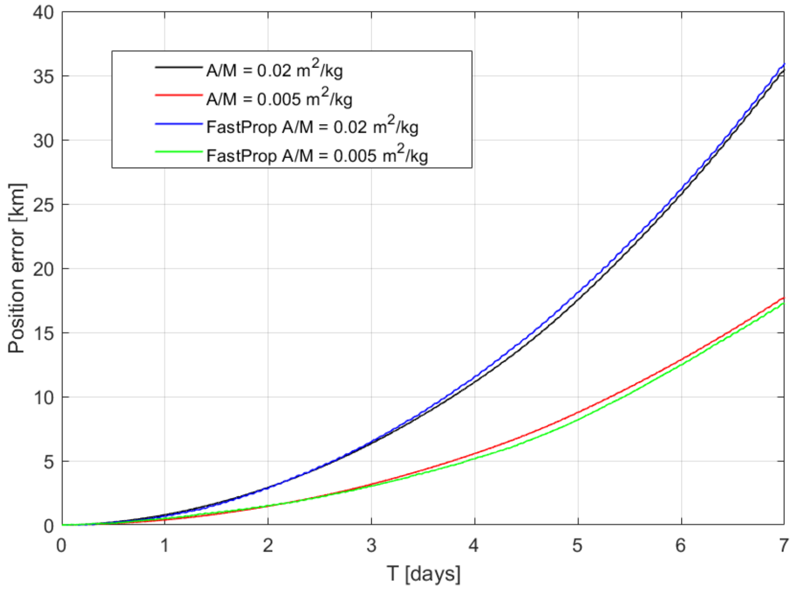


Figure 14 Evolution of the position errors with respect to the nominal propagation's setting when A/M = 0.02 m2/kg, both in nominal (black line) and FastProp (blue line) settings, and A/M = 0.005 m2/kg, both in nominal (red line) and FastProp (green line) settings for the first test case.

The computational times are reported in Table 5. The *FastProp* setting allows to save about 30% of computational time with respect to the propagation with all the perturbations included. Thus, since the related errors are much smaller than those due to the uncertainty in the *A/M*, the *FastProp* setting seems to be a good choice, especially when dealing with a large number of objects (e.g., fragments coming from a real or simulated fragmentation event).

Table 5 Computational times of the first test case propagations

| **Settings** | **Computational times (s)** |
|---|---|
| All perturbations | 248 |
| No TB/SRP | 227 |
| 20x20 harmonics | 176 |
| *FastProp* | 170 |

**Second test case**

The initial conditions of the second test case are reported in Table 6. They represent an 800km-altitude retrograde orbit.

Table 6 Initial conditions of the second test case

| **Parameter** | **Value** |
|---|---|
| UTC Epoch | 4 June 2021 22:05:32 |
| Semi-major axis (km) | 7174.5 |
| Eccentricity | 0.00153 |
| Inclination (°) | 99.41 |
| Right ascension of the ascending node (°) | 141.3 |
| Argument of perigee (°) | 101.3 |
| True anomaly (°) | 287 |

The orbit is just outside of the thermosphere region of the Earth atmosphere. The same analyses as in the first test case have been run, both for the study of the perturbations' impact and the uncertainty effect. Since this orbit is placed at higher altitudes, two additional propagation's settings have been tested: firstly, removing the drag perturbation only and then combining the drag perturbation removal with the other actions.

Figure 15 shows the 7-days evolution of the position errors due to neglecting some perturbations. Figure 16 plots the position errors in the along-track direction. The position errors when varying perturbations' settings are smaller with respect to the first test case, because the reduction of the gravity field harmonics impacts less than before due to the higher altitude. Thus, it is advisable to reduce the number of harmonics for higher altitudes LEO orbits, without removing other perturbations.

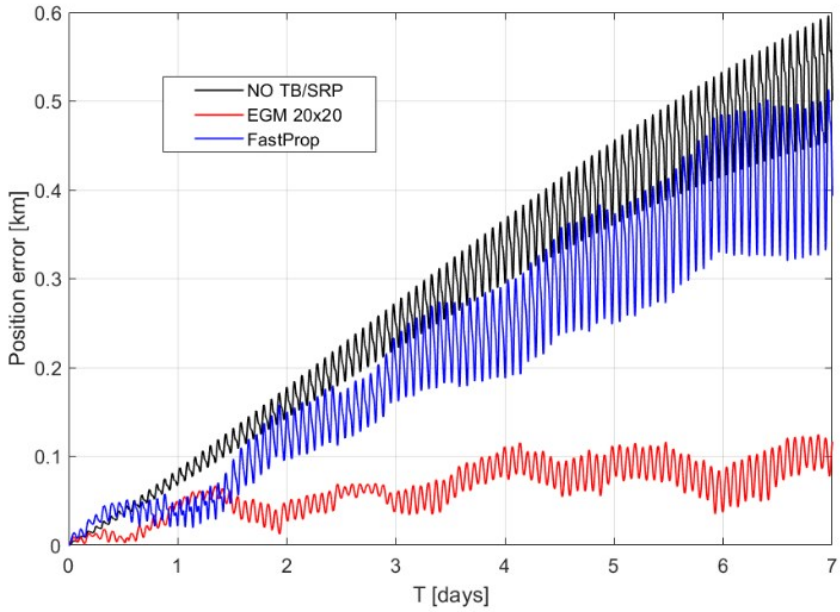


Figure 15 Evolution of the position errors with respect to the nominal propagation's setting when removing Third-Body and SRP perturbation (black line), reducing the gravity field harmonics to 20x20 (red line) and combining both actions (blue line) for the second test case.

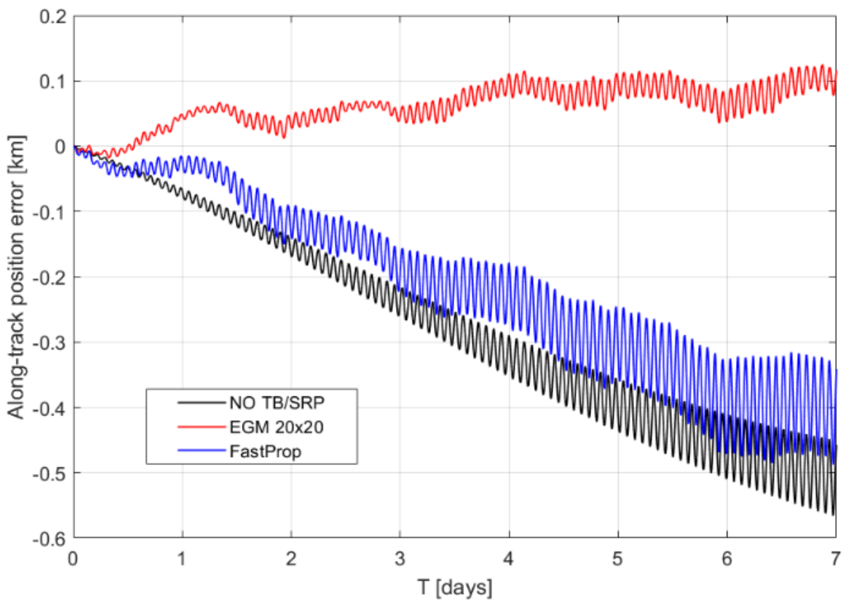


Figure 16 Evolution of the along-track position errors with respect to the nominal propagation's setting when removing Third-Body and SRP perturbation (black line), reducing the gravity field harmonics to 20x20 (red line) and combining both actions (blue line) for the second test case

Figure 17 presents the evolution of the position errors when introducing the *A/M* uncertainties. In this case, the errors coming from the two sources are of the same order of magnitude. It is interesting to note that considering the *FastProp* setting can be convenient also in terms of accuracy when the *A/M* is higher than the nominal value. The reason is that overestimating the A/M has an opposite effect than using the *FastProp* setting in the along-track error (see also Figure 16 and Figure 18).

Figure 19 shows the effects of the drag perturbation removal. Removing the drag perturbation seems to have no critical impact on the accuracy for a 7-days propagation but leads to a great advantage in terms of computational cost (Table 7), in particular when dealing with a large number of objects.

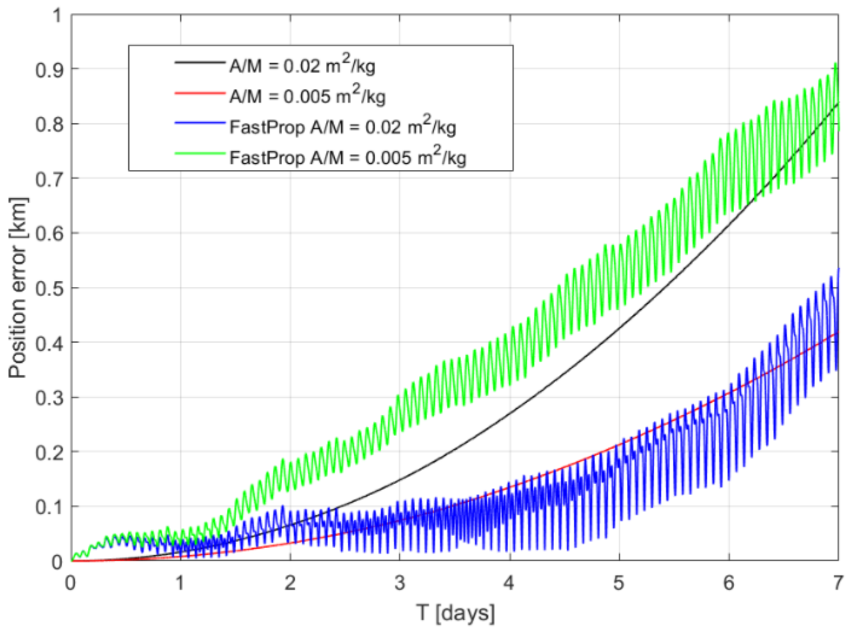


Figure 17 Evolution of the position errors with respect to the nominal propagation's setting when A/M = 0.02 m2/kg, both in nominal (black line) and FastProp (blue line) settings, and A/M = 0.005 m2/kg, both in nominal (red line) and FastProp (green line) settings for the second test case.

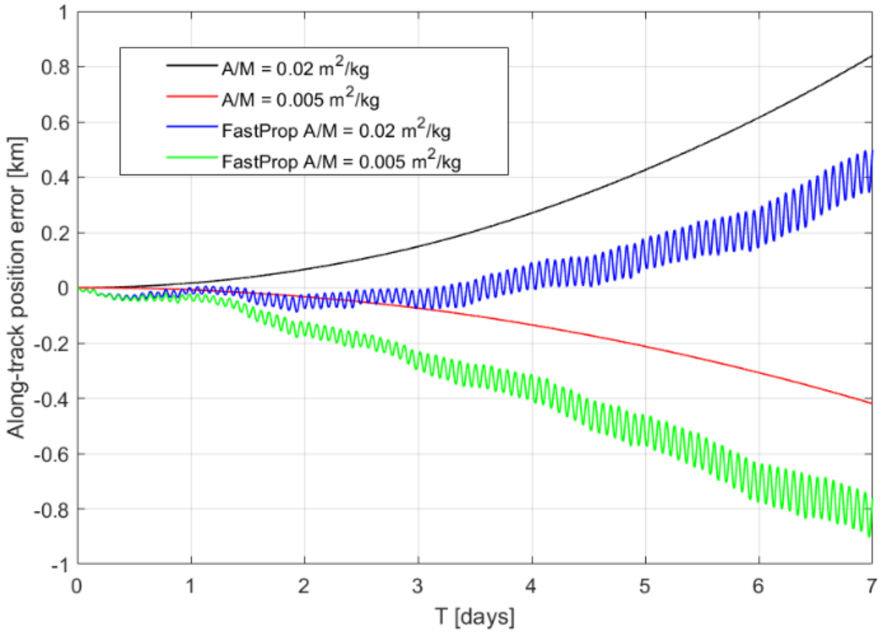


Figure 18 Evolution of the along-track position errors with respect to the nominal propagation's setting when A/M = 0.02 m2/kg, both in nominal (black line) and FastProp (blue line) settings, and A/M = 0.005 m2/kg, both in nominal (red line) and FastProp (green line) settings for the second test case.

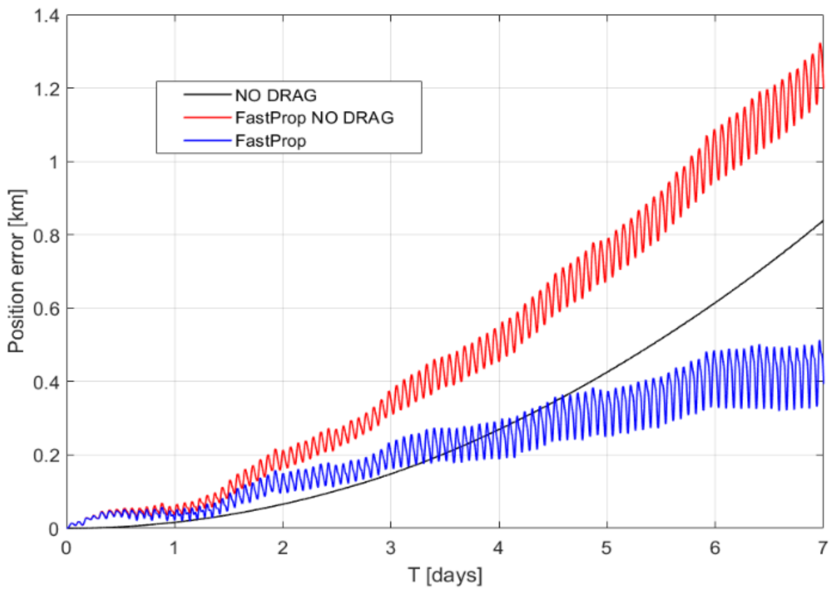


Figure 19 Evolution of the position errors with respect to the nominal propagation's setting when removing drag perturbation (black line), considering FastProp settings (blue line) and combining both actions (red line) for the second test case.

Table 7 Computational times of the second test case propagations

| Settings | Computational times (s) |
|---|---|
| All perturbations | 241 |
| No TB/SRP | 230 |
| 20x20 harmonics | 180 |
| *FastProp* | 171 |
| No Drag | 156 |
| *FastProp* + No Drag | 88 |

**Third test case**

The initial conditions of the third test case are shown in Table 8. They represent a GEO orbit, with inclination close to 0°.

Table 8 Initial conditions of the third test case

| Parameter | Value |
|---|---|
| UTC Epoch | 4 June 2021 22:05:32 |
| Semi-major axis (km) | 7174.5 |
| Eccentricity | 0.00153 |
| Inclination (°) | 99.41 |
| Right ascension of the ascending node (°) | 141.3 |
| Argument of perigee (°) | 101.3 |
| True anomaly (°) | 287 |

In this scenario, analyses different with respect to the previous test cases have been carried out. To investigate the effect of the perturbations, first of all the drag perturbation was removed and the gravity field harmonics were reduced to 20x20. Then, these actions have been combined separately with the removal of the third-body perturbation and the SRP perturbation. The A/M values chosen to simulate the uncertainty in the physical parameter are: 0.001 $m^2/kg$, 0.02 $m^2/kg$, 0.1 $m^2/kg$ and 1 $m^2/kg$.

Figure 20 presents the evolution of the position errors when varying perturbations for the GEO test case. Figure 21 shows the distribution of the position errors in the RSW reference frame. For GEO orbits, the third-body perturbation is dominant, while the errors due to the removal of the drag perturbation and the reduction of the gravity field harmonics are negligible. Therefore, the position error vector has components also along the radial and cross-track direction, differently to the previous test cases.

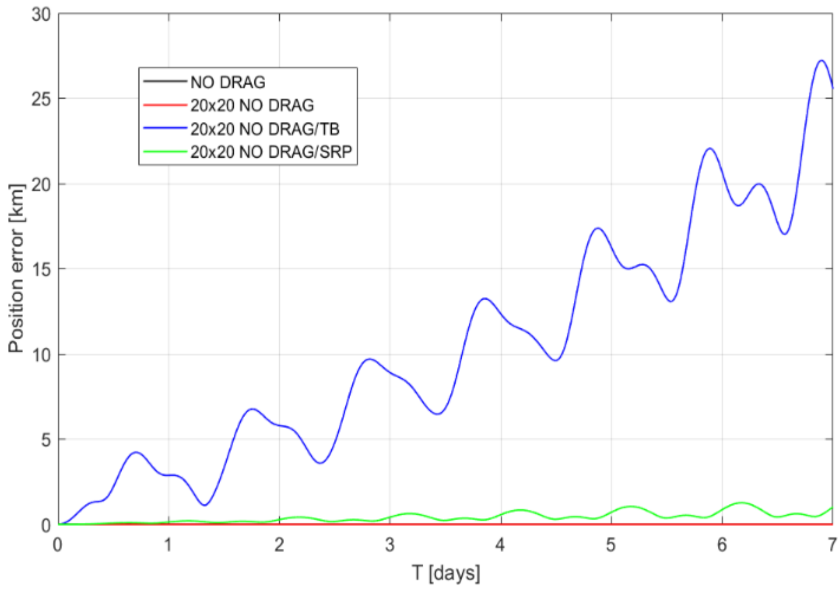


Figure 20 Evolution of the position errors with respect to the nominal propagation's setting when removing the drag perturbation only (black line), removing drag perturbation and reducing the gravity field harmonics to 20x20 (red line), and combining these actions with TB removal (blue line) and SRP removal (green line) for the third test case.

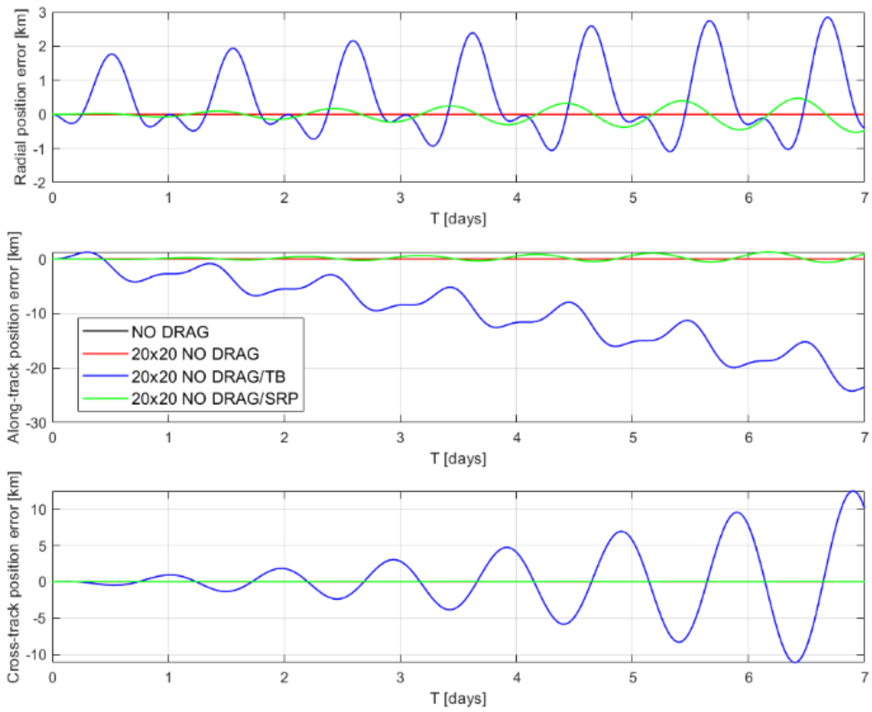


Figure 21 Evolution of the position errors in radial (top), along-track (mid) and cross-track (bottom) directions with respect to the nominal propagation's setting when removing the drag perturbation only (black line), removing drag perturbation and reducing the gravity field harmonics to 20x20 (red line), and combining these actions with TB removal (blue line) and SRP removal (green line) for the third test case.

Figure 22 shows the effects of the *A/M* uncertainties on the propagations. While the *A/M* is small, the Third-body perturbation is much more significant than the others. When increasing the *A/M* of at least one order of magnitude with respect to the nominal value, the effects of the SRP and TB perturbations start to be comparable. The SRP perturbation becomes dominant when the *A/M* is equal to 1 $m^2$/kg.

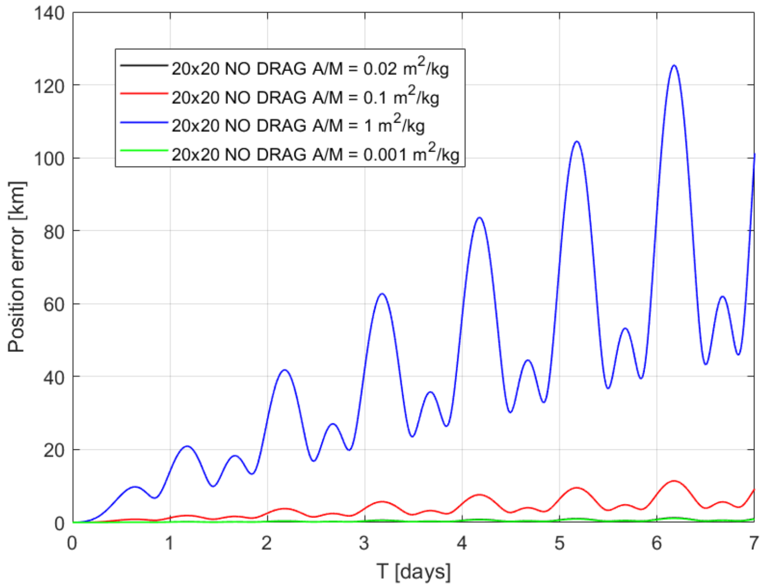


Figure 22 Evolution of the position errors with respect to the nominal propagation's setting when A/M = 0.02 m2/kg (black line), A/M = 0.1 m2/kg (red line), A/M = 1 m2/kg (blue line) and A/M = 0.001 m2/kg (green line) for the third test case.

The computational times of the third test case are presented in Table 9. In general, GEO propagations are much less demanding than LEO propagations in terms of computational cost. However, neglecting some perturbation terms allows to save more than 50% of calculation time with respect to nominal settings.

Table 9 Computational times of the third test case

| **Settings** | **Computational times (s)** |
|---|---|
| All perturbations | 14 |
| No Drag | 8 |
| 20x20 + No Drag | 6 |
| 20x20 + No Drag/TB | 6 |
| 20x20 + No Drag/SRP | 6 |

To conclude this analysis, an application to fragments' propagation is shown in the following. An explosion event has been simulated using NASA EVOLVE 4.0 [51], [128]. The same parameters as the first test case, reported in Table 4, have been assumed as initial conditions of the parent object and epoch of the fragmentation event.

The event generated 216 fragments with a characteristic length over 10 cm, which have been propagated in two different ways: first, considering all the perturbations, and then considering the *FastProp* settings. Figure 23 and Figure 24 show the Gabbard diagram of the generated fragments and the distribution of their A/M respectively.

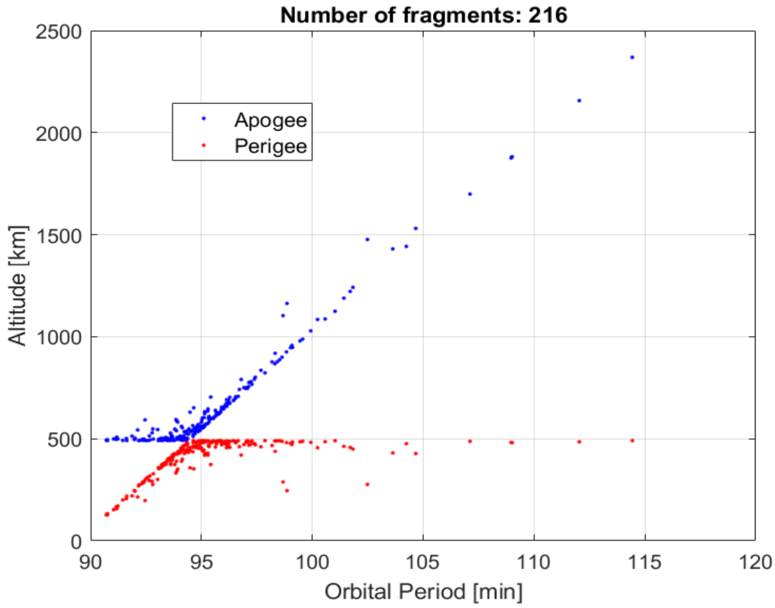


Figure 23 Gabbard diagram of the fragments generated by the simulated explosion event.

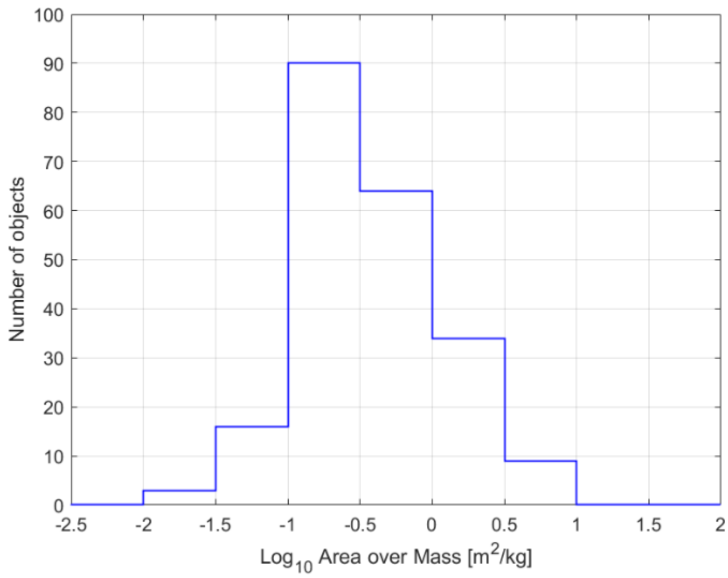


Figure 24 A/M distribution of the fragments generated by the simulated explosion event

Figure 25 shows the boxplots corresponding to the distributions of semi-major axis *a*, eccentricity *e*, inclination, *i,* and right ascension of the ascending node *Ω* of the fragments after the 7-days propagations carried out with the two different perturbation's settings. On each box, the central mark (i.e., the red line) indicates the median of the statistics parameter, the bottom and top edges of the box indicate the 25$^{th}$ and 75$^{th}$ percentiles, respectively. The difference between the 75$^{th}$ and 25$^{th}$ percentiles is called interquartile range (IQR). The whiskers extend to a value equal to 1.5*IQR above the 75$^{th}$ percentile and below the 25$^{th}$ percentile. The values beyond the whiskers are outliers and are plotted using the '+' symbol.

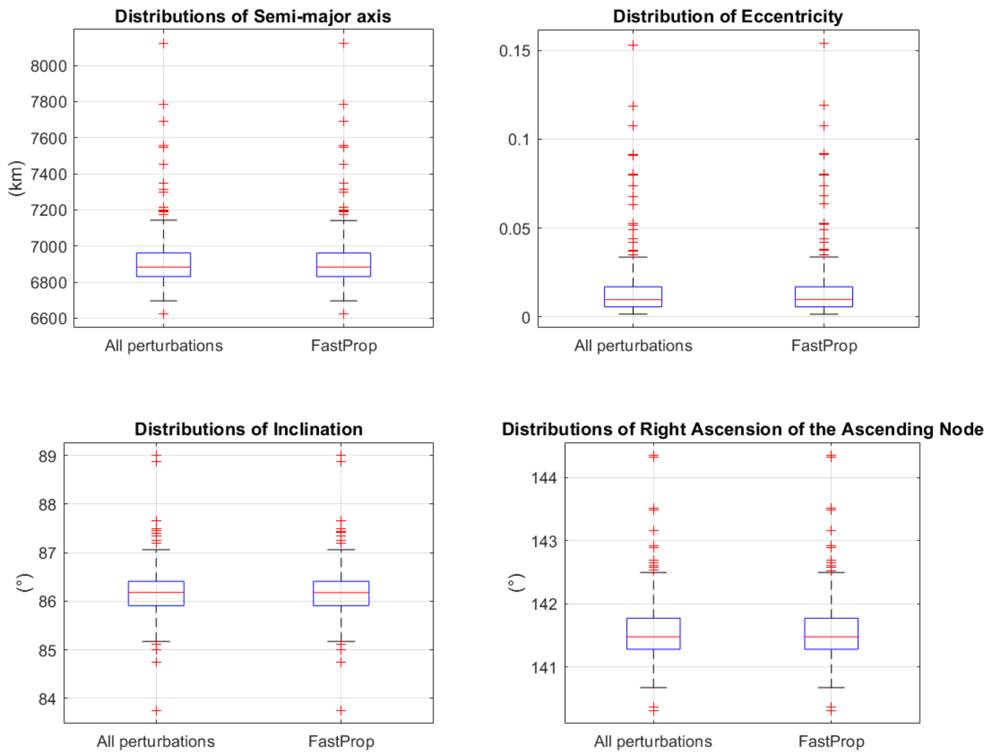


Figure 25 Distributions of semi-major axis (top-left), eccentricity (top-right), inclination (bottom-left) and right ascension of the ascending node (bottom-right) of the fragments after 7 days.

The distributions are evaluated on 189 fragments, since 27 of the 216 initial fragments re-entered during the 7 days and have been removed from the analyses. It can be noted that the two fragments' clouds evolve almost equally for one week, since there is no visible difference in the distributions of the orbital elements. The values of mean, $\mu$, and standard deviation, $\sigma$, of the distributions of the two clouds are presented in Table

10 for the sake of completeness. The results support the theory that neglecting some perturbations (i.e., removing Third-Body and SRP perturbations and reducing the gravity field harmonics to 20x20) does not affect critically the accuracy of a 7-days LEO propagation.

Table 10 Means and standard deviations of the orbital elements' distributions for the two fragments' clouds

| Orbital elements | All perturb. | | FastProp | |
|---|---|---|---|---|
| | $\mu$ | $\sigma$ | $\mu$ | $\sigma$ |
| $a$ (km) | 6928.15 | 183.51 | 6928.21 | 183.38 |
| $e$ | 0.0165 | 0.0215 | 0.0166 | 0.0216 |
| $i$ (°) | 86.1712 | 0.5753 | 86.1709 | 0.5751 |
| $\Omega$ (°) | 141.5889 | 0.5728 | 141.5886 | 0.5725 |

The mean (i.e., per fragment) and total computational times for the two propagations are reported in Table 11. In this example, the *FastProp* settings allow reducing the computational cost of about 35% (i.e., from 7.85 hours to 5.13 hours), resulting in a great advantage when the number of objects to propagate is large. Therefore, in summary, using *FastProp* settings seems to be a viable solution to propagate hundreds of fragments coming from a fragmentation event when interested in short-term collision hazard for threatened assets.

Table 11 Computational times comparison

| Settings | Mean computational time (s) | Total computational time (s) |
|---|---|---|
| All perturbations | 149.5 | 28268 |
| *FastProp* | 97.7 | 18471 |

# 4. Space Surveillance and Tracking applications

In this section, the algorithms developed for SST applications are presented and their performance assessment is discussed. In the first part, the basic idea and the implementation of the Uncertainty-aware Cube method are illustrated and the results of its application in synthetically generated medium-term LEO scenarios are shown. Then, the uncertainty evaluation algorithm, developed to be coupled with the Uncertainty-aware Cube, is presented, also discussing the results of some test cases. Then, the description of the sensor calibration tool is provided, together with examples of sensor calibration for both ground-based radar sensors and telescopes. Finally, in the RSP framework, the Chapter presents the algorithm developed to analyze satellite's overflights over selected AOI, thus showing the results of some examples.

## 4.1 Medium-term collision frequency analysis

One of the critical aspects of the Cube for its use in operative context is that the uncertainties related to the orbit propagation are not considered in the method. It is clear that, when one is interested in the long-term evolution of space debris and the estimation of the number of collisions over time period of many years, considering the uncertainties is not necessary. But for medium-term collision risk analysis, the role of the uncertainties involved in the orbit propagation becomes prominent and cannot be ignored. Since the objects are assumed to be uniformly distributed within a cube, the volume of the cube itself may somehow resemble a positional uncertainty. However, the scale of the accumulated along-track position uncertainty rapidly exceeds the size of the cube, which then is not enough to represent the uncertainties involved. Hence the idea to suggest a modification of the original Cube with the purpose of building an Uncertainty-aware Cube algorithm, able to take the possible error in the space objects' position into account for the detection of the conjunctions.

### 4.1.1 Uncertainty-aware Cube method

Differently from its classic application, the Cube algorithm has been modified to be used for medium-term conjunction analysis in LEO, e.g., considering a time span of 30 days. In this context, the reliability of the Cube method's results can be highly affected by the large uncertainties which characterize the orbit propagation. In LEO, parameters which heavily impact the propagation are the ballistic coefficient of the objects and the atmospheric density model, including the solar activity which contributes to the atmospheric density variation [52]. These parameters enter directly in the computation of the acceleration due to the atmospheric drag, that in turn influences the prediction of the object's position along its own orbit. So, the uncertainty in these parameters results in a lack of knowledge of the true position of the objects, mainly in the along-track direction and, thus, in terms of argument of latitude. It is worth noting that uncertainties in the *A/M* also determine errors in the evaluation of the acceleration due to the SRP perturbation. While the SRP contribution to the position error is not significant for lower LEO orbits, it starts to be comparable to atmospheric drag contribution, or even bigger, for higher LEO orbits, i.e., at altitudes above 700 km. Since SRP acts in the anti-solar direction, in general its contribution distributes itself over the three position components and not only in the along-track direction. Thus, for the applications of this approach to LEO scenarios, the along-track contribution of the SRP error is not significant enough to require explicit modelling. For all these reasons, at this time, the algorithm includes the uncertainties accounting for the along-track position error due to atmospheric drag perturbation only.

The basic idea is that, as the propagation goes ahead, the uncertainties grow more and more, and each object could potentially be in a cube different from the one associated to the position computed by numerical propagation, as if it occupied more than one cube at the same time. The workflow of the algorithm, which is applicable to any set of resident space object of interest, is presented in Figure 26.

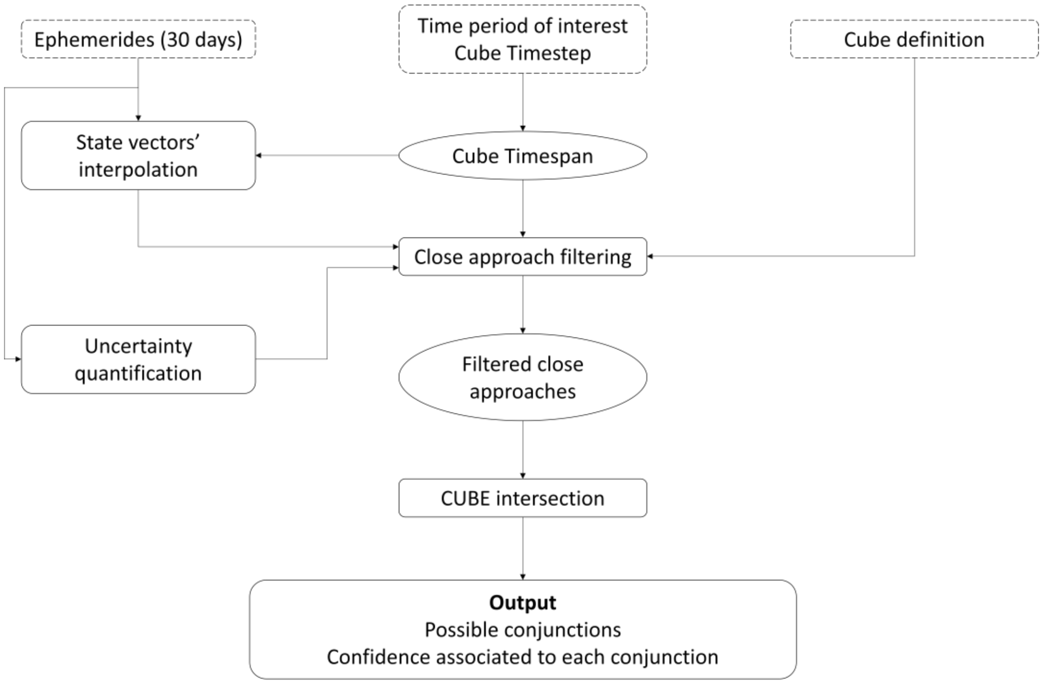


Figure 26 Workflow of the uncertainty-aware Cube algorithm

The reference frame used for all the analyses is the EME2000 reference frame, which is an ECI reference frame. The algorithm takes as input the orbital state of the objects in form of TLE or state vectors, which can be expressed both as Keplerian orbital elements or Cartesian position and velocity vectors. The ephemerides of the objects are then generated by means of numerical propagations, carried out using the developed orbit propagation environment, and interpolated over the timespan of interest for the risk analysis. At this point, a grid is built by dividing the region of space around the Earth in cubes of equal size. The dimension of the cube can be user-defined, or set to a default value of around 1% of the objects' minimum semimajor axis [8], meaning that the cube dimension is slightly bigger than 80 km for LEO scenarios. This value differs from the cube size of 10 km conventionally used in Cube applications, but it is advantageous as it allows reducing the computational time, also considering the significant along-track uncertainty which arise in the considered LEO orbital regimes. Each cube is univocally identified by three coordinates, i.e., ($C_x$, $C_y$, $C_z$) called *cube coordinates* in the following, which represent the cube identification number along each of the ECI direction axes.

A coarse filtering of all the possible close approaches is now carried out. To this aim, at each time instant, the algorithm evaluates the position uncertainty associated to each object as a function of elapsed time and altitude (see Section 4.2 for details about implementation and testing of the uncertainty evaluation algorithm), thus being able to identify the cubes associated to each object. The uncertainty associated to the propagation is modelled as an error on the object's position in the along-track direction. Specifically, it is assumed that the object's true anomaly ($\nu$) can lie in the interval $[\nu - \frac{\Delta\nu}{2}, \nu + \frac{\Delta\nu}{2}]$, where $\Delta\nu$ is computed from the corresponding along-track error ($\Delta R$). Consequently, the object can potentially occupy all the cubes covered by the true anomaly interval. It is worth clarifying that the Cube approach has been implemented here using instantaneous orbital elements, considering its application to time scales relatively short with respect to those considered within long term evolutionary models, in which mean orbital elements are typically used.

Given this information, only the close approaches involving objects separated by a distance below a threshold (defined in terms of number of cubes) along each ECI direction, are filtered through. Specifically, for each couple of objects, e.g., 1 and 2 for clarity, if $\Delta C_{i,1}$ and $\Delta C_{i,2}$ represent the distance potentially covered along direction $i$ by object 1 and 2 respectively due to the propagation uncertainty (and measured as number of cubes), the close approach is selected if the following condition is met

$$\left|C_{i,1} - C_{i,2}\right| \leq \Delta C_{i,1} + \Delta C_{i,2}\ , \forall i = x, y, z \tag{4.1}$$

At this point, every selected close approach is analyzed. Specifically, a conjunction is declared if the two objects have at least one cube in common.

Finally, for each conjunction, an estimation of the degree of confidence in that result is provided. It is assumed that, at each time instant, the true anomaly has a discrete uniform distribution in the previously-defined interval $[\nu - \frac{\Delta\nu}{2},\ \nu + \frac{\Delta\nu}{2}]$, meaning that the object can be found at any position along its orbit in that interval with the same probability. Clearly more positions can lie in the same cube. Therefore, probability that the object is in a particular cube $C$ of coordinates ($C_x$, $C_y$, $C_z$) at a given time instant, i.e., $P_C$, is the ratio between the number of times the cube $C$ is associated to positions in that interval and the total number of positions. Thus, $P_C$ can be expressed as follows:

$$P_C = P_{C_X} \cdot P_{C_Y|C_X} \cdot P_{C_Z|(C_X \cap C_Y)} \tag{4.2}$$

where $P_{C_X}$ is the probability that the object is in a cube with first cube coordinate equal to $C_x$, $P_{C_Y|C_X}$ the conditional probability that the second cube coordinate is equal to $C_y$ given that the first cube coordinate is $C_x$ and $P_{C_Z|(C_X \cap C_Y)}$ the conditional probability that the third cube coordinate is equal to $C_z$ given that the first cube coordinate is $C_x$ and the second is $C_y$. Calculating the probabilities for two objects through Eq. (4.2) and multiplying them, the joint probability is obtained and associated to the possible conjunction. This joint probability measures the confidence with which the objects could share a cube at a given time instant.

### 4.1.2 Application to medium-term propagation scenarios

In this section, a description of the analyses carried out to assess the performance of the Uncertainty-aware Cube method is presented, and the results of the simulations for the different test cases are shown, also compared to those of the Cube method. A test case consists of a synthetically generated conjunction, i.e., two objects in orbit characterized by a miss distance (MD) lower than 2 km. Starting from this conjunction event, the objects' states are backpropagated for many days, i.e., more than 15 days to simulate a medium-term scenario to get the initial condition characterizing the test case. These initial states are then propagated forward for 30 days to obtain the input ephemerides required by the proposed method. The backward and forward propagations are run in nominal conditions, considering $A/M = 0.01$ m$^2$/kg, $C_D = 2.2$, $C_R = 1$ and SISE00 as density model. Then, both the versions of the Cube method have been applied to the nominal scenario, to verify the conjunction detection.

The analyses performed to test the method consisted in evaluating the impact of the A/M uncertainty on their performance. In particular, six levels of percentage variation with respect to the nominal *A/M*, i.e., -90%, -50%, -20%, +20%, +50% e +90%, have been considered. The values of percentage variation are consistent with the results of the analysis on the performance of the uncertainty evaluation tool, shown in Section 4.2.1. New propagations have been run with the altered *A/M* values for both objects. All the possible combinations of the uncertainties, including the cases in which one of the objects has nominal *A/M*, have been tested using both the Cube and Uncertainty-aware Cube methods, with a total number of 48 different combinations. The results are then compared in terms of how many times the methods are still capable to detect the conjunction, i.e., success rate (SR), and in which conditions. The conjunction detected in the nominal case (i.e., both objects having nominal *A/M*) has been excluded from the computation of the SR. A sensitivity analysis has been realized for Test case 1 to assess the impact of the cube dimension on the performance of the method.

**Test case 1**

The first test case is the lowest altitude scenario, i.e., altitude lower than 500 km, where the effect of the atmospheric drag perturbation is more significant. The objects' initial conditions are shown in terms of Keplerian orbital parameters in Table 12, where $v$ is the object's true anomaly. As the minimum semi-major axis of the two objects is equal to 6841 km, the dimension of the cube, i.e., the side length, is 82 km. The initial UTC epoch is on 14$^{th}$ November 2021 at 10:50:50. The synthetic conjunction without any uncertainty is exactly 20 days later, on 4$^{th}$ December 2021 at 10:50:50 UTC, with a MD of 1.43 km and a relative velocity of 10.582 km/s between the two objects.

Table 12 Initial conditions of the objects of Test case 1 in terms of Keplerian orbital parameters

| **Object** | ***a*** | ***e*** | ***i*** | ***Ω*** | ***ω*** | ***v*** |
|---|---|---|---|---|---|---|
| Object 1 | 6855.58 km | 0.000896 | 97.35° | 24.66° | 43.1° | 316.8° |
| Object 2 | 6841.08 km | 0.001828 | 103.13° | 98.76° | 306.2° | 199.8° |

When introducing the *A/M* uncertainties, the results of the two methods are totally different. The Cube method is not capable of detecting the conjunction, regardless of the magnitude of the percentage errors (SR = 0%), as reported in Table 13. The Uncertainty-aware Cube, instead, always finds the conjunction (SR = 100%), thus its results in table form are not shown. However, different combinations of objects' *A/M* percentage errors correspond to different minimum distances and confidence values, as shown in Figure 27-Figure 28. Figure 27 depicts the distances between the two objects when the conjunction is detected as function of the *A/M* uncertainties. The distances grow as the *A/M* values move farther from the nominal value and with respect to each other and they remain quite small when the uncertainties are low or similar (i.e., same amplitude and sign). For the confidence values the opposite is true, as the confidence is higher when the *A/M* uncertainties are low or similar and it reduces if the uncertainties are bigger and of opposite sign (Figure 28).

Table 13 Results of the Cube method when considering the A/M uncertainties for Test case 1

| | | Object 2 | | | | | | |
|---|---|---|---|---|---|---|---|---|
| | *A/M* uncertainty | +90% | +50% | +20% | 0 | -20% | -50% | -90% |
| Object 1 | +90% | X | X | X | X | X | X | X |
| | +50% | X | X | X | X | X | X | X |
| | +20% | X | X | X | X | X | X | X |
| | 0 | X | X | X | ✓ | X | X | X |
| | -20% | X | X | X | X | X | X | X |
| | -50% | X | X | X | X | X | X | X |
| | -90% | X | X | X | X | X | X | X |

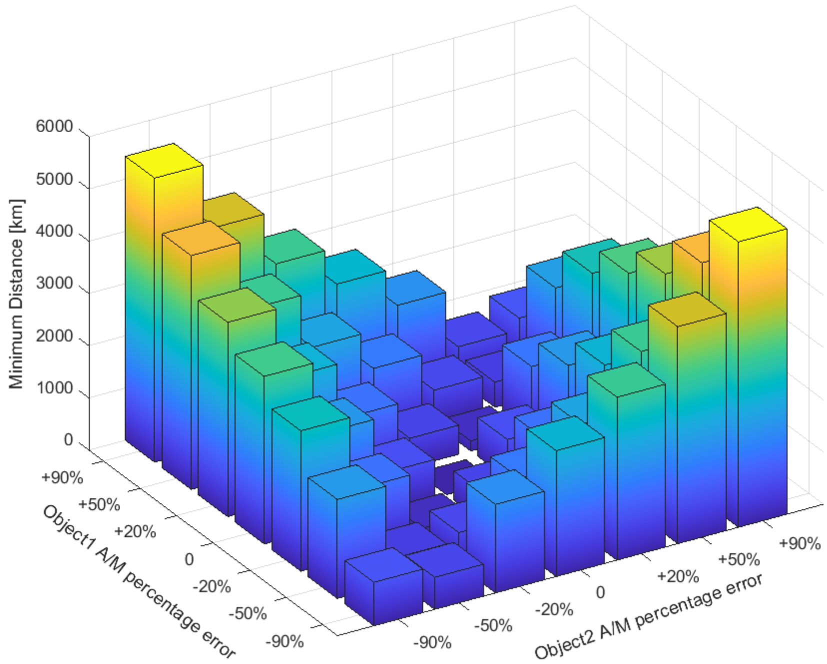


Figure 27 3D histogram of the minimum distance between the two objects as function of the A/M percentage errors for Test case 1

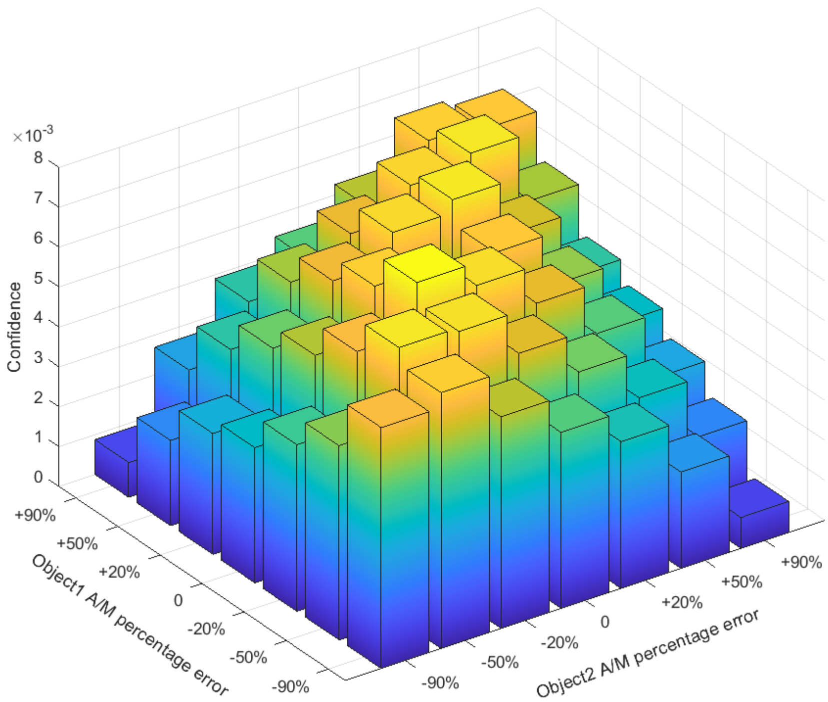


Figure 28 3D histogram of the confidence values associated to the detected conjunctions between the two objects as function of the A/M percentage errors for Test case 1

In Table 14, the characteristics of the conjunctions with maximum and minimum distances are reported, in terms of confidence value, *A/M* uncertainties of the objects and coordinates of the cube occupied by the two objects when the conjunction is detected, as well as cube coordinates of the ideal conjunction. The maximum distance conjunction corresponds to the case with *A/M* uncertainties of -90% for Object 1 and +90% for Object 2, and the cubes occupied by the two objects differ mainly along the y-axis direction. The minimum distance conjunction, instead, occurs when the *A/M* uncertainties are -20% for both the objects, and the cubes occupied are very close to each other and to the cube of the ideal conjunction. The confidence values in the two cases differ of one order of magnitude. This is related to the fact that, at a certain time instant, the objects could share more than one cube, thus more than one possible conjunction is detected by the algorithm and a confidence is computed for each one. In these cases, the algorithm considers a single conjunction with a confidence equal to the sum of all the confidence values associated to the many conjunctions detected at that time instant. Therefore, when the objects are closer, it is more likely that they share several cubes, thus the confidence of the conjunction is higher. The confidence ratio is defined as the ratio between the confidence values of the maximum and minimum distance conjunctions, and it is equal to 0.107 in this case.

Table 14 Characteristics of the maximum and minimum distance conjunctions detected for Test case 1

| | Distance | *A/M* uncertainties | Cube coordinates Object 1 | Cube coordinates Object 2 | Cube coordinates Ideal conjunction | Confidence |
|---|---|---|---|---|---|---|
| Max distance | 5463 km | [-90%,+90%] | [134,122,143] | [134,56,147] | [106,91,166] | 7.73e-4 |
| Min distance | 191 km | [-20%,-20%] | [105,90,166] | [105,92,166] | [106,91,166] | 7.24e-3 |

A sensitivity analysis has been carried out by varying the dimension of the cube, considering 50 km, 100 km and 150 km as side lengths. The results are shown in Figure 29 and Figure 30 for the 50 km case in terms of minimum distances and confidence values respectively, and in Table 15 for all the three cases in terms of characteristics of maximum and minimum distance conjunctions. In this table, the cube coordinates are not reported, because they are different from case to case, as the number of cubes the region of space is divided into is different. While the distances are almost the same, depending only on the objects' propagation, the confidence values change, especially when considering a cube size of 50 km. The reason is that having smaller cubes means that many different cubes are associated to each object, thus strongly reducing the probability associated to them. When considering bigger cubes as well, the confidence values slightly reduce. In this case, although the probabilities associated to each cube are higher, the objects share few cubes, thus the total confidence obtained by summing all the confidence values is lower. However, despite the changes in the absolute values of the confidence, the resulting confidence ratios are very similar, being always around 0.1. This suggests that the confidence values shall not be considered in an absolute sense, but as a reference to measure the relative importance of different conjunctions.

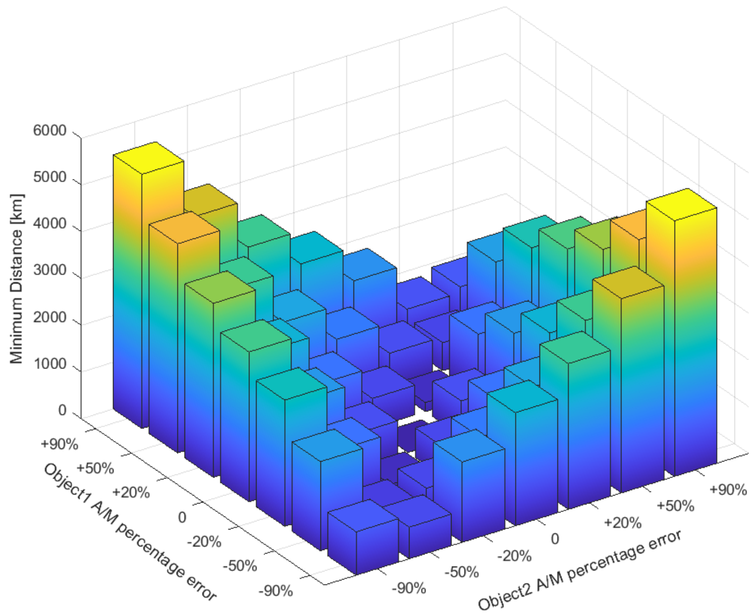


Figure 29 3D histogram of the minimum distances associated to the detected conjunctions between the two objects as function of the A/M percentage errors for Test case 1 with Cube dimension equal to 50 km

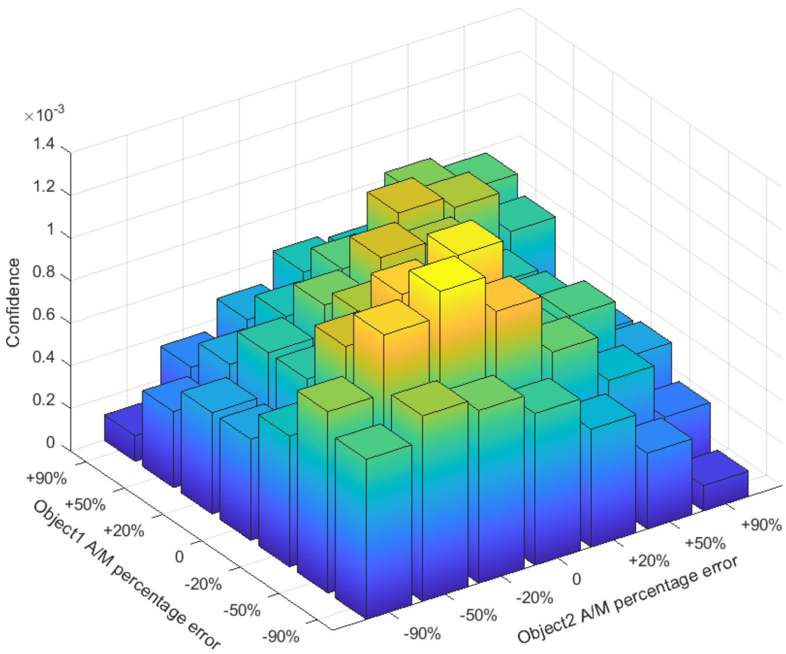


Figure 30 3D histogram of the confidence values associated to the detected conjunctions between the two objects as function of the A/M percentage errors for Test case 1 with Cube dimension equal to 50 km

Table 15 Characteristics of the maximum and minimum distance conjunctions detected for Test case 1 for varying cube size

| | | Distance | *A/M* uncertainties | Confidence | Confidence ratio |
|---|---|---|---|---|---|
| Cube size = 50 km | Max distance | 5465 km | [-90%,+90%] | 1.19e-4 | 0.107 |
| | Min distance | 191 km | [-20%,-20%] | 1.11e-3 | |
| Cube size = 100 km | Max distance | 5463 km | [-90%,+90%] | 6.54e-4 | 0.103 |
| | Min distance | 191 km | [-20%,-20%] | 6.33e-3 | |
| Cube size = 150 km | Max distance | 5463 km | [-90%,+90%] | 6.73e-4 | 0.097 |
| | Min distance | 191 km | [-20%,-20%] | 6.89e-3 | |

**Test case 2**

In the second test case, two objects at altitudes between 500 and 600 km have been considered, the initial conditions being summarized in Table 16. The dimension of the cube is around 83 km, since the minimum semi-major axis is slightly less than 6913 km. The initial epoch is on 14th November 2021 at 14:42:38 UTC and the conjunction in the nominal scenario is exactly 15 days later, on 29th November 2021 at 14:42:38 UTC, with a MD of 0.58 km and a relative velocity of 12.965 km/s between the two objects.

Table 16 Initial conditions of the objects of Test case 2 in terms of orbital parameters

| **Object** | ***a*** | ***e*** | ***i*** | ***Ω*** | ***ω*** | ***v*** |
|---|---|---|---|---|---|---|
| Object 1 | 6931.74 km | 0.00135 | 53.11° | 161.5° | 50.7° | 309.5° |
| Object 2 | 6912.88 km | 0.00183 | 72.46° | 341.2° | 295° | 178.5° |

Again, the Uncertainty-aware Cube is always capable to detect the conjunction (SR = 100%). However, in contrast to Test case 1, Cube detects the conjunction 8 out of 48 times (SR = 17%), when the *A/M* uncertainty is the same for the two objects and two cases in which one of the objects has nominal *A/M* and the other has *A/M* uncertainty of 20% (Table 17). Figure 31-Figure 32 show the minimum distances and confidence values as a function of the *A/M* percentage errors. As the altitude grows, the same *A/M* uncertainties have a less significant effect on the objects' propagation, causing smaller position errors. Therefore, the minimum distances are smaller and the confidence values higher than those of Test case 1. The trends of distances and confidences are the same of Test case 1, with the former growing and the latter reducing when moving away from nominal *A/M* or same *A/M* uncertainty cases.

Table 17 Results of the Cube method when considering the A/M uncertainties for Test case 2

| | | Object 2 | | | | | | |
|---|---|---|---|---|---|---|---|---|
| | *A/M* uncertainty | +90% | +50% | +20% | 0 | -20% | -50% | -90% |
| Object 1 | +90% | ✓ | X | X | X | X | X | X |
| | +50% | X | ✓ | X | X | X | X | X |
| | +20% | X | X | ✓ | X | X | X | X |
| | 0 | X | X | ✓ | ✓ | X | X | X |
| | -20% | X | X | X | ✓ | ✓ | X | X |
| | -50% | X | X | X | X | X | ✓ | X |
| | -90% | X | X | X | X | X | X | ✓ |

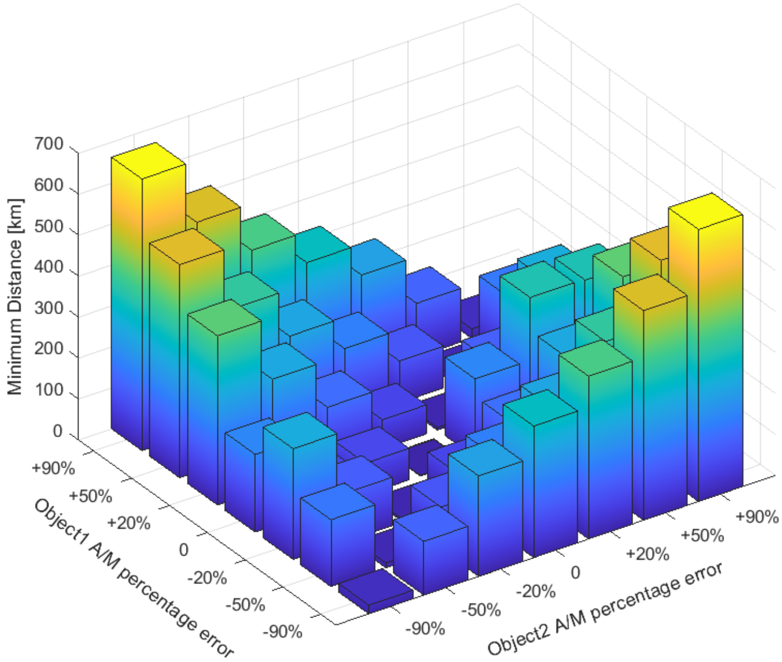


Figure 31 3D histogram of the minimum distances between the two objects as function of the A/M percentage errors for Test case 2

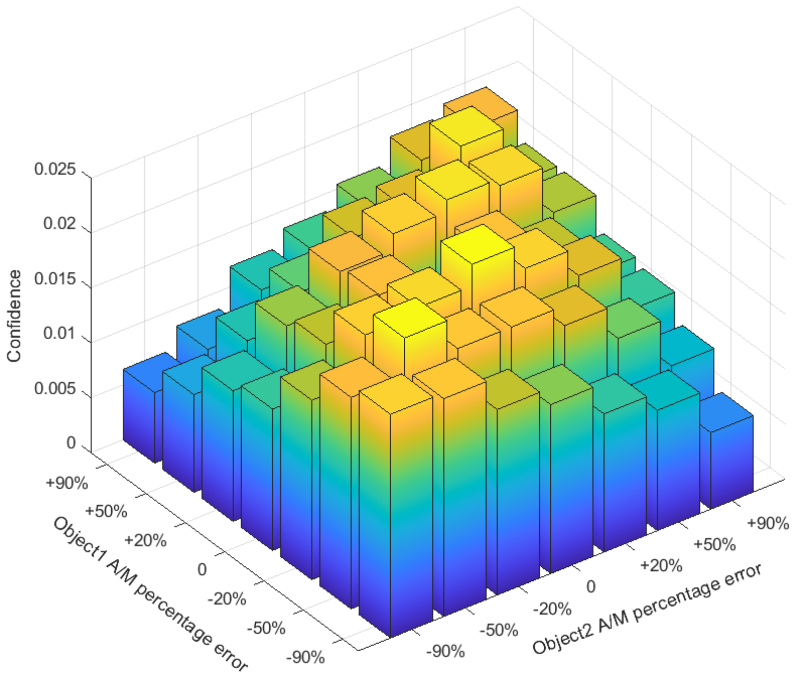


Figure 32 3D histogram of the confidence values associated to the detected conjunctions between the two objects as function of the A/M percentage errors for Test case 2

Table 18 reports the characteristics of the conjunctions with maximum and minimum distances. The maximum distance conjunction corresponds to the case with *A/M* uncertainties of -90% for Object 1 and +90% for Object. The minimum distance conjunction, instead, occurs when the *A/M* uncertainties are -20% for both the objects, which occupy the same cube in this case. The distance values are an order of magnitude smaller than those of Test case 1 (Table 14), while the confidence values are an order of magnitude larger. This is due to the lower number of cubes associated to the objects, thus making higher the probability of each cube.

Table 18 Characteristics of the maximum and minimum distance conjunctions detected for Test case 2

| | Distance | *A/M* uncertainties | Cube coordinates Object 1 | Cube coordinates Object 2 | Cube coordinates Ideal conjunction | Confidence |
|---|---|---|---|---|---|---|
| Max distance | 664 km | [-90%,+90%] | [55,155,120] | [47,152,118] | [51,151,124] | 6.96e-3 |
| Min distance | 6 km | [+20%,+20%] | [51,151,124] | [51,151,124] | [51,151,124] | 2.09e-2 |

**Test case 3**

In the third test case, the altitude range is between 600 and 700 km. The initial orbital parameters of the two objects are shown in Table 19. The minimum semi-major axis is equal to 7015 km and so the dimension of the cube used is 84 km. The initial epoch is on 15$^{th}$ November 2021 at 09:56:44 and the conjunction on 5$^{th}$ December 2021 at 09:56:44, so 20 days later with a MD of 0.67 km. The relative velocity between the objects is 15.059 km/s.

Table 19 Initial conditions of the objects of Test case 3 in terms of Keplerian orbital parameters

| **Object** | ***a*** | ***e*** | ***i*** | ***Ω*** | ***ω*** | ***v*** |
|---|---|---|---|---|---|---|
| Object 1 | 7015.34 km | 0.00129 | 97.86° | 4.82° | 72.6° | 287.3° |
| Object 2 | 7023.27 km | 0.00264 | 81.94° | 225.1° | 38.4° | 6.65° |

In this scenario the objects are at altitudes over 600 km and the position errors due to uncertainties in the physical parameters affecting the atmospheric drag perturbation are much smaller than those in previous test cases. When considering the *A/M* uncertainties, the performance of the two methods starts to be comparable (Table 20), with the Cube being capable to detect the conjunctions 44 out of 48 times (SR = 91.6%), while the SR of Uncertainty-aware Cube is still 100%. To explain this phenomenon, it can be useful to look at Figure 33, which depicts the minimum distances as function of the objects' *A/M* uncertainties. It is clear that there is no more the trend observed at lower altitudes. In particular, the minimum distances are always smaller than 10 km, meaning that the objects are quite close even in the cases in which the Cube is not able to detect the conjunctions. This happens because of one of the limitations of the Cube method: although the objects are close in terms of relative distance, they occupy different cubes by chance, as shown in Table 21, which reports the characteristics of the four conjunctions detected only by the Uncertainty-aware Cube.

Table 20 Results of the Cube method when considering the A/M uncertainties for Test case 3

| | | Object 2 | | | | | | |
|---|---|---|---|---|---|---|---|---|
| | *A/M* uncertainty | +90% | +50% | +20% | 0 | -20% | -50% | -90% |
| Object 1 | +90% | ✓ | ✓ | ✓ | ✓ | ✓ | ✓ | ✓ |
| | +50% | ✓ | ✓ | ✓ | ✓ | ✓ | ✓ | ✓ |
| | +20% | ✓ | ✓ | ✓ | ✓ | X | ✓ | ✓ |
| | 0 | ✓ | ✓ | ✓ | ✓ | ✓ | ✓ | X |
| | -20% | ✓ | ✓ | ✓ | ✓ | ✓ | ✓ | ✓ |
| | -50% | ✓ | ✓ | X | ✓ | X | ✓ | ✓ |
| | -90% | ✓ | ✓ | ✓ | ✓ | ✓ | ✓ | ✓ |

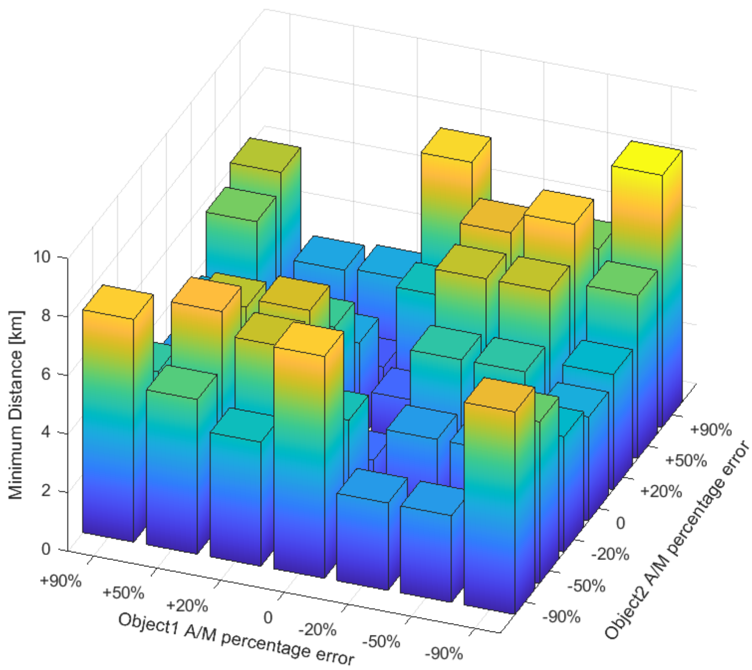


Figure 33 3D histogram of the minimum distances between the two objects as function of the A/M percentage errors for Test case 3

Table 21 Characteristics of the four conjunctions detected only by the Uncertainty-aware Cube for Test case 3

| | Distance | *A/M* uncertainties | Cube coordinates Object 1 | Cube coordinates Object 2 | Cube coordinates Ideal conjunction | Confidence |
|---|---|---|---|---|---|---|
| 1 | 3.02 km | [-50%,-20%] | [72,92,4] | [71,91,4] | [70,91,4] | 7.37e-2 |
| 2 | 6.38 km | [-50%,+20%] | [70,91,4] | [71,91,4] | [70,91,4] | 6.32e-2 |
| 3 | 7.58 km | [0%,-90%] | [73,93,3] | [73,92,3] | [69,90,4] | 2.39e-1 |
| 4 | 6.61 km | [+20%,-20%] | [73,92,3] | [72,92,3] | [71,92,4] | 7.37e-2 |

Finally, the 3D histogram of the confidence values as function of the *A/M* uncertainties is presented in Figure 34. Here, the cases characterized by nominal *A/M* value of one of the objects or same *A/M* uncertainties show very high values of confidence, more than double of the others, since the objects share a lot of cubes in those scenarios. In general, the confidence values are higher than those in previous test cases, because the number of cubes the objects may potentially occupy is reduced, thus increasing the probability assigned to each cube.

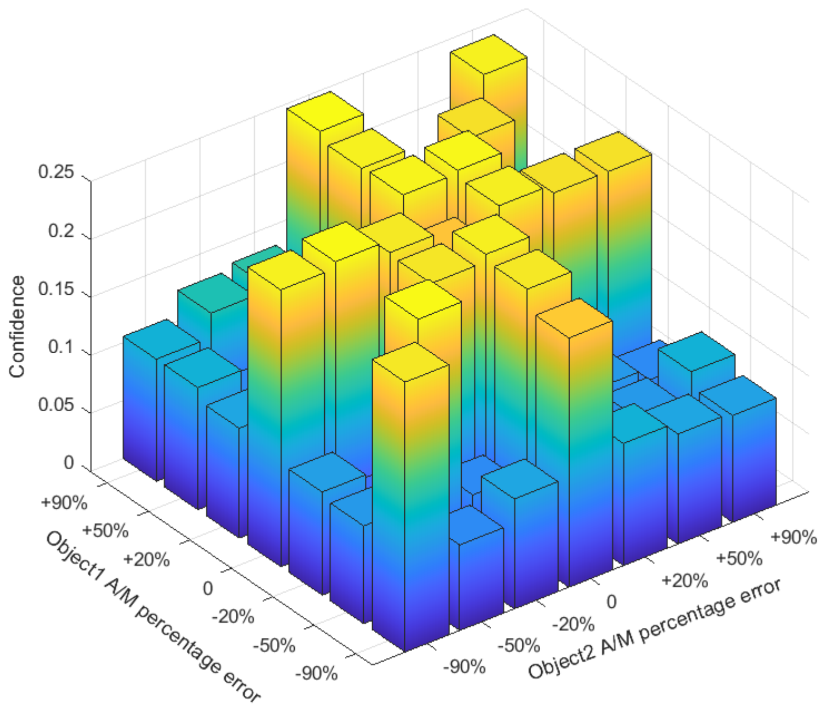


Figure 34 3D histogram of the confidence values associated to the detected conjunctions between the two objects as function of the A/M percentage errors for Test case 3

**Test case 4**

Two objects at altitudes between 700 and 800 km have been chosen for the fourth test case and their initial conditions are reported in Table 22. The cube dimension is around 86 km. The initial epoch is on 14th November 2021 at 14:35:46, while the conjunction event is 25 days later, on 9th December 2021 at 14:35:46 with a MD equal to 0.52 km and a relative velocity of 7.574 km/s.

Table 22 Initial conditions of the objects of Test case 4 in terms of Keplerian orbital parameters

| **Object** | ***a*** | ***e*** | ***i*** | ***Ω*** | ***ω*** | ***v*** |
|---|---|---|---|---|---|---|
| Object 1 | 7139.56 km | 0.00128 | 98.59° | 18.05° | 102.5° | 257.4° |
| Object 2 | 7125.21 km | 0.00398 | 154.9° | 281.4° | 6.61° | 23.1° |

When introducing the *A/M* uncertainties, while the Uncertainty-aware Cube continues to perform well in every condition (SR = 100%), the Cube shows a lower success rate (i.e., SR = 42%), as shown in Table 23. This happens despite the higher altitude, thus resulting in a worse performance with respect to Test case 3, which was characterized by altitudes around 640 km. The results could seem counterintuitive, but the reason is related to the geometry of the orbits. Indeed, the orbital planes are quite distant in terms of inclination angle. Therefore, when considering an uncertainty in the *A/M* value, which causes the objects to be ahead or behind the nominal intersection point along their own orbits, the objects move away quickly from each other. Figure 35 confirms this phenomenon, showing the minimum distances as function of the *A/M* uncertainties. It can be noted that the minimum distances are much larger than those of Test case 3 (Figure 33) and of the maximum admissible distance to be in the same cube, i.e., cube diagonal, explaining the miss detections of the Cube. The confidences, plotted in Figure 36 as function of the *A/M* uncertainties, show very high values in correspondence of the cases characterized by small minimum distances and very low values as the minimum distance grows.

Table 23 Results of the Cube method when considering the A/M uncertainties for Test case 4

| | | Object 2 | | | | | | |
|---|---|---|---|---|---|---|---|---|
| | *A/M* uncertainty | +90% | +50% | +20% | 0 | -20% | -50% | -90% |
| Object 1 | +90% | ✓ | ✓ | ✓ | X | X | X | X |
| | +50% | X | ✓ | ✓ | ✓ | X | X | X |
| | +20% | X | ✓ | ✓ | ✓ | ✓ | X | X |
| | 0 | X | X | ✓ | ✓ | ✓ | X | X |
| | -20% | X | X | ✓ | ✓ | ✓ | X | X |
| | -50% | X | X | X | ✓ | ✓ | ✓ | X |
| | -90% | X | X | X | X | ✓ | ✓ | X |

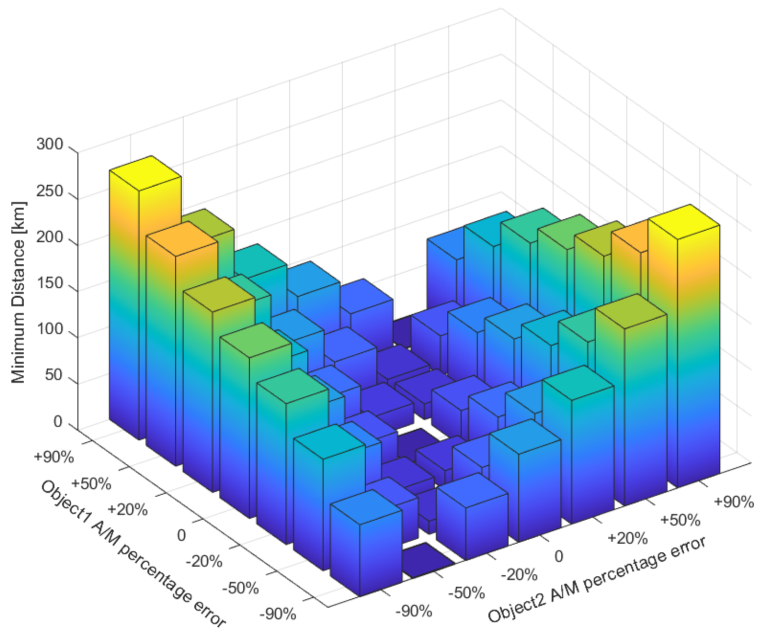


Figure 35 3D histogram of the minimum distances between the two objects as function of the A/M percentage errors for Test case 4

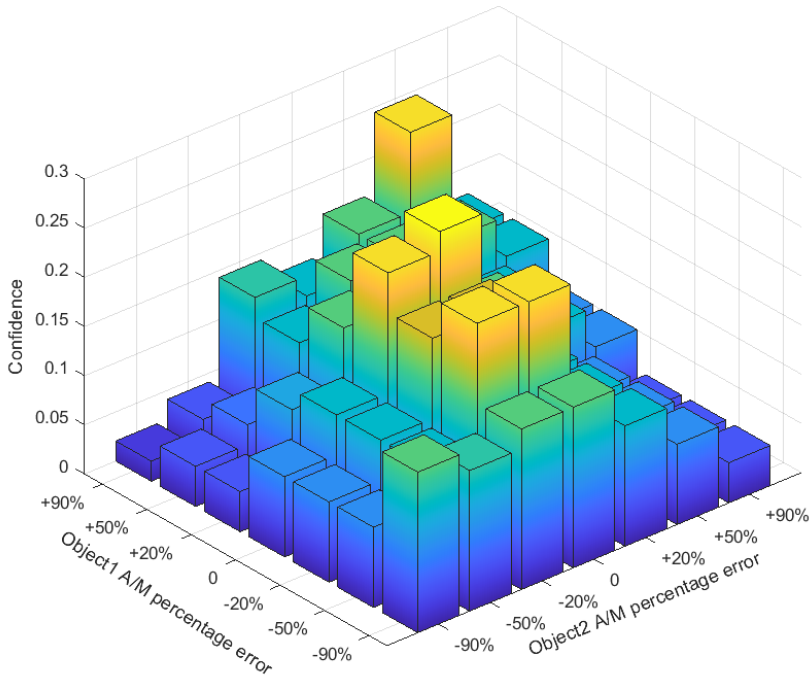


Figure 36 3D histogram of the confidence values associated to the detected conjunctions between the two objects as function of the A/M percentage errors for Test case 4

To further investigate the role of the inclination in the performance of the Cube, another simulation has been run considering a different orbit for Object 2 in the same altitude range, characterized by an inclination angle of 81.4°. In this case the relative velocity between the two objects is 14.955 km/s. The analysis shows that the minimum distances reduce substantially (Figure 37), the Cube being able to detect the conjunction 47 out of 48 times (SR = 98%). This result suggests that the Cube can still be considered suitable to perform medium-term analysis at altitudes higher than 600 km, as long as the orbital planes of the objects are close. When the orbits have very different inclinations, the Cube exhibits a significantly lower success rate. The Uncertainty-aware Cube, instead, is always capable to detect the conjunctions regardless of the uncertainties in the *A/M* value, while these are consistent with the position errors established through the uncertainty evaluation process.

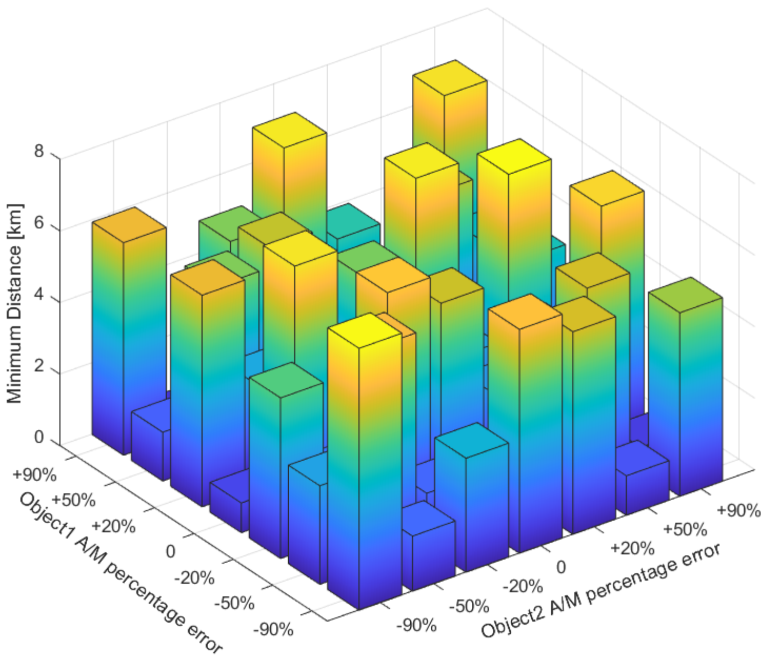


Figure 37 3D histogram of the minimum distances between the two objects as function of the A/M percentage errors for the second version of Test case 4

The results have shown the capability of the proposed method to reduce the missed detection rate by accounting for propagation uncertainties. Clearly, this is achieved at the cost of an increase in the false alarm rate. For the sake of completeness, quantitative information about this issue is provided in the following. In general, the number of potential close approaches detected by the method strongly depends on the orbit altitude, because of the different magnitude of the along-track uncertainties at different altitude ranges. While the method could find hundreds of possible close approaches at low altitudes (i.e., under 600 km), where along-track uncertainties of thousands of kms are accounted for, their number reduces to few instances at higher altitudes. Therefore, the false alarm rate also reduces for increasing orbit altitude, varying from dozens to 2-3 times the false alarm rate of original Cube method. However, it should be said that these false alarms rate are not to be considered as "critical" from an operational point of view, since the Uncertainty-aware method is intended as a medium-term screening and not as a collision avoidance tool. Indeed, with reference to an operative context in which the method could be used to foresee the most endangered assets in the next few weeks and to focus the attention on specific active or debris objects, it is important not to lose information about potential risk, providing early warnings which are consistent with the orbital propagation uncertainty within the considered time horizon. These warnings can then support optimized procedures such as ad hoc sensor tasking to reduce uncertainties.

To summarize the results of the performance assessment, the Uncertainty-aware Cube method resulted to be capable to detect the conjunctions in all the cases and regardless of the *A/M* uncertainties, provided that these are consistent with the position errors computed through the uncertainty evaluation tool. Clearly, the original Cube method is not suitable to perform successfully medium-term risk analysis, being not intended for this purpose. In particular, it exhibits low success rate for low-altitude LEO scenarios, i.e., below 600 km, or when the objects' orbits are quite different in terms of inclination angle. Furthermore, it should be noted that, with respect to standard Cube implementation, the Uncertainty-aware approach requires a larger computational effort, which depends on the cube size and the magnitude of the uncertainties involved. Specifically, the computational time increases when reducing the cube size and when considering lower altitudes, as the uncertainty magnitude increases.

## 4.2 Uncertainty evaluation algorithm

Here, an analytical algorithm for the evaluation of the uncertainty in medium-term scenarios is presented, as a tool to be integrated with the Uncertainty-aware Cube discussed above.

The basic concept of the proposed approach is that, given the propagated orbit of a nominal space object, the motion of a "clone" object with modified physical characteristics can be treated as a relative motion problem between a real and a fictitious object. In particular, the approach is based on the idea that the uncertainties in the input parameters on which the atmospheric drag acceleration depends, cause a sort of differential drag between the two objects.

Recalling the drag equation,

$$\boldsymbol{a_D} = -\frac{1}{2}\rho C_D \frac{A}{M} v\boldsymbol{v}, \tag{4.3}$$

it is possible to see how the drag acceleration, $\boldsymbol{a_D}$, is directly related to both the *A/M* and the atmospheric density, $\rho$. Clearly, errors in the estimation of the ballistic coefficient (i.e., $C_D\, A/M$) and atmospheric density have the same importance (i.e., linear dependence) in determining the atmospheric drag acceleration. Consequently, the two different sources of error can be considered together, meaning that their overall contribution can be modelled by considering an error on a single parameter. Denoting $K = \rho C_D\, A/M$, defining the uncertainty as $\Delta K$, and substituting it in Eq. (4.3), the differential drag equation is obtained as

$$\delta\boldsymbol{a_D} = -\frac{1}{2}\Delta K v\boldsymbol{v}, \tag{4.4}$$

which represents the atmospheric drag acceleration error vector at a given time instant due to the uncertainty in the input physical and environmental parameters.

At this point, the accumulated error in semi-major axis, $\Delta a$, and eccentricity, $\Delta e$, at a given time instant T can be computed as

$$\Delta a = \frac{2}{n}\frac{a}{r}\sqrt{1-e^2}\int_0^T \delta a_D dt, \tag{4.5}$$

$$\Delta e = \frac{\sqrt{1-e^2}}{a^2 e\, n}\left(\frac{a^2\sqrt{1-e^2}}{r} - r\right)\int_0^T \delta a_D dt\,, \tag{4.6}$$

where $a, e$ and $n$ are respectively the semi-major axis, the eccentricity and the mean motion of the nominal orbit, $r$ is the norm of the position vector of the object, and $\delta a_D$ is the magnitude of the differential drag acceleration vector.

The semi-major axis error can be integrated itself to obtain the accumulated error in argument of latitude, $\Delta u$, as

$$\Delta u = -\frac{3}{2}\frac{n}{a}\int_0^T \Delta a\, dt. \tag{4.7}$$

The Hill's equations expressed in terms of DOPs [129], [130] are then used to compute the along-track separation due to the accumulated error in the orbital parameters. Since the method is conceived to be applied to LEO orbits, atmospheric drag is the dominant perturbation. Clearly, it is a planar perturbation, thus causing variations in the semi-major axis, eccentricity and argument of latitude only, as a first approximation. Therefore, in the formulation used for this purpose, only terms depending on variations in these parameters have been considered, while terms depending on inclination or right ascension of the ascending node variations have been neglected. Furthermore, since the real and fictitious objects have the same initial conditions, also terms presenting initial separation errors have been neglected. So, the along-track position error, $\Delta y$, can be expressed as

$$\Delta y = a(\Delta u + 2\Delta e \sin M - \Delta e \Delta u \cos M), \tag{4.8}$$

where $M$ is the mean anomaly of the nominal orbit.

It can be noted that the errors in eccentricity and argument of latitude enter directly in the computation of the along-track separation. The semi-major axis error computed as in Eq. (4.5) can be regarded as a sort of radial error and represents the shrinking of the orbit, which causes the along-track drift, as shown by Eq. (4.7). The proposed approach takes as input only the time evolution of the space object's state vector (in form of ephemerides, orbital parameters or positions and velocities coming from orbital propagation) and a percentage of uncertainty, representing both uncertainties in *A/M* and atmospheric density. The output are the time evolutions of the along-track position error and the semi-major axis error, i.e., radial error, accumulated during the time interval of interest.

### 4.2.1 Uncertainty-evaluation algorithm performance assessment

To assess the performance of the method, the analyses focused on four different test cases in LEO at different altitudes. The initial UTC epochs and the initial Keplerian orbital parameters characterizing the orbits of the four space objects are reported in Table 24 with $i$, $\Omega$, and $\omega$ being respectively the inclination, right ascension of the ascending node and argument of perigee of the orbits. The nominal physical characteristics of the objects for the four test cases are reported in Table 25.

Table 24 Initial UTC epochs and orbital elements of the objects of the four test cases

| **Object** | **UTC epoch** | **$a$ (km)** | **$e$** | **$i$ (°)** | **$\Omega$ (°)** | **$\omega$ (°)** |
|---|---|---|---|---|---|---|
| Object 1 | 14 November 2021 10:50:50 | 6855.58 | 0.000896 | 97.35 | 24.66 | 43.1 |
| Object 2 | 14 November 2021 14:42:38 | 6931.74 | 0.00135 | 53.11 | 161.5 | 50.7 |
| Object 3 | 15 November 2021 09:56:44 | 7015.34 | 0.00129 | 97.86 | 4.82 | 72.6 |
| Object 4 | 14 November 2021 14:35:46 | 7139.56 | 0.00128 | 98.59 | 18.05 | 102.5 |

Table 25 Nominal physical characteristics of the space objects

| **Parameter** | **Value** |
|---|---|
| $A/M\ (m^2/kg)$ | 0.01 |
| $C_D$ | 2.2 |
| $C_R$ | 1 |

For each test case, four different values of *K* uncertainty have been considered, i.e., +20%, +50%, +100% and +200%. The uncertainty is global and takes into account the combination of the two main sources of error, but these levels of uncertainty can be considered representative of specific scenarios that could occur. For instance, uncertainties from 20% to 100% can represent situations in which the objects are characterized by a stable history of the ballistic coefficient, so the uncertainty is only expression of the misprediction of solar and geomagnetic indices which determine the atmospheric density estimation, with a growing degree of error. The 200% uncertainty, instead, can represent a scenario in which, in addition to the atmospheric density prediction uncertainty, there is also a significant *A/M* mismodeling that can be related to estimation error during the orbit determination process.

It should be noted that, as already said, most of the Earth orbiting space objects shows quite stable trends of the ballistic coefficient, with small *A/M* variations, so the first three uncertainty levels could depict the most frequent scenarios. This is true especially for the 100% uncertainty case, that well emulates a typical degree of uncertainty due to EUV indices forecasting error. The 200% uncertainty case, instead, can be regarded as a “worst” case, that may still apply to the reminder of Earth orbiting objects. Sometimes, the uncertainty on density and/or ballistic coefficient can be treated as noise in the numerical propagation, but in this application it is kept constant during the propagation. Such assumption has been made to carry out a worst-case scenario analysis.

The workflow of the analyses carried out is presented in the following and shown in Figure 38. The orbit of the object is propagated for 30 days using the numerical propagator, firstly with the nominal $K$, and then considering the $K$ percentage variation representing the uncertainties involved. In this application, all the available perturbations have been considered, limiting the harmonics of the EGM2008 gravity field to 20 in degree and order and selecting the NRLMSISE00 (SISE00) as density model, with a constant medium solar activity modelled using F10.7 index of 150 Solar Flux Unit (SFU) and an Ap index equal to 15.

The difference between the position vectors of the object propagated in nominal condition and those obtained when accounting for error in $K$ is computed and expressed in a classic RSW reference frame [85] centered in the nominal object, to obtain the along-track component of the position error. The time evolutions of the along-track separation and the semi-major axis error represent the benchmark for the analysis. At this point, the state vectors of the nominal propagation and the percentage value of the uncertainty are given as input to the algorithm. It outputs the 30-day time evolutions of the errors in along-track position and semi-major axis, that are compared to the benchmark.

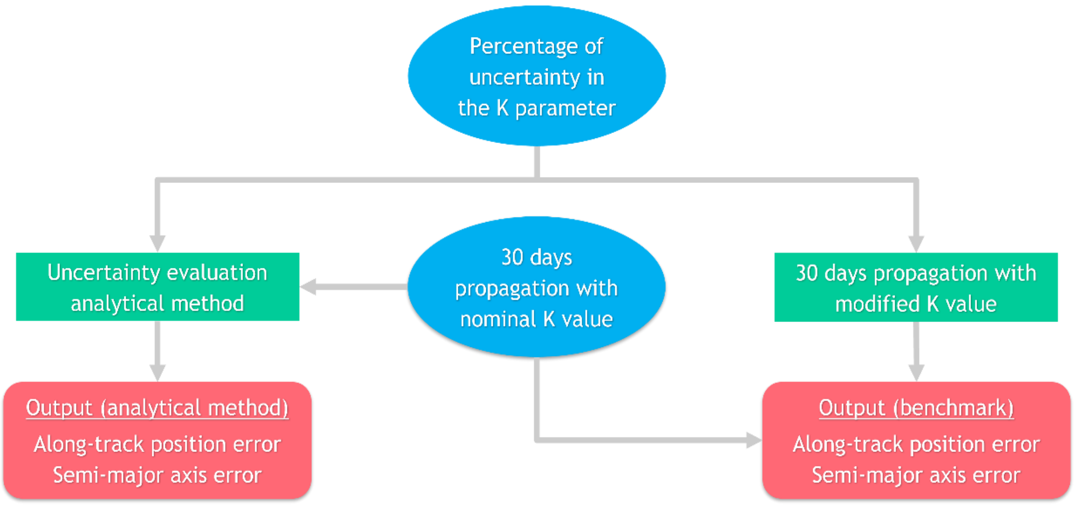


Figure 38 Workflow of the analyses carried out to test the algorithm

The performance of the algorithm is evaluated based on accuracy, i.e., its capability to provide values of the errors comparable to those of the benchmark and trustworthy trends of the error curves, and computational cost. In particular, the performance parameter selected is the relative error between the errors evaluated through the analytical method and those obtained by propagation, i.e., the benchmark.

The relative error, ε, is computed as

$$\varepsilon = \frac{X_{analytic} - X_{prop}}{X_{prop}}, \tag{4.9}$$

where $X_{analytic}$ is the along-track position error (or the semi-major axis error) estimated through the analytical method and $X_{prop}$ the same quantity obtained using propagation. The relative error is than multiplied by 100 to obtain the percentage error.

**Test case 1**

The test case 1 (TC1) is about the Object 1 of Table 24. It features the object orbiting at the lowest altitude, i.e., at around 450 km, in which the impact of the atmospheric drag perturbation is greater, and also the effects of the differential drag caused by a ballistic coefficient uncertainty are more evident. The along-track position errors of the analytic method and the benchmark are reported in Figure 39 for the four levels of *K* uncertainty.

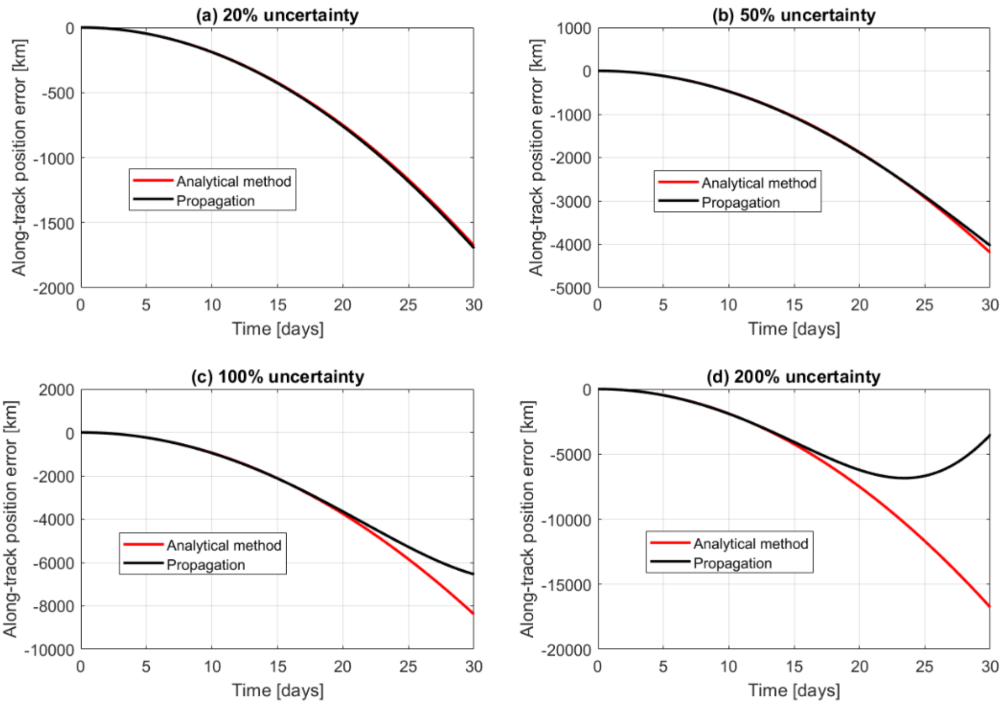


Figure 39 Time evolutions of the along-track position errors evaluated using the analytical method (red) and the propagation (black) in the 20% (a), 50% (b), 100% (c) and 200% (d) uncertainty cases for TC1.

From Figure 39, it can be noted how the trends of the along-track error evaluated using the analytical method are quite consistent with those of the benchmark for the 20% and 50% uncertainty cases. When the uncertainty is 100% (Figure 39c), the curve starts to diverge from the benchmark after about 20 days. Indeed, the curve of the benchmark presents an inflection point and change from concave downward to concave upward around the 25$^{th}$ day, while the curve of the analytical method does not show this behavior. The phenomenon is emphasized in the 200% uncertainty case (Figure 39d). Here, significant differences between the analytical method and the numerical propagation can be noticed after about 15 days, and, in particular, the derivative of the numerical along-track error changes its sign after about 23 days. This phenomenon can be explained considering the position that the fictitious object occupies in the local RSW reference frame centered in the real object, i.e., the nominal object. Indeed, it is intuitive that as the angular separation between the objects grows, the along-track component of the fictious object's position oscillates around zero.

While this behavior remains “hidden” in the other cases, it is evident in the highest uncertainty case because the angular separation becomes very high (higher than 90°). For the sake of clarity, the trends of the along-track angular separation, i.e., the error in the argument of latitude, computed using the analytical method is shown in Figure 40. While the angular separation is never higher than 70° in the first three uncertainty cases, it reaches around 140° in the last case. In particular, around the 24$^{th}$ day, the angular separation is around 90° and it corresponds to the highest value of the along-track error magnitude (Figure 39d).

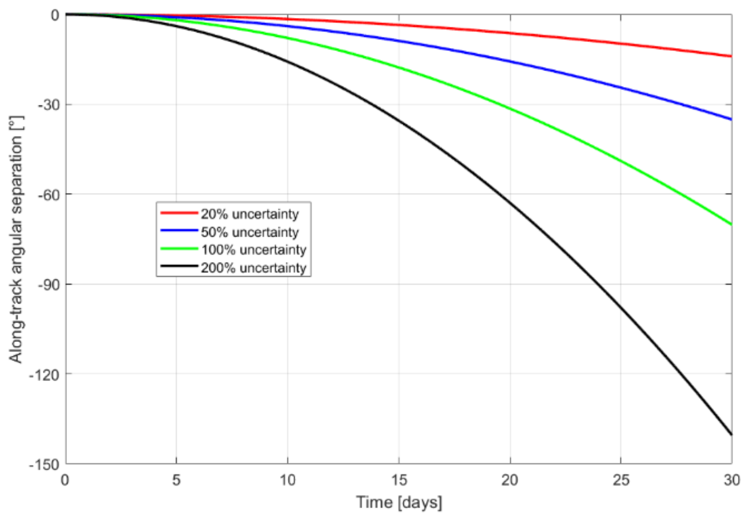


Figure 40 Time evolutions of the along-track angular separation computed using the analytical method in the 20% (red), 50% (blue), 100% (green) and 200% (black) uncertainty cases for TC1.

In Figure 41, instead, the percentage relative error between the along-track separation evaluated with the analytical method and the benchmark is shown, for the first three uncertainty cases. At this altitude, there is an evident degradation of the method performance over time. However, the method estimates reasonably well, i.e., percentage error less than 5%, the along-track error trend for at least 20 days, as long as the uncertainty in the *K* parameter is within 100%.

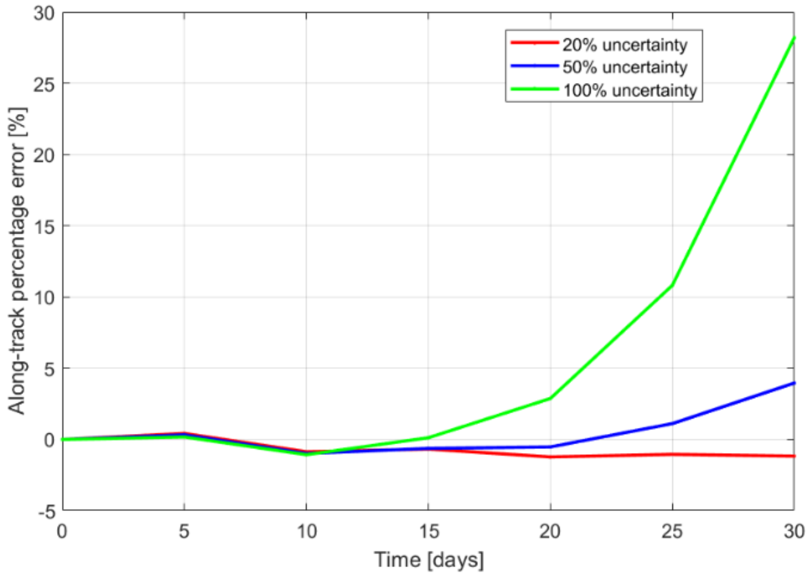


Figure 41 Time evolution of the percentage error in the along-track separation in the 20% (red), 50% (blue) and 100% (green) uncertainty cases for TC1.

As for the radial error, i.e., the accumulated error in the semi-major axis, its trend for the different uncertainty cases is plotted in Figure 42 and compared to that obtained using numerical propagations. In this case the trends of the errors are linear, and it can be noted that the analytical method always tends to slightly underestimate the magnitude of the error. The percentage errors related to the semi-major axis error are shown in Figure 43 for all the uncertainty cases. They are always lower than 10%, which represents an acceptable value for the semi-major axis error, thus proving the good performance of the analytical method in estimating the radial error also at low altitude and even in the 200% uncertainty case.

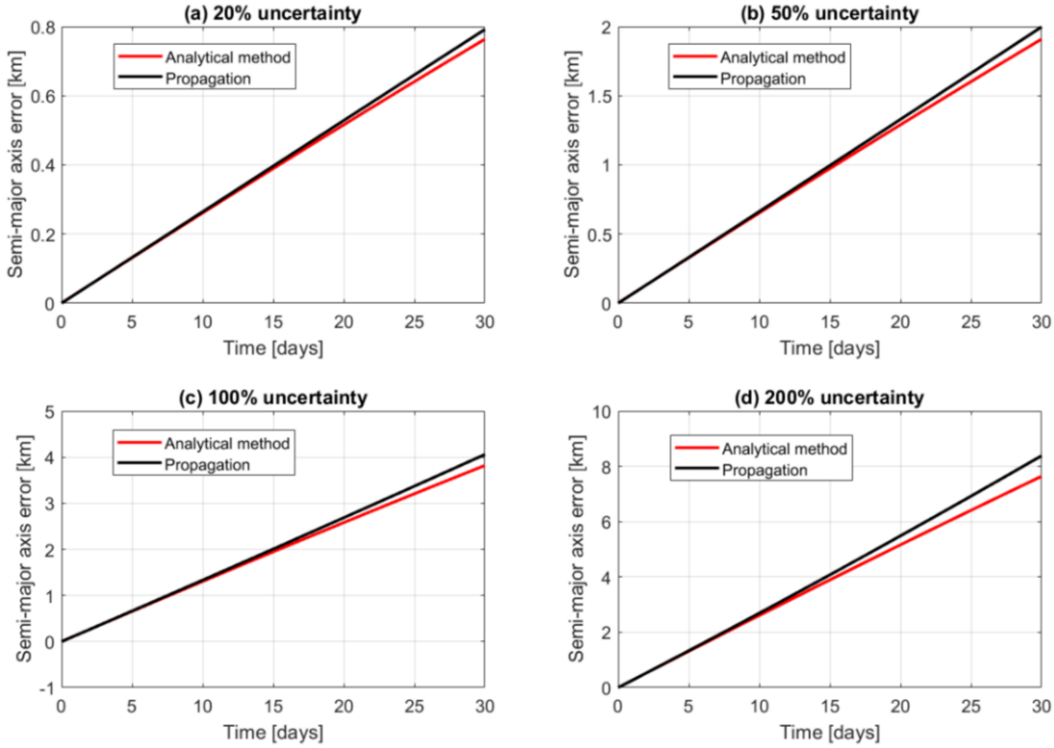


Figure 42 Time evolutions of the semi-major axis errors evaluated using the analytical method (red) and the propagation (black) in the 20% (a), 50% (b), 100% (c) and 200% (d) uncertainty cases for TC1.

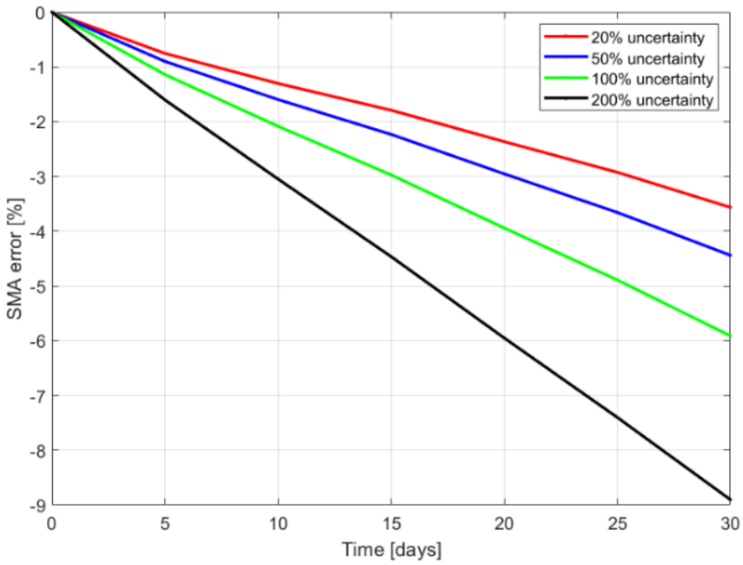


Figure 43 Time evolutions of the percentage error in the semi-major axis variation in the 20% (red), 50% (blue) and 100% (green) uncertainty cases for TC1.

**Test case 2**

In the test case 2 (TC2), the Object 2 of Table 24 is considered for the analysis, with an altitude between 500 and 600 km. The results of the analytic method in terms of time evolutions of the along-track separation and semi-major axis error are reported respectively in Figure 44 and Figure 45, also compared to those of the benchmark.

Figure 44 shows that the curves are very similar for uncertainties up to 100% and almost overlapped in the 20% and 50% uncertainty cases. Only for the 200% uncertainty case, the analytic along-track error diverges over 5% after around 26 days. However, the magnitude of the along-track error estimated using the analytical method is always larger with respect to the benchmark, thus resulting in an overestimation of the error.

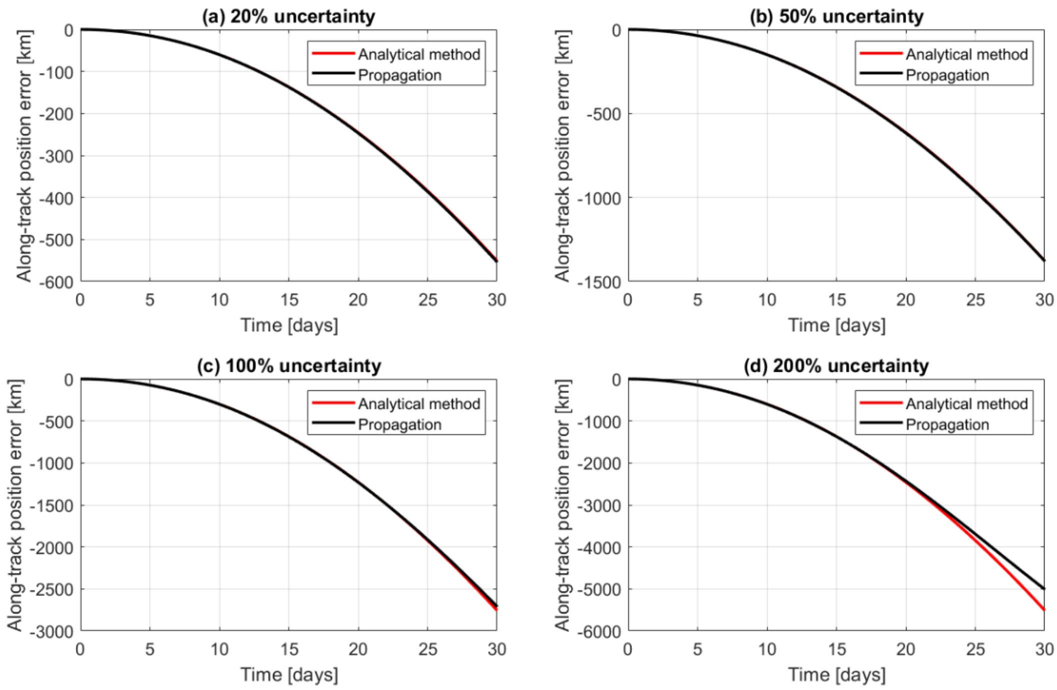


Figure 44 Time evolutions of the along-track position errors evaluated using the analytical method (red) and the propagation (black) in the 20% (a), 50% (b), 100% (c) and 200% (d) uncertainty cases for TC2.

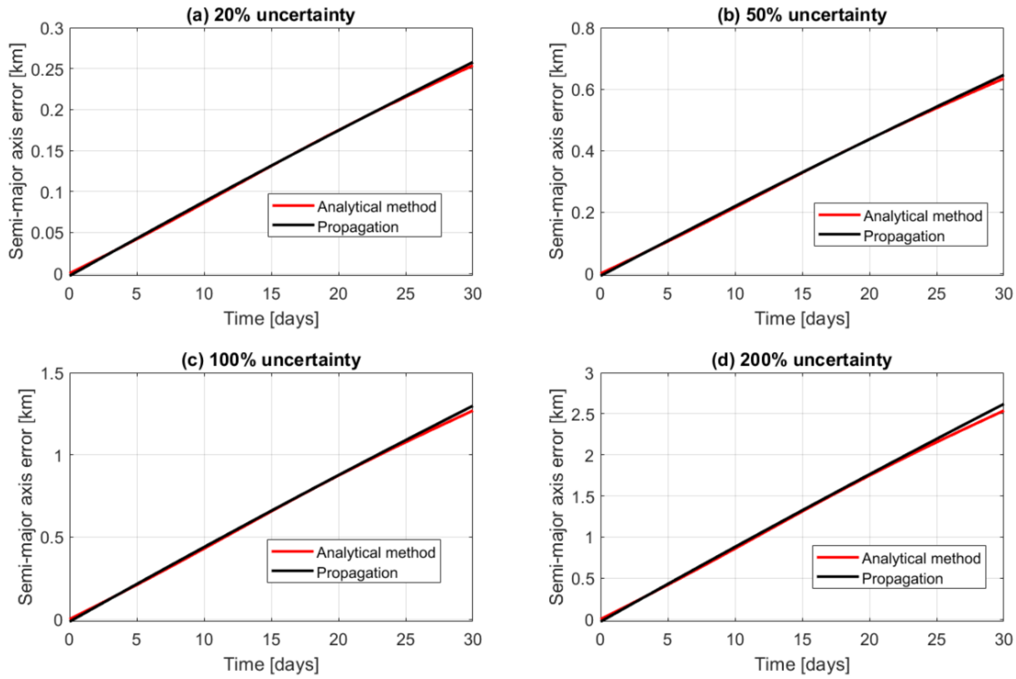


Figure 45 Time evolutions of the semi-major axis errors evaluated using the analytical method (red) and the propagation (black) in the 20% (a), 50% (b), 100% (c) and 200% (d) uncertainty cases for TC2.

Although this conservative nature of the method may imply computational issues in some applications, it can be useful when applied to operative context in which a medium-term collision frequency screening is needed, and it is important not to lose information about potential risk. On the contrary, the trends of the semi-major axis error shown in Figure 45 exhibit a small underestimation with respect to the benchmark, which grows for increasing uncertainty in the $K$ parameter. These small misestimations are easily deduced from the time evolution of the percentage errors of both the along-track separation (Figure 46) and the semi-major axis error (Figure 47). For the former, the percentage error is around zero for the 20% and 50% uncertainty cases, less than 2% in the 100% uncertainty case and reaches a maximum of 10% in the most extreme uncertainty case. Regarding the latter, instead, trends similar to each other can be observed for varying percentages of uncertainty, with a maximum value of 3% in the 200% case.

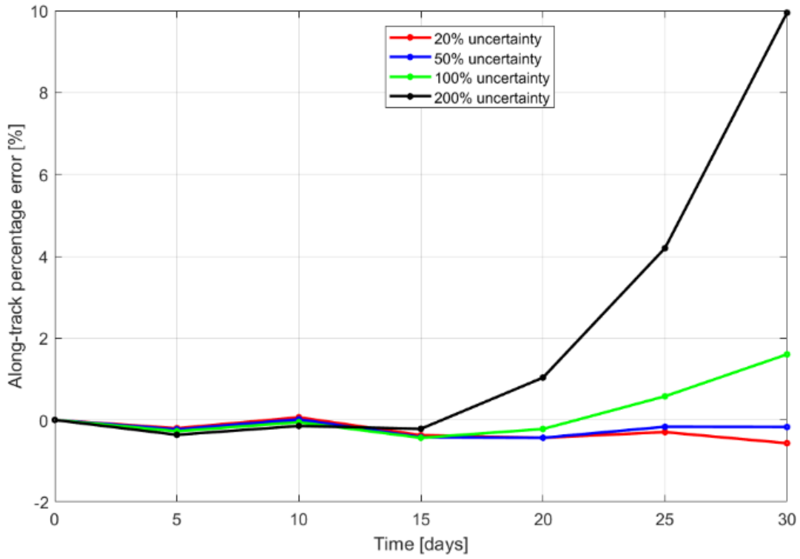


Figure 46 Time evolutions of the percentage errors in the along-track separation in the 20% (red), 50% (blue), 100% (green) and 200% (black) uncertainty cases for TC2.

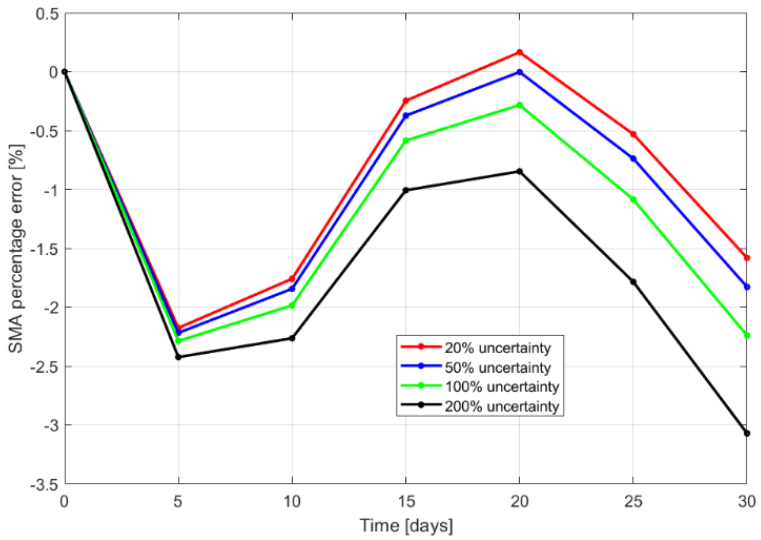


Figure 47 Time evolutions of the percentage errors in the semi-major axis variation in the 20% (red), 50% (blue), 100% (green) and 200% (black) uncertainty cases for TC2.

**Test case 3**

The test case 3 (TC3) deals with the Object 3 of Table 24, at an altitude around 640 km. The results in terms of along-track position error trends are shown in Figure 48 only for the 200% uncertainty case, since there are no appreciable differences between the analytical method and the benchmark in the other conditions.

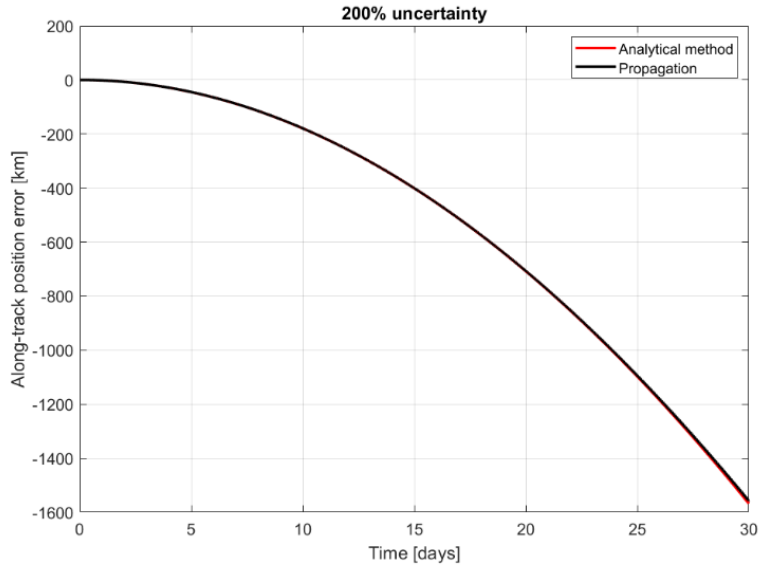


Figure 48 Time evolution of the along-track position error evaluated using the analytical method (red) and the propagation (black) in the 200% uncertainty case for TC3.

Also in the 200% uncertainty case, the difference between the two curves is small and the maximum value of the percentage error is around 0.7% after 30 days, as shown in Figure 49. A very slight overestimation of the error is still present, as for the previous test cases, but its magnitude reduces as the altitude grows.

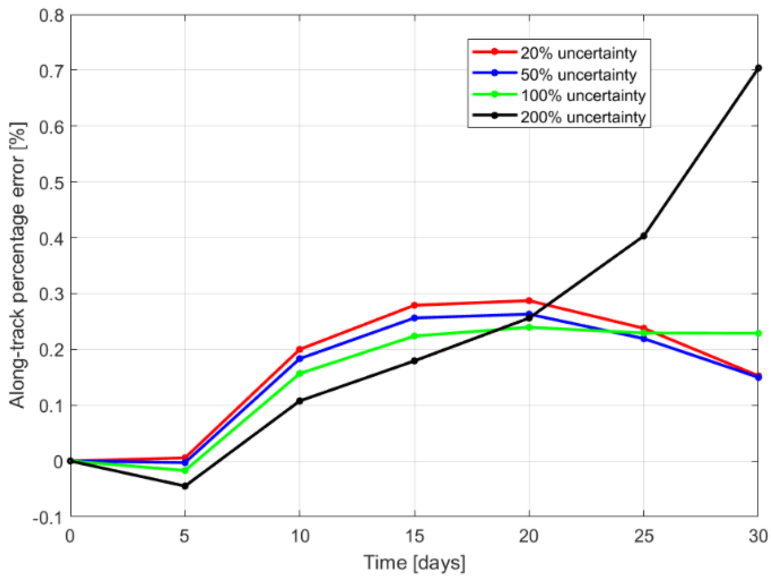


Figure 49 Time evolutions of the percentage errors in the along-track separation in the 20% (red), 50% (blue), 100% (green) and 200% (black) uncertainty cases for TC3.

The same applies to the semi-major axis error, whose time evolution is plotted in Figure 50 only for the 200% uncertainty scenario. As in the previous test cases, there is a small underestimation of the final radial error, as shown also by Figure 51, which depicts the trends of the percentage error of the semi-major axis variation. The percentage error is always lower than 1% and reduces as the $K$ uncertainty decreases.

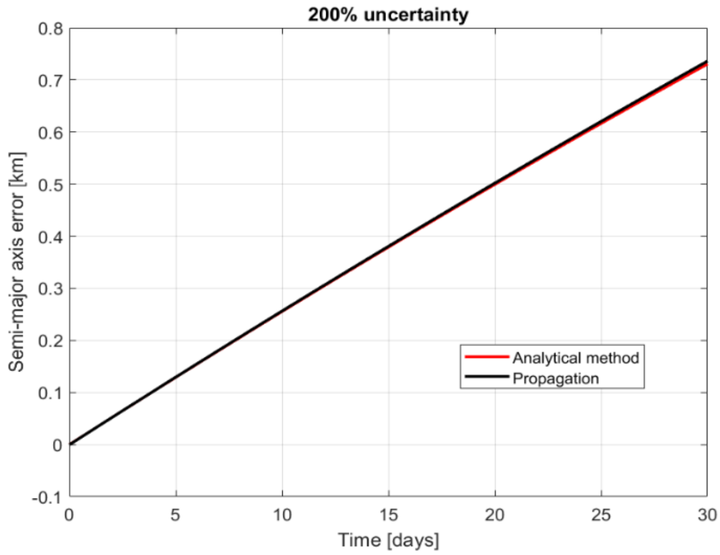


Figure 50 Time evolution of the semi-major axis error evaluated using the analytical method (red) and the propagation (black) in the 200% uncertainty case for TC3.

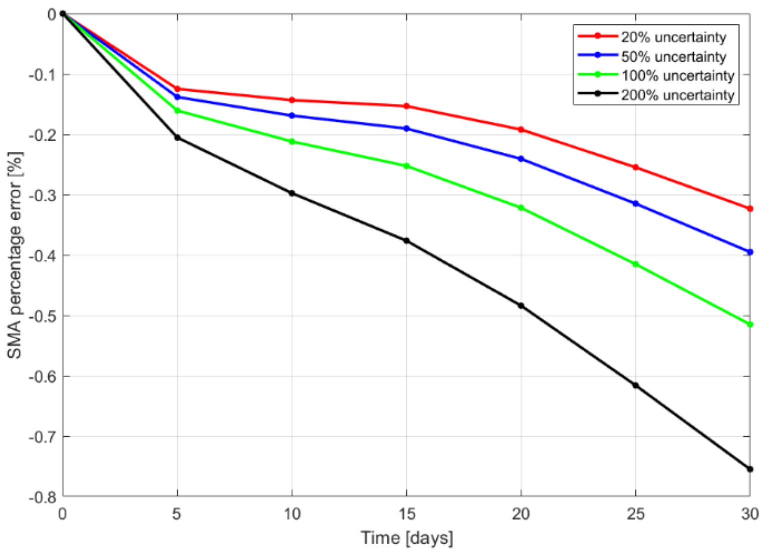


Figure 51 Time evolutions of the percentage errors in the semi-major axis variation in the 20% (red), 50% (blue), 100% (green) and 200% (black) uncertainty cases for TC3.

**Test case 4**

Object 4 of Table 24 is considered for the test case 4 (TC4). The altitude is around 760 km, which is in the most crowded region of the LEO environment. At this altitude, the more rarefied atmospheric density causes the drag perturbation to be comparable to other perturbations, i.e., Solar Radiation Pressure (SRP), so the impact of a ballistic coefficient uncertainty is less significant and, consequently, less appreciable. However, the analytical method confirms its good performance also in this orbital regime. Since there are no noticeable differences between the along-track separation trends and semi-major axis trends of the two adopted methods, only the evolution of their percentage errors is reported for this test case in Figure 52 and Figure 53. The along-track separation percentage errors follow the same trend in all the uncertainty scenarios, with final errors of less than 0.1%. Small differences between the uncertainty cases are probably due to the effect of the SRP perturbation. Since SRP acts in the anti-solar direction, its contribution distributes itself over the three position components and not only in the along-track direction. Therefore, in some circumstances, uncertainties in the $K$ value could cause a differential SRP, which may have “positive” effects on the along-track position error, thus slightly reducing the error accumulated due to differential drag. Figure 53, instead, shows again a small underestimation of the semi-major axis error, but its magnitude drops down of almost one order, with final errors ranging from -0.1 to -0.2%.

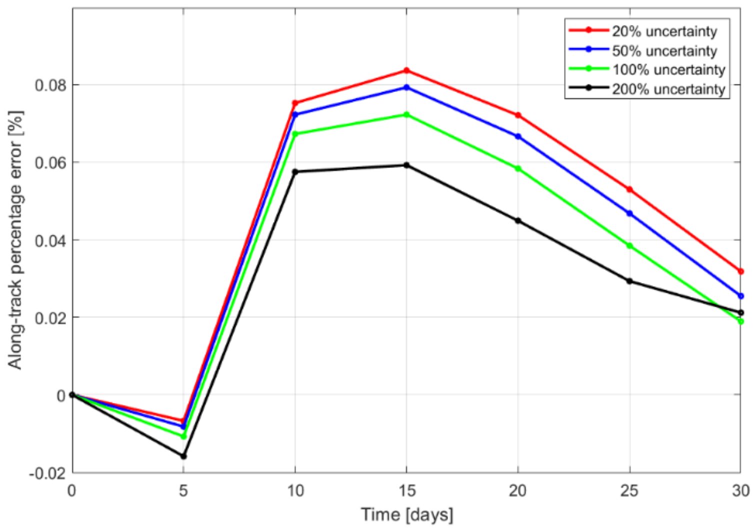


Figure 52 Time evolutions of the percentage errors in the along-track separation in the 20% (red), 50% (blue), 100% (green) and 200% (black) uncertainty cases for TC4.

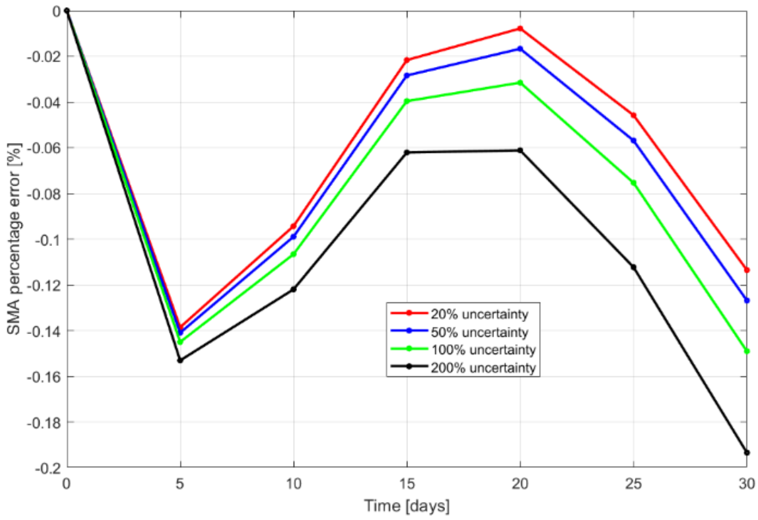


Figure 53 Time evolutions of the percentage errors in the semi-major axis variation in the 20% (red), 50% (blue), 100% (green) and 200% (black) uncertainty cases for TC4.

To sum up, the results suggest that the prediction performance of the method clearly improves for increasing orbit altitude, being also less significant the effect of the differential drag perturbation. Therefore, while the method always shows very good accuracy for altitudes higher than 600 km, at lower altitudes its usage should be limited to less than 30 days when the involved uncertainty is equal or higher than

100%, In these cases, around the 25th day, the estimated error starts to diverge too much with respect to the benchmark error, i.e., the error evaluated comparing propagations run with nominal and modified *K* values. However, it should be noted that, in such situation, the method always overestimates the error due to the input uncertainty. This behavior could be convenient if the tool is applied in an operative context in which the collision frequency of assets of interest must be foreseen. Indeed, in such application, the tool can provide propagation error boundaries based on the uncertainties involved and give them as input to algorithms performing medium-term collision risk assessment. A conservative estimation of the errors can be useful in such context not to lose information about potential risk, even if it could imply an increase of the computational time.

## 4.3 Sensor Calibration

In this section, a calibration tool able to carry out the metrological characterization of ground-based sensors is presented. After setting up information about the sensor, such as position, type of sensor (i.e., telescope, radar or laser) and coordinate system in which the observations are represented, the tool acquires data from available Tracking Data Messages (TDMs) and Orbit Ephemeris Messages (OEMs) relevant to reference satellites and the residuals for the metric observations are computed.

### 4.3.1 Reference frames and notation

Before going into the details of the calibration tool, the adopted reference frames and notation shall be specified. The position of the sensor, initially expressed in geodetic coordinates, i.e., longitude $\lambda$, latitude $\varphi$ and altitude $h$, is transformed into the ECEF reference frame and then in the ECI reference frame using routines of the NASA's SPICE toolkit. Depending on the type of sensor, the observations can be expressed in two different coordinate systems, i.e., topocentric equatorial (TE) or topocentric horizontal (TH) reference frames. The TE coordinate system has the origin at a point on the surface of the Earth (e.g., the sensor's location) and its nonrotating set of axes is parallel to the XYZ axes of the ECI reference frame. In the TH coordinate system, the origin is at a point on the surface of the Earth, the y-axis points towards East, the z-axis is parallel to the local vertical and the x-axis completes the right-handed set and points South. The positions and velocities of the ephemerides are expressed in the ECI reference frame. Therefore, the latter must be transformed in topocentric coordinates and the strategy changes according to the coordinate system:

- If the sensor is a telescope, the reference frame of the observations is the topocentric equatorial and the measurements are the right ascension and declination angles; in this case, only a translation of the origin from the

Earth center to the sensor's location is needed to express the state vectors of the ephemerides in the same reference frame as the observations.

- If the sensor is a radar (or a laser), the reference frame of the observations is the topocentric horizontal and the measurements are the azimuth and elevation angles, range, and range rate; in this case, the state vector from OEM is firstly expressed in the topocentric frame by translating the origin from the Earth center to the sensor's location. Then, a transformation is needed from topocentric equatorial to topocentric horizontal, obtained by means of a 321 sequence of Euler angles: the first angle equal to λ, the second angle of (90° - φ) and the third angle equal to 0.

Furthermore, also the position error in the RSW reference frame is evaluated. The position error vector is calculated as the difference between the measured vector and the actual vector computed from the ephemerides and then it is rotated from ECI to RSW, expressing its components along the radial, along-track and cross-track directions, to determine how the error is distributed.

As for the definition of the angles, the azimuth $\beta$ is the angle between the North of the topocentric horizontal reference frame and the projection of the position vector in the $xy$ plane, while the right ascension $\alpha$ is the angle between the $x$-axis of the topocentric equatorial reference frame and the projection of the position vector in the $xy$ plane. As for the elevation $\varepsilon$, it is the angle between the $xy$ plane of the topocentric horizontal/equatorial and the position vector, while the declination $\delta$ is the angle between the $xy$ plane of the topocentric equatorial and the position vector. The range $R$ is the distance between the sensor's site and the observed target, and the range rate $\dot{R}$ is the rate at which $R$ is changing with respect to time. The residuals are referred to as ΔX, where X can be any of the measured parameters, and they are to be intended as

$$\Delta X = X_{obs} - X_{calc}, \tag{4.10}$$

where $X_{obs}$ is the measurement of the sensor and $X_{calc}$ is the corresponding parameter computed from the ephemerides. The latter represents the theoretical value that an ideal sensor located at the real sensor position should measure.

### 4.3.2 Description of the tool

As reported in [66], a simple method to characterize a measurement is to assume it has a Gaussian distribution with a time-constant non-zero mean. Clearly, the mean, $\mu$, standard deviation, $\sigma$, and root mean square (RMS) represent main parameters of the distribution and are computed for the residuals of the parameters of interest. The parameters considered for the calibration are range, range rate and azimuth and elevation angles, if the sensor is a radar or a laser. Instead, right ascension and declination angles are used if the sensor is a telescope. The general scheme of the sensor calibration tool is summarized by the flow chart in Figure 54.

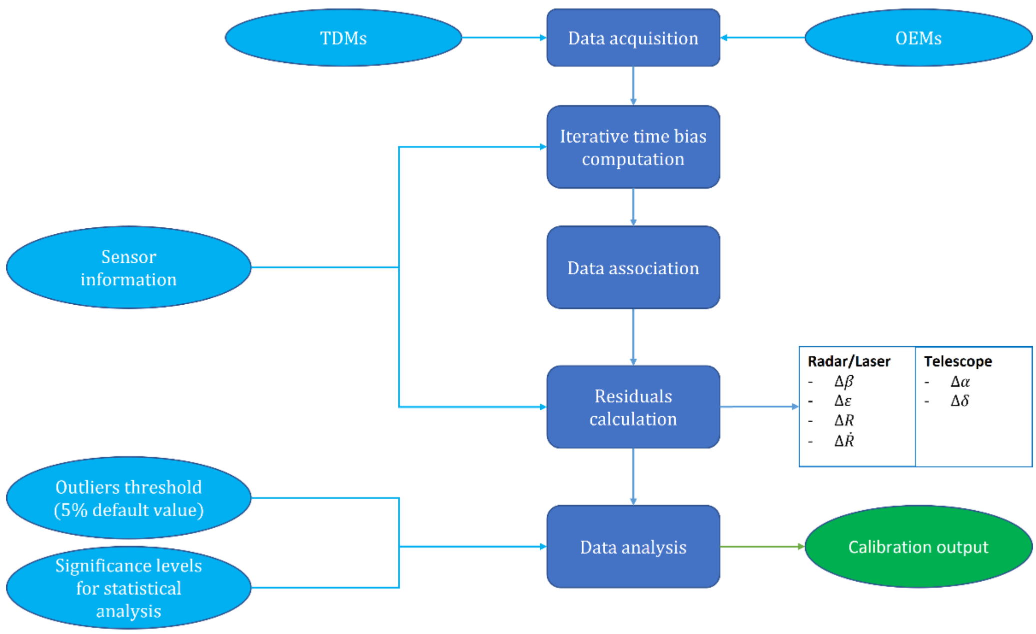


Figure 54 Workflow of the sensor calibration tool for a telescope. In case of radar/laser sensor, the time bias computation is not performed and the data are directly associated after the acquisition phase.

The tool receives the following inputs:

- Sensor information: type (radar, optical or laser), WGS84 coordinates (latitude, longitude and altitude) and coordinate system in which the observation parameters are represented (topocentric equatorial or topocentric horizon);
- TDMs generated by the sensor;

- Reference OEMs associated to the TDMs;
- Outliers percentage threshold;
- A priori sensor error statistics from previous calibrations (optional);

After the data acquisition, if the sensor is a telescope, the first step is the computation of the time bias (TB) of the sensor using an iterative process based on the minimization of the mean of the along-track error, $\mu_{AT\_err}$, which is an index of how much the observation epoch is ahead or delayed with respect to the actual epoch of the object's passage. A description of this process is presented later in this section.

Then, for each observation in the TDMs, the corresponding ephemerides in the OEMs are identified, based on the object designator, i.e., NORAD ID. To correctly associate the available ephemerides to the TDM observables, the state vector at the time instant closest to the observation epoch is extracted from the OEMs and it is propagated from ephemeris epoch to observation epoch. The propagations are carried out using the numerical propagator presented in Chapter 3. Being accurate ephemerides needed for the calibration process, all the perturbations are considered for this application, but limiting to 20 the harmonics of the Earth's gravity field in order to speed up the propagations.

However, before starting the propagation step, it is necessary to check if the observations in the TDMs are suitable for association with the available ephemeris data. Specifically, all the measurements within a TDM whose epoch is outside the time span $[T_0 - \tau, T_1 + \tau]$, where $T_0$ and $T_1$ are the epochs of the first and last available ephemeris, respectively, must be discarded. $\tau$ is a tolerance parameter whose value must be set considering the frequency of the ephemerides and the accuracy and reliability of the selected propagator.

After associations between observations in the TDMs and ephemerides in the OEMs are determined, the state vector information are converted into angles and, eventually, range and range rate information as explained before, depending on the type of sensor. Finally, correction of diurnal and annual aberration is performed if needed, and the residuals are evaluated as shown by equation (4.10).

Then, the presence of any anomalous measurements is checked, and the possible outliers are removed. To do so, a region of acceptance is defined and any residual falling outside of this region is considered anomalous and removed. There are two possible procedures:

1. If a priori information from previous calibrations is available, an acceptance region is formulated as [μ - 3σ, μ + 3σ], where μ is the aprioristic bias and σ is the aprioristic standard deviation

2. If a priori information is not available, an iterative method is used: the acceptance region is formulated as [μ - kσ, μ + kσ], where $\mu$ is the mean of the set of residuals, $\sigma$ its standard deviation, and $k$ is a user-defined width parameter. At each iteration, the mean and standard deviation are re-calculated and possible outliers are discarded. The iteration stops when no element is removed from the set.

The number of outliers is computed and the percentage of outliers with respect to the number of observations used is evaluated. A warning is generated if the percentage exceeds the user-selected threshold.

**Iterative method for time bias computation**

As regards the iterative process for the TB computation, the minimization of the along-track error is performed with a simple bisection method: it starts by computing $\mu_{AT\_err}$ considering a null TB, and then considering two extreme guess values, $TB = -1\ s$ and $TB = 1\ s$. Depending on the signs of the $\mu_{AT\_err}$ values, the bisection is applied in the [-1 s, 0 s] or the [0 s, 1 s] interval. Then, the bisection method goes on until the difference between the along-track errors means evaluated at the updated interval extremes is below a user-defined threshold. The flowchart of the bisection method is shown in Figure 55. Once the optimum TB has been identified, the TB correction is applied to the observation epochs to correctly associate the TDMs and OEMs data, thus finally computing the residuals of the calibration parameters. Clearly, at each iteration of the bisection method, and so for each guess value of the time bias, association of TDM and OEM data should be performed and residuals should be evaluated to compute the mean of the along-track error, as depicted in Figure 56.


Figure 55 Flowchart of the iterative bisection method for time bias computation

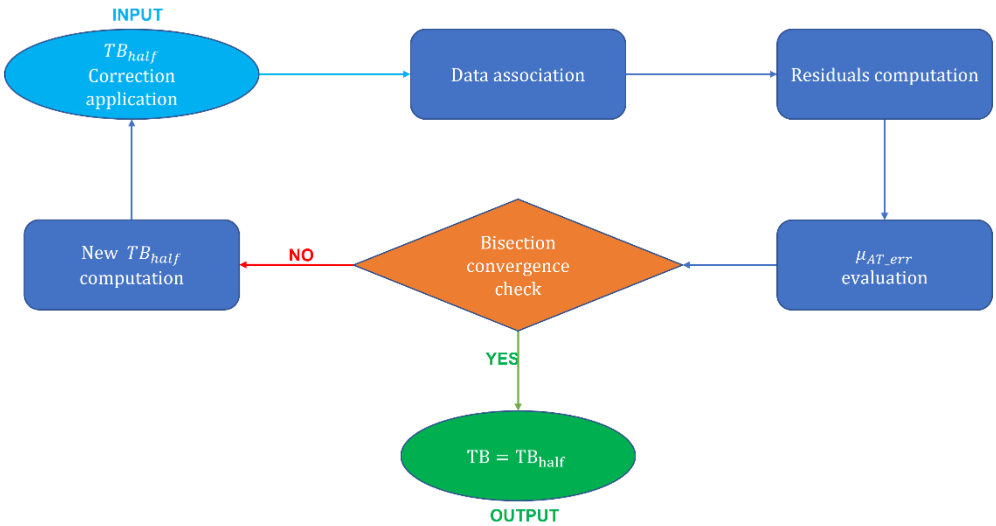


Figure 56 Flowchart of logic process of an iteration of the bisection method

### 4.3.3 Performance assessment of the sensor calibration tool

In this section the performance assessment of the sensor calibration tool is carried out, by showing the results of two different test cases using real data, one for a radar sensor calibration and the other for a telescope calibration. For both test cases, no a priori information for biases and noises of the measurements was available, so the second method for the removal of the outliers is implemented. With regards to the numerical propagation, all the available perturbations have been included, considering harmonics up to 20x20 for the gravity model, the Jacchia-Roberts as density model, being less demanding from a computational point of view, and both Sun and Moon as third bodies.

**Test case 1 (radar)**

The number of available tracks, i.e., TDMs, is 9, of which 4 are referred to the METOP-2 satellite and 5 to METOP-1, for a total of 182 available observations. The available OEMs instead are 8, four for each satellite. However, the epochs of two TDMs associated to METOP-2 and three TDMs of METOP-1 are outside the time span of the respective OEMs. Thus, these TDMs are discarded by and only 4 TDMs, i.e., two for each satellite containing 69 observations, and the corresponding OEMs are considered for the calibration process. Each TDM reports observations over a time span slightly longer than one minute. However, for the sake of simplicity and clarity in the subsequent plots, a number from 1 to 4 is assigned to each TDM chronologically and the related observations are grouped at the same epoch, which is the first epoch of the corresponding TDM. The relative UTC epochs are listed in Table 26.

Table 26 Reference epochs and satellites of the TDMs of the first test case

| TDM | Satellite | UTC Epoch |
|---|---|---|
| 1 | METOP-2 | 04/08/2020 20:34:50.910 |
| 2 | METOP-2 | 05/08/2020 20:13:52.766 |
| 3 | METOP-1 | 04/09/2020 09:49:32.707 |
| 4 | METOP-1 | 04/09/2020 21:07:44.445 |

A comparison between the azimuth and elevation observations from TDMs and the same parameters computed from the OEMs is presented in Figure 57. The data are well separated, and it is not difficult to distinguish observations from different TDMs, except for the central cloud, where some measurements coming from two different TDMs tend to overlap.

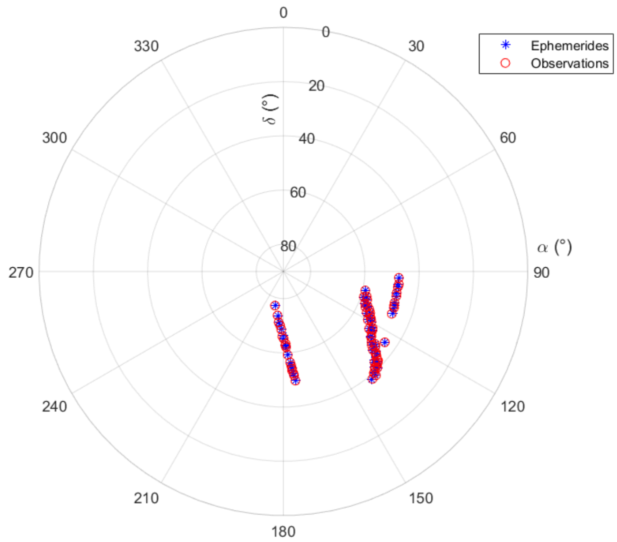


Figure 57 Comparison between measurements and ephemerides in terms of azimuth ($\beta$) and elevation ($\varepsilon$)

The distribution of the residuals of azimuth, elevation, range, and range rate for the different TDMs are shown in Figure 58. The means (μ) and the standard deviations (σ) of the residuals for each TDM are instead reported in Table 27.

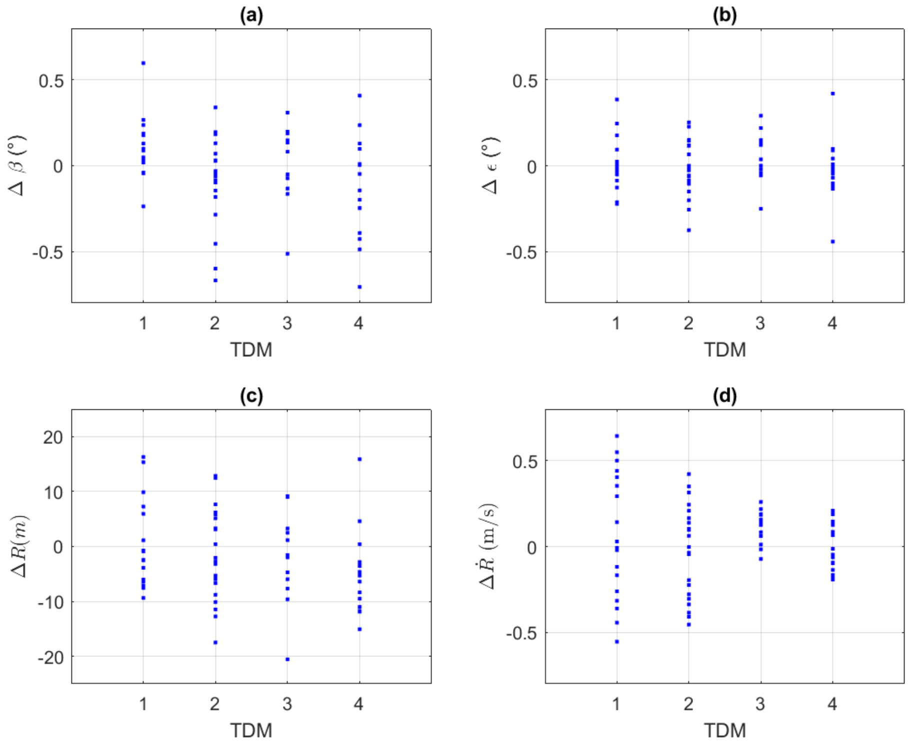


Figure 58 Distributions of the azimuth (a), elevation (b), range (c), and range rate (d) residuals for each TDM

Table 27 Statistics of the residuals for each TDM for the first test case

| **TDM** | **Δ $\beta$ (°)** | | **Δ $\varepsilon$ (°)** | | **Δ $R$ (m)** | | **Δ $\dot{R}$ (m/s)** | |
|---|---|---|---|---|---|---|---|---|
| | **μ** | **σ** | **μ** | **σ** | **μ** | **σ** | **μ** | **σ** |
| 1 | 0.11 | 0.17 | 0 | 0.15 | 0.11 | 7.78 | 0.06 | 0.37 |
| 2 | -0.09 | 0.25 | -0.01 | 0.15 | -1.47 | 8.47 | -0.03 | 0.27 |
| 3 | 0.01 | 0.22 | 0.04 | 0.14 | -2.24 | 8.31 | 0.11 | 0.10 |
| 4 | -0.12 | 0.29 | -0.03 | 0.17 | -6.07 | 8.81 | -0.03 | 0.14 |

It can be noted that the sensor performance is very similar for all the TDMs in terms of azimuth, elevation, and range rate, but there seems to be a degradation of the performance in the range measurements. In particular, there is an increase of the mean of the range residuals for the fourth TDM, although the value of the standard deviation is comparable to the others. The outputs of the calibration are summarized in Table 28.

The results are consistent with the values expected for a calibration of a SST radar and they are in the same order of magnitude of the residuals admissible to accept tracklets during a correlation process [131].

Table 28 Outputs of the radar calibration

| **Parameter** | **Constant bias** | **White noise sigma** | **RMS** |
|---|---|---|---|
| $\beta$ (°) | -0.028 | 0.251 | 0.251 |
| $\varepsilon$ (°) | -0.001 | 0.153 | 0.152 |
| $R$ (m) | -2.35 | 8.48 | 8.74 |
| $\dot{R}$ (m/s) | 0.021 | 0.256 | 0.255 |

The distribution of the error in the radial, along-track and cross-track direction of the RSW is shown in Figure 59, which also illustrates the distribution of the time residuals. Since the time residual is evaluated as the along-track error divided by the velocity, its distribution is identical to the along-track error distribution. The total time bias computed as the mean of the time residuals is 0.0757 s.

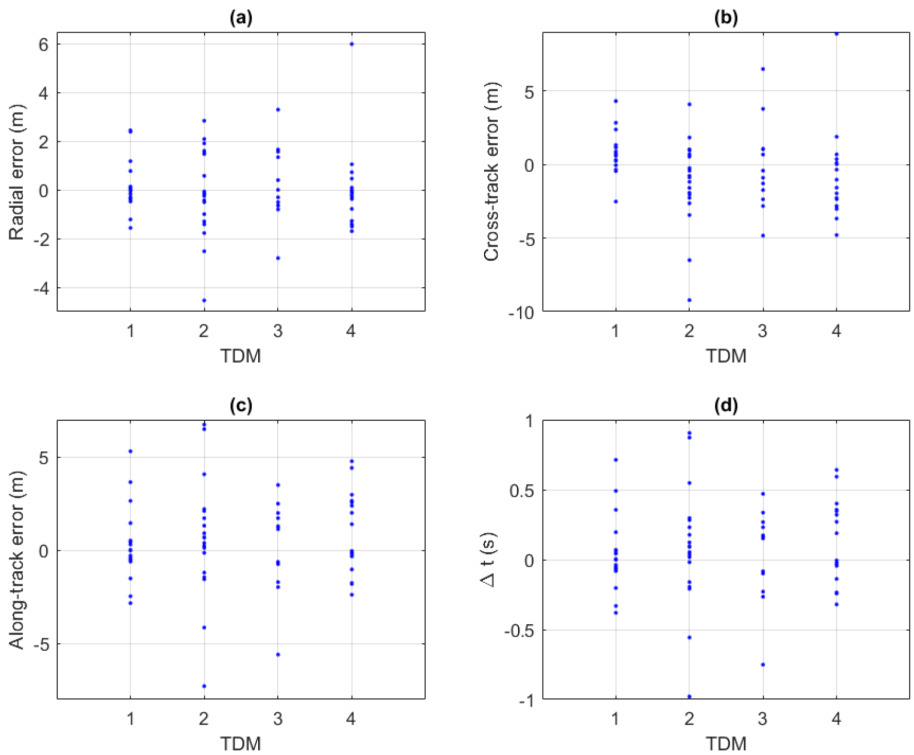


Figure 59 Distributions of the position error in the radial (a), cross-track (b) and along-track (c) directions and of the time residuals (d).

**Test case 2 (telescope)**

For this test case, 3 TDMs were available for a total of 197 observations. The sensor used for this calibration test is the PdM-Mite telescope, while the objects involved are two satellites of the GALILEO constellation, in particular two TDMs are referred to the GALILEO220 satellite (ID 43567) and only one TDM to GALILEO222 (ID 43565). Two OEMs were available, one for each object, both completely covering the epochs of the TDMs. The initial UTC epochs and the reference satellites of the TDMs are reported in Table 29.

Table 29 Reference epochs and satellites of the TDMs of the second test case

| TDM | Satellite | UTC epoch |
|---|---|---|
| 1 | GALILEO220 | 03/05/2021 19:04:44.091 |
| 2 | GALILEO220 | 04/05/2021 23:45:02.094 |
| 3 | GALILEO222 | 10/05/2021 23:04:10.105 |

The calibration time interval lasts from 03/05/2021 at 19:04:44.091 to 11/05/2021 at 00:23:02.080, for a total of about 7.22 days. After the data acquisition, the iterative method to compute the sensor time bias is applied, resulting in a time bias of 0.00188 s (1.88 ms) after 21 iterations. The time bias correction is implemented before proceeding with the data association. Once the data are associated, the residuals are evaluated and the outliers are removed using the second method presented in the previous Section, being a priori information not available. Of the 197 initial observations, only 3 outliers have been identified and removed, representing the 1.5%. As for the first test case, a comparison between the right ascension and declination observations from the TDMs and the same parameters computed starting from the OEMs is shown in Figure 60. Differences between ephemerides and observations are not appreciable and the tracks seem to be overlapping.

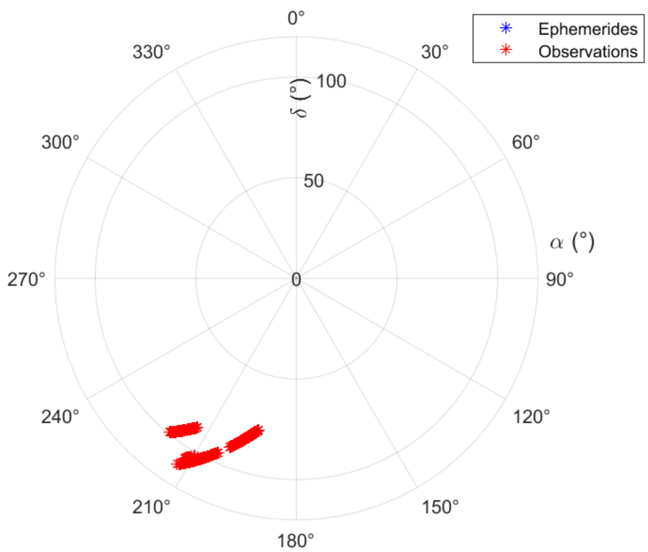


Figure 60 Comparison between measurements and ephemerides in terms of right ascension ($\alpha$) and declination ($\delta$)

The means, standard deviation and root mean square (RMS) error of the right ascension and declination residuals are reported in Table 30 for each TDM. For a clearer analysis of the right ascension residuals, the same are scaled for the cosine of the declination, thus analyzing the parameter ($\alpha \cos \delta$) to evaluate the statistics. The results are also shown in Figure 61. The three TDMs have shown similar results in terms of residuals, although they contained quite different numbers of observations, the third TDM being the most numerous including 136 observations. The final results of the calibration in terms of RMS of the residuals are summarized in Table 31. The residuals are quite low and in agreement with the EU SST requirements for MEO telescopes, which require the telescopes of the EU sensors networks to have residuals lower than 2 arcsec.

Table 30 Statistics of the residuals for each TDM for the second test case

| **TDM** | **$\Delta$ ($\alpha \cos \delta$) (°)** | | | **$\Delta\ \delta$ (°)** | | |
|---|---|---|---|---|---|---|
| | **μ** | **σ** | **RMS** | **μ** | **σ** | **RMS** |
| 1 | 1.63e-04 | 3.43e-04 | 3.77e-04 | 4.11e-05 | 5.68e-04 | 5.63e-04 |
| 2 | -1.95e-04 | 2.89e-04 | 3.40e-04 | 4.37e-05 | 4.42e-04 | 4.27e-04 |
| 3 | -3.85e-05 | 4.32e-04 | 4.32e-04 | -4.89e-05 | 4.51e-04 | 4.52e-04 |

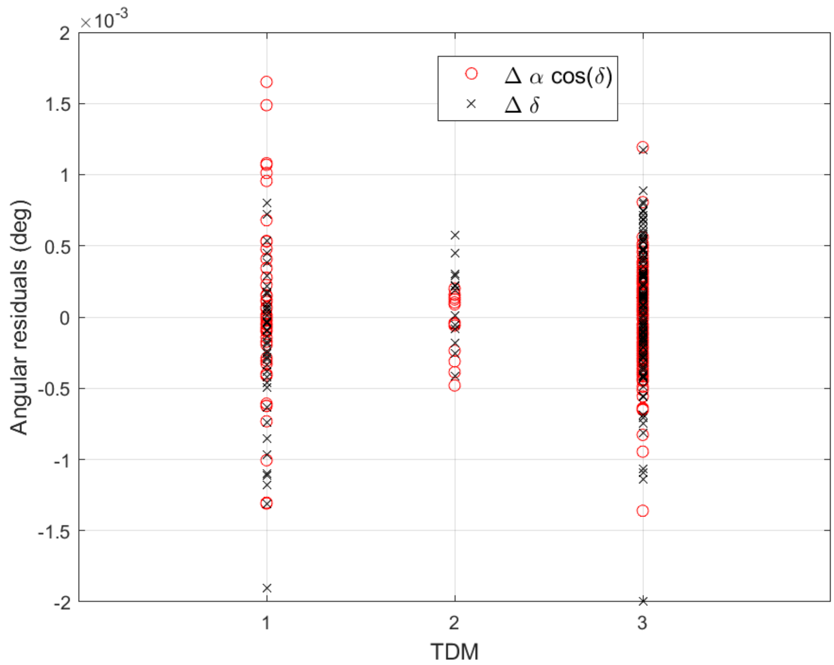


Figure 61 Distributions of the residuals of right ascension scaled for the cosine of the declination (red circle) and declination (black cross) for each TDM of the second test case

Table 31 Outputs of the telescope calibration

| **Parameter** | **RMS** | |
|---|---|---|
| | **(°)** | **(arcsec)** |
| $\Delta(\alpha \cos\delta)$ (°) | 4.138e-04 | 1.489 |
| $\Delta\delta$ (°) | 4.787e-04 | 1.723 |

## 4.4 Analysis of AOI overflights

This section presents the description of an algorithm developed for RSP applications, as part of an integrated RSP architecture, to evaluate whether a satellite overflights and/or observes an Area of Interest (AOI) in a given timespan, thus eventually identifying the entry and exit epochs and latitude and longitude coordinates. The workflow of the algorithm is reported in Figure 62.

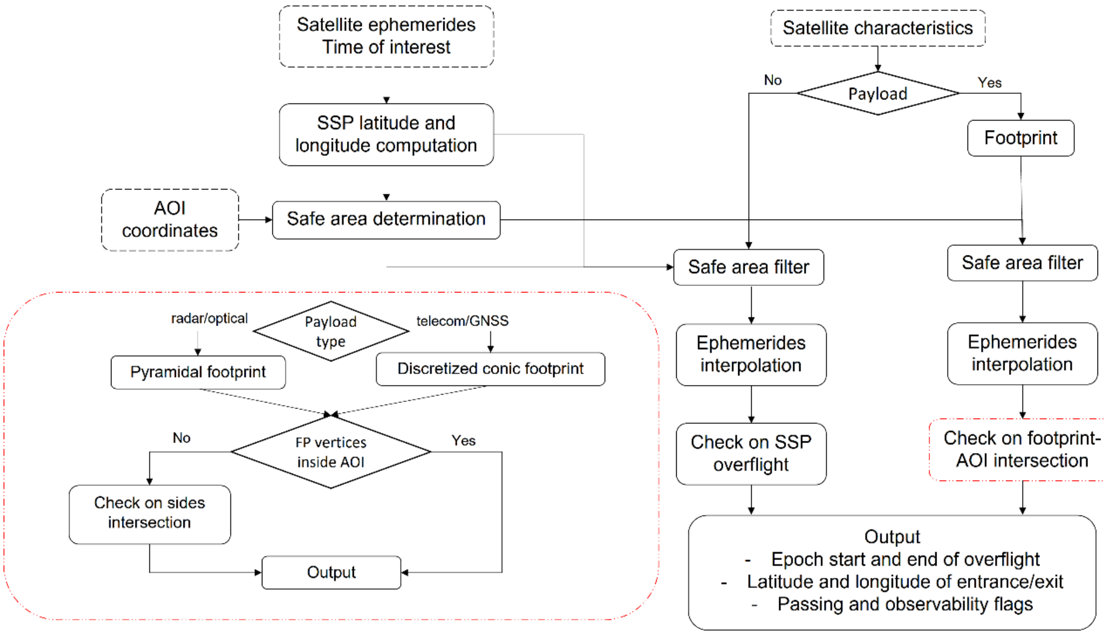


Figure 62 Workflow of the AOI overflight algorithm

The algorithm takes as input:

- Ephemerides of a satellite of interest for the analysis;
- Initial and final epochs of the analysis;
- Satellite's payload information (if available);
- Latitude and longitude coordinates of the AOI vertices.

The outputs are:

- Epochs in which the satellites enters in and exits from the AOI;
- Latitude and longitude coordinates of the entry and exit points;

- Information about satellite operativity (passing/overflight)
- Information about AOI observability (for optical payloads)

Depending on the availability of satellite's payload information, the algorithm follows two different procedures: if payload information are not available, the analysis concerns the subsatellite point (SSP) and its AOI crossings within the timespan of interest (satellite passing over the AOI); if payload information are available, the analysis focuses on the intersections between the sensor's footprints and the AOI (satellite observing the AOI).

In both cases, the first step of the algorithm consists in building a "safe area", starting from the AOI received as input. This "safe area" is used as an initial filter, to focus the analysis on the timespans in which an AOI passing/observation is possible, thus reducing the computational cost. The "safe area" is always a rectangle containing the AOI in the longitude-latitude coordinate system. The "safe area" generation is realized as follows:

1. The rectangle that includes the initial AOI is built, considering the maximum and minimum values of longitude and latitude;
2. The rectangle dimensions are increased by values equal to the maximum variations of longitude and latitude between two consecutive time instants in the reference ephemerides.

**Case A – Payload information not available**

In this case, the work logic of the algorithm is the following:

1. The algorithm checks whether the SSPs obtained from the ephemerides fall within the safe area and, when a passing in the safe area is identified, the initial and final epochs of the passing are stored. This preliminary analysis is performed by means of a function, which takes as input the points to be checked and the vertices of the polygon representing the safe area and provides as output a vector of Boolean values (1 if the point is inside the polygon, 0 otherwise). This filter allows to identify rapidly the time intervals in which the AOI passing is possible, if any.

2. For each time interval, the timespan is discretized with a user defined time step, which is used to interpolate the position and velocity vectors of the ephemerides.
3. Latitude and longitude coordinates of the SSPs at each time step are computed and the check with the previously described function is performed again, but using the real AOI.
4. If one or more AOI overflights are identified, the algorithms outputs the initial and final epochs and the entry and exit latitude and longitude coordinates of each passing, thus setting the operativity flag to “passing”.

It is worth noting that, if the AOI is represented by a concave polygon, the SSP could exit the AOI and then re-enter shortly thereafter. In such situation, the algorithm considers two (or more) overflights and provides information for each one.

**Case B – Payload information available**

If the payload information are available, the algorithm performs the following steps:

1. First of all, the sensor’s footprint is evaluated for each time instant of the ephemerides, by using a function providing as output a matrix containing the latitude and longitude coordinates of the vertices of the footprint. The filter is realized by using the same function used for Case A, considering the footprint’s vertices as points and the safe area as polygon. It should be noted that, if the satellite’s payload is a radar or optical sensor, the footprint has 4 vertices. If the satellite is a telecom satellite or GNSS, the footprint would be a circumference, but it is discretized in 30 or 60 vertices respectively for the sake of coherence with the other types of payload. Also in this case, this step is required to filter out all the time intervals in which the AOI observation is not possible.
2. For each time interval, the timespan is discretized with a user defined time step, which is used to interpolate the position and velocity vectors of the ephemerides.
3. At each time step of the identified time intervals, the sensor’s footprint is evaluated. The strategy is the same regardless of the payload type:

a. First, it is checked whether at least one of the vertices of the footprint falls within the AOI. If so, the information is stored and the analysis goes on to the next time instant.
b. If the first check is not successful, the possible intersection between the sides of the footprint's polygon and the sides of the AOI polygon is checked. If there is intersection, the related information are stored and the analysis goes on to the next time instant.

4. If one or more AOI observations are identified, the algorithms outputs the initial and final epochs and the entry and exit latitude and longitude coordinates of each passing, thus setting the operativity flag to "observation". Furthermore, if the payload type is optical, the AOI observability conditions are checked and the observability flag is activated.

As in the previous case, the algorithm counts two (or more) observations if the footprint exits and then re-enters the AOI during the same overflight.

### 4.4.1 Performance assessment of the algorithm

In this sub-section, an example of application of the algorithm is shown for both passing and observation cases. The analysis is about a one-day time interval, from midnight of 22$^{nd}$ May 2021 to midnight of 23$^{rd}$ May 2021. The AOI has the following latitude and longitude coordinates:

(-50.5°,100.5°), (-50.5°,155.5°), (-32°,120°), (-15.5°,155.5°), (-15.5°,100.5°).

To generate the ephemerides required by the algorithm, the UNINA propagator has been used. All the available perturbations have been included, selecting the NRLMSISE00 as density model, but limiting to 20x20 the harmonics of the gravity model. The initial orbital parameters of the selected satellite are reported in Table 32.

Table 32 Initial orbital parameters of the satellite considered for the test case

| Parameter | Value |
|---|---|
| Semi-major axis (km) | 7169.17 |
| Eccentricity | 0.0028 |
| Inclination (°) | 98.57 |
| Right ascension of the ascending node (°) | 209.7 |
| Argument of perigee (°) | 95.92 |
| True anomaly (°) | 179.9 |

First, assuming not available payload information, the algorithm checked whether the satellite passes over the AOI in the timespan of interest, following the procedure described in Case A. The analysis showed the presence of 8 overflights, with 2 couples of multiple overflights. The results are summarized in Table 33, and a graphical representation of an overflight is shown in Figure 63, for a double overflight scenario.

Table 33 Results of the analysis for the selected test case, considering payload information not available

| Entry epoch | Entry point | Exit epoch | Exit point |
|---|---|---|---|
| 2021-05-22 01:18:29.000 | (-15.55°,128.1°) | 2021-05-22 01:22:33.000 | (-29.91°,124.5°) |
| 2021-05-22 01:23:39.000 | (-33.77°,123.4°) | 2021-05-22 01:28:26.000 | (-50.45°,117.4°) |
| 2021-05-22 02:59:28.000 | (-15.54°,102.8°) | 2021-05-22 03:02:09.000 | (-25.02°,100.5°) |
| 2021-05-22 12:05:40.000 | (-17.41°,151.4°) | 2021-05-22 12:06:12.000 | (-15.52°,150.9°) |
| 2021-05-22 13:37:13.000 | (-50.48°,136.3°) | 2021-05-22 13:40:46.000 | (-38.13°,131.7°) |
| 2021-05-22 13:43:41.000 | (-27.89°,128.7°) | 2021-05-22 13:47:11.000 | (-15.53°,125.7°) |
| 2021-05-22 15:18:13.000 | (-50.44°,111.1°) | 2021-05-22 15:28:05.000 | (-15.84°,100.5°) |
| 2021-05-22 23:20:31.000 | (-47.86°,150.3°) | 2021-05-22 23:21:16.000 | (-50.45°,149.2°) |

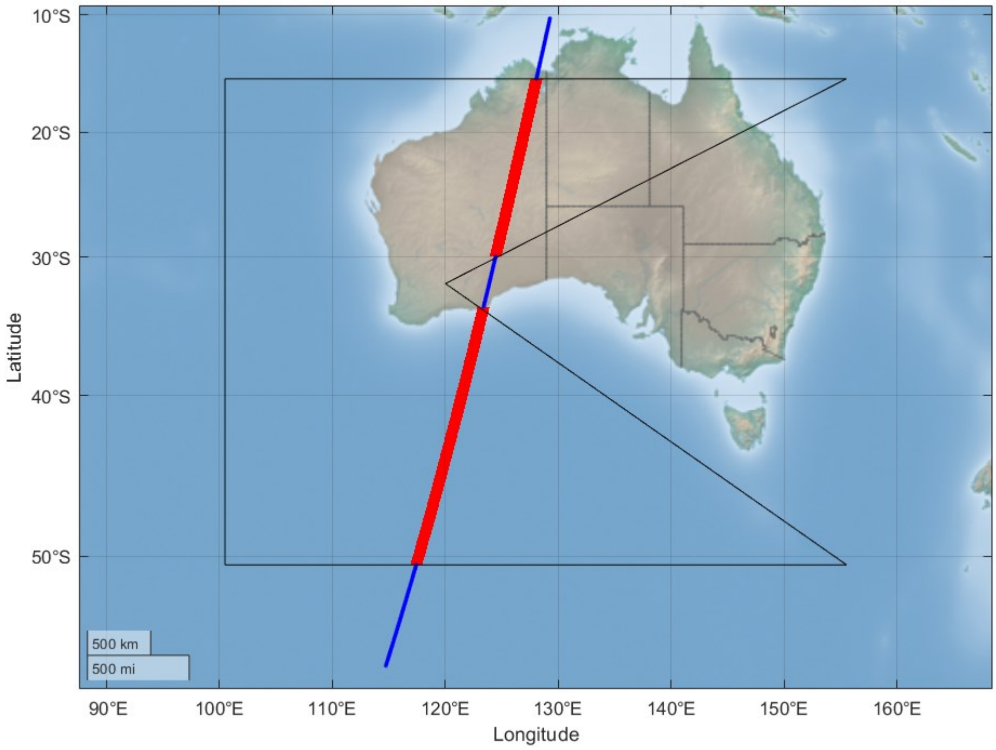


Figure 63 Example of satellite passing over the AOI of interest, when payload information is not available. The red points are those inside the AOI, the blue points are outside.

In the second part of the analysis, payload is considered. In particular, the satellite is assumed to be equipped with a radar sensor, with off-nadir angles of 20° and 50° for near-range and far-range respectively. The results of the analysis are reported in Table 34, and graphical representations of the first observation of Table 34 are shown from Figure 64 to Figure 66, including zooms on entry and exit points.

In general, the results are reasonable in terms of expected revisit time for the considered class of satellites. Thus, the tool can be useful to carry out the coverage analysis of space missions or to support civilian and military SST operations.

Table 34 Results of the analysis for the selected test case, considering payload information available

| Entry epoch | Entry point | Exit epoch | Exit point |
|---|---|---|---|
| 2021-05-22 01:18:32.000 | (-15.54°,125.2°) | 2021-05-22 01:29:42.000 | (-50.49°,100.7°) |
| 2021-05-22 12:05:50.000 | (-16.17°,153.9°) | 2021-05-22 12:06:09.000 | (-15.51°,153.7°) |
| 2021-05-22 13:35:58.000 | (-50.47°,153.1°) | 2021-05-22 13:40:02.000 | (-40.36°,136.1°) |
| 2021-05-22 13:43:51.000 | (-26.61°,131.5°) | 2021-05-22 13:47:08.000 | (-15.52°,128.5°) |
| 2021-05-22 15:16:57.000 | (-50.49°,127.8°) | 2021-05-22 15:28:07.000 | (-15.53°,103.2°) |
| 2021-05-22 16:57:57.000 | (-50.45°,102.5°) | 2021-05-22 16:59:10.000 | (-48.16°,100.5°) |
| 2021-05-22 23:11:24.000 | (-15.51°,155.5°) | 2021-05-22 23:12:58.000 | (-18.72°,148.5°) |
| 2021-05-22 23:19:20.000 | (-41.81°,138.8°) | 2021-05-22 23:22:31.000 | (-50.45°,132.5°) |

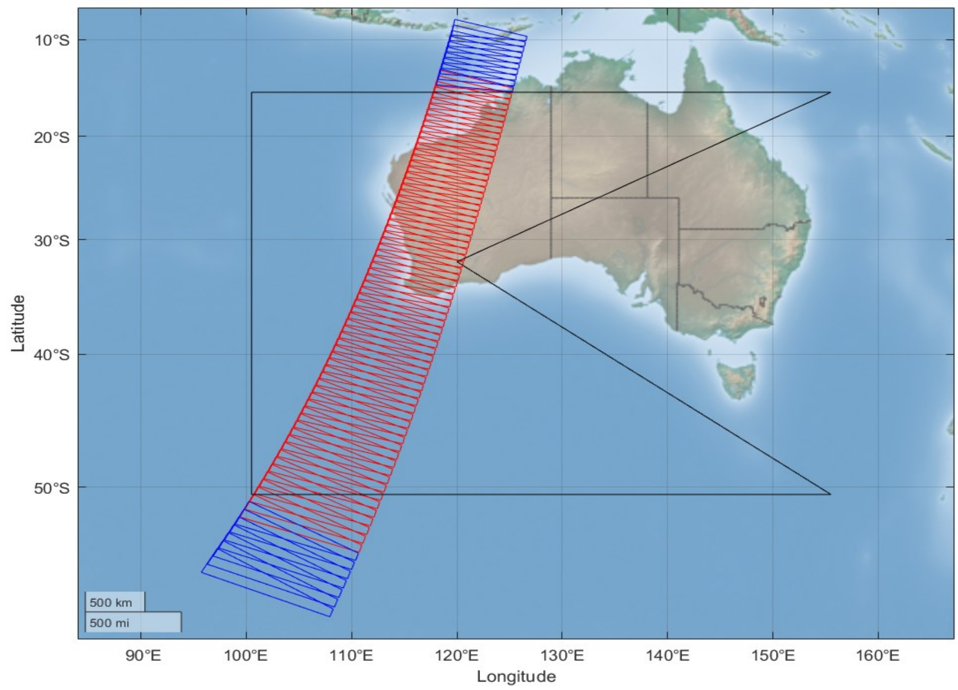


Figure 64 Example of satellite equipped with radar observing the AOI of interest for the first observation of Table 34. The red footprints are those inside the AOI, the blue footprints are outside.

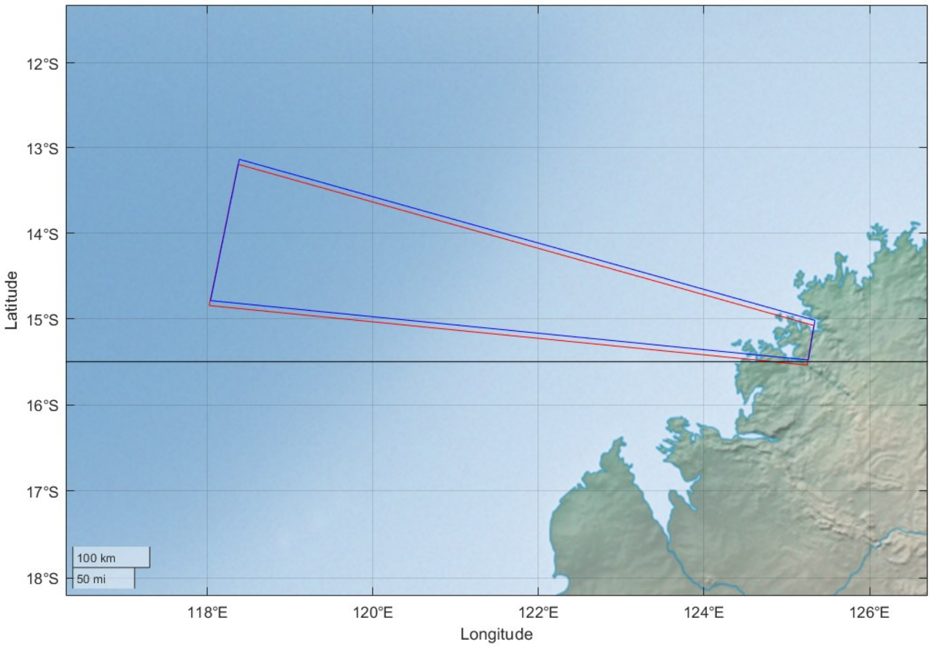


Figure 65 Zoom on the entry point of the first observation of Table 34. The red footprint is inside the AOI, the blue footprint is outside.

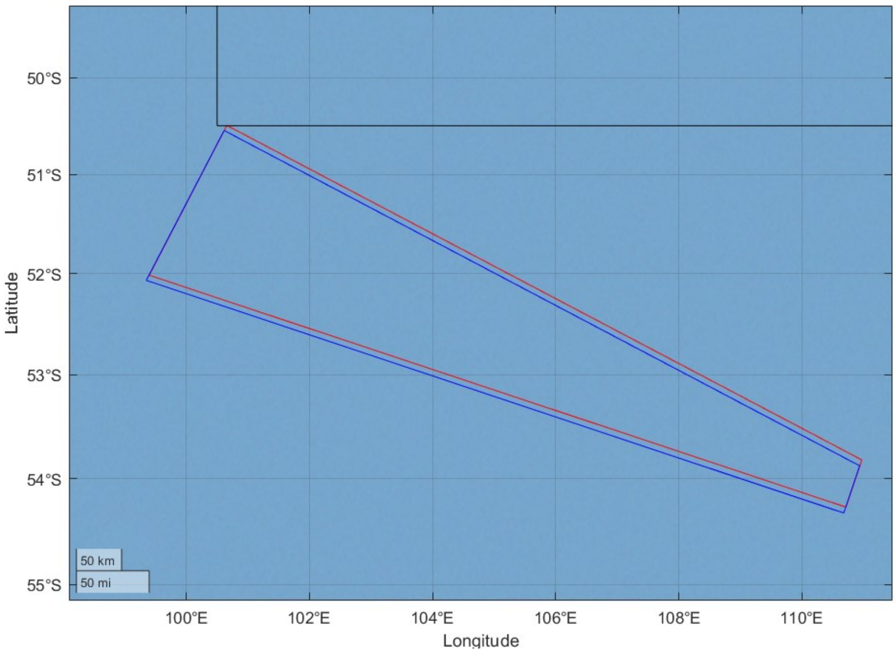


Figure 66 Zoom on the exit point of the first observation of Table 34. The red footprint is inside the AOI, the blue footprint is outside.

# 5. Feasibility study of Mars aerocapture

Aerobraking and aerocapture are the main aeroassisted maneuvers for planetary capture. While the former has been performed several times in previous Mars missions, the latter has never been employed to date. This chapter presents the research activity carried out to investigate the feasibility of aerocapture at Mars for small satellites using a deployable heat shield. First, a brief literature review regarding demonstrations relevant to aerocapture and aerocapture studies is reported, together with the description of the Small Mission to MarS (SMS) project, which has been considered as case study. Then, the modelling and implementation of the aerocapture maneuver is presented, also discussing the Mars atmospheric density modelling. Finally, the description of the general parametric bi-dimensional analysis and the specific three-dimensional Mars mission analysis is provided and results are shown and discussed.

## 5.1 Literature review

According to a recent NASA study [132], aerocapture is ready to be employed for science missions at Venus, Mars, and Titan, and it may enable missions to Uranus and Neptune after further studies and developments. In the case of Mars, a high technological readiness has been reached through many missions performing atmospheric entry. However, despite all its potential benefits, aerocapture has never been implemented because of the uncertainties in Mars' atmospheric density and its variations, as well as navigation errors [19]. Nevertheless, demonstrations relevant to aerocapture have already been accomplished. For instance, in the 1960s, the hypersonic guidance and control necessary for a skip entry into Earth's atmosphere was demonstrated by the Apollo 6 vehicle, and the Soviet Zond spacecraft performed a successful skip entry from lunar return in the same years. In 2014, the Chang'e 5-T1 mission by the Chinese space agency performed a similar aeroassisted manoeuvre. In August 2012, NASA's Mars Science Laboratory (MSL) demonstrated the capability of accurate soft-landing on the Martian surface by using autonomous hypersonic guidance in the atmosphere. Subsequent studies about the relative difficulty of skip entry, hypersonic manoeuvring and aerocapture have led to conclude that both skip entry and hypersonic manoeuvring to precision landing are more challenging than aerocapture because of the tighter tolerances on the vehicle's state [132].

Aerocapture was adopted in the early phases of the design of 2001's Mars Odyssey mission [133], but then replaced with an aerobraking strategy when issues related to the packaging of the aeroshell and the mass budget arose. Since then, the possibility to employ aerocapture for small satellites has been investigated thoroughly. A recent study has demonstrated that aerocapture for SmallSats, i.e., satellites with a mass lower than 180 kg, could increase the delivered mass to Mars, Venus and other destinations [18]. In particular, drag-modulation aerocapture turned out to be an interesting option for SmallSat missions at Mars, since the associated low heat rates allow to use large and lightweight inflatable drag devices [134]. Falcone et al. [17] have shown that single-event drag-modulation aerocapture could be a good way to improve mission flexibility for SmallSat missions at Mars by decreasing the orbit insertion system mass fraction by 30% or more with respect to propulsive options.

### 5.1.1 Review of the SMS mission

SMS was initially conceived as a landing mission. Its development started within ESA's General Support Technology Programme (GSTP). The main objective of SMS was a technology demonstration mission to Mars characterized by small size and low cost. Designed to fit inside a VEGA rocket, it featured an innovative Deployable Heat Shield (DHS) for system deceleration and thermal protection during entry, descent and landing (EDL). Most of the information in this section is extracted from [135], [136].

The SMS spacecraft presents a modular architecture consisting of the capsule, containing the lander module, stowed inside the DHS during launch and interplanetary cruise, the cruise stage (CS) providing power, communications and propulsion support during interplanetary journey, and a kick stage for orbit raising and interplanetary injection (Figure 67, left). The DHS is deployed by an umbrella-like mechanism just before AI (Figure 67, center and right). In this way, the mass/volume ratio at launch increases, widening the choice of possible launchers and, in particular, leading to the possibility of using a small launcher, such as VEGA. The wet system mass is 300 kg, whereas the mass left after jettisoning the CS at Mars approach is 150 kg. In the early SMS design, launch and arrival options were determined in a Sun-spacecraft two-body model following a direct transfer from Earth to Mars. The chosen solution was the minimum-cost option within the 2024 launch window. It is a type II transfer, i.e., the transfer angle is larger than 180°, and corresponds to departing on October 2$^{nd}$ 2024 and arriving on September 1$^{st}$ 2025. This solution has an Earth $C_3$ (launch energy) of 11.316 km$^2$/s$^2$ and a Mars $v_\infty$ of 2.455 km/s. The only deterministic manoeuvre along the trajectory was the targeting manoeuvre at the Mars' Sphere of Influence (SOI) characterized by a magnitude between 33 and 50 m/s.

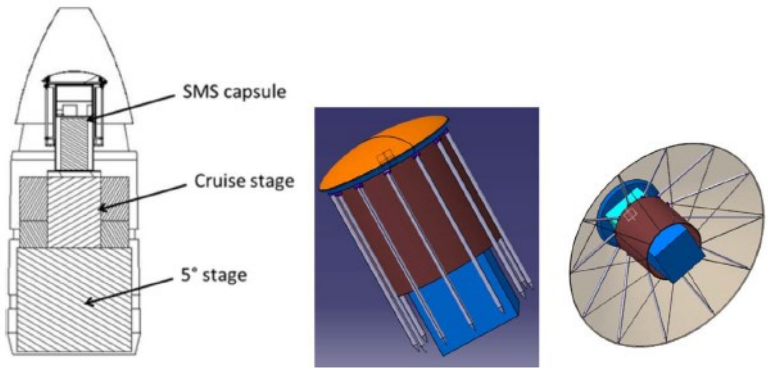


Figure 67 Left: SMS capsule (Lander + DHS), CS and kick stage after assembly and packing in the payload fairing of VEGA. Center and right: the lander inside the DHS in folded and unfolded configuration, respectively.

In the successive phases of the mission development, several innovations have been introduced, including the possibility of using the DHS for Mars orbit insertion through an aerocapture manoeuvre, eventually followed by an aerobraking campaign to lower the eccentricity of the elliptical orbit around Mars. The significant propellant savings resulting from this new development would increase the payload mass fraction and allow to transfer to Mars additional scientific payloads, including CubeSats to be released before atmospheric entry.

The DHS, whose characteristics are described in [135], provides both thermal protection and deceleration through the atmosphere and has been designed on the basis of the Italian ReEntry NacellE (IRENE) capsule concept [137]. IRENE, which can be seen as a first version of the DHS, was conceived for terrestrial applications in the context of research and industrial projects in the field of suborbital re-entry technology [138]. Its demonstrator, Mini-IRENE [139], [140], has been successfully launched on 23rd November 2022.

In all past Mars missions, the design of the entry capsule always included a fixed forebody heat shield, which protected it from the high aerodynamic heating of atmospheric entry. The advantage of using a deployable umbrella-like device is the small attainable ballistic coefficient. The ballistic coefficient achievable by SMS with the DHS can be as small as 20 kg/m$^2$, i.e., less than one third the value for any previous Mars mission [141] (Figure 68 and Table 35), allowing higher decelerations even in the upper region of Mars atmosphere and a substantial reduction of the aerodynamic and aero-thermo-dynamic loads during the hypersonic entry flight path. The umbrella-like concept in the DHS is similar to the ADEPT technology developed by NASA [142], [143].

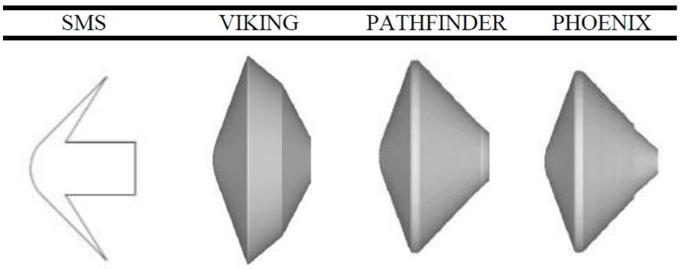


Figure 68 Comparison of the shape of DHS of SMS with previous Mars entry systems.

Table 35 Comparison of the characteristics of DHS of SMS with previous Mars entry systems.

| Parameter | SMS | Viking | Pathfinder | Phoenix |
|---|---|---|---|---|
| Relative entry velocity, km/s | 5.5 | 4.5 | 7.6 | 5.9 |
| Relative entry flight path angle, ° | -13 | -17.6 | -13.8 | -13.2 |
| Ballistic coefficient, kg/m$^2$ | 21 | 64 | 62 | 65 |
| Entry altitude, km | 125 | 82 | 125 | 125 |

## 5.2 Aerocapture modelling and implementation

The analysis focuses on the final phase of an interplanetary trajectory from Earth to Mars modelled with patched conics (Figure 69). For this reason, the simulations here presented start at the surface of Mars' SOI.

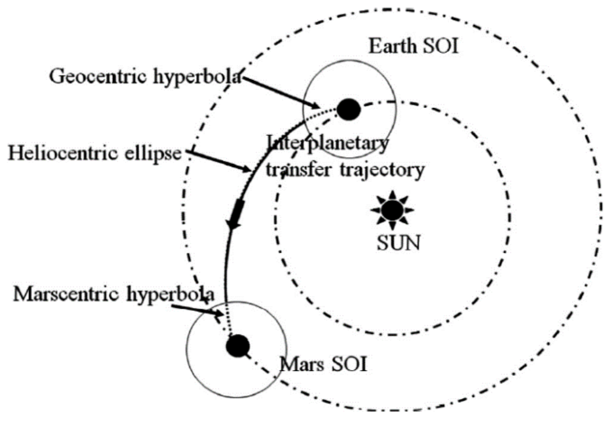


Figure 69 Patched conics approximation for an Earth-to-Mars direct interplanetary transfer [144]

In the patched conics approximation, after entering Mars' SOI, the spacecraft is assumed to be only subject to the gravitational attraction of Mars, i.e., its trajectory is modelled as a gravitational two-body orbit and the solution is a Mars-centric hyperbola. In this work, the arrival hyperbola is propagated up to the atmospheric interface (AI), for which an altitude of 125 km above Mars' surface is assumed (a value of common use in the literature) (Figure 70). Below this limit, the physical model is the drag-perturbed two-body problem,

$$\ddot{\boldsymbol{r}} - \frac{\mu}{r^3}\boldsymbol{r} = \boldsymbol{a_D} \tag{5.1}$$

where $\boldsymbol{r}$ is the position vector of the spacecraft with respect to the center of Mars, $\mu$ is the standard gravitational parameter of Mars and $\boldsymbol{a_D}$ is the acceleration caused by atmospheric drag. The drag perturbation is expressed as follows

$$\boldsymbol{a_D} = -\frac{1}{2}\frac{\rho}{\beta}v\boldsymbol{v} \tag{5.2}$$

$\rho$ being the atmospheric density, a function of altitude, $\beta$ the ballistic coefficient of the probe, $\boldsymbol{v}$ the relative velocity of the spacecraft with respect to the atmosphere and $v$ its magnitude. The ballistic coefficient $\beta$ in classic space exploration applications is defined as

$$\beta = \frac{m}{C_D A} \tag{5.3}$$

where $C_D$ is the drag coefficient, $m$ is the mass and $A$ is the cross section of the spacecraft. The last term can be expressed as $A = A_{max} \cos \theta$, with $A_{max}$ the maximum drag cross-section representing the nominal configuration and $\theta$ the angle of misalignment with respect to such configuration.

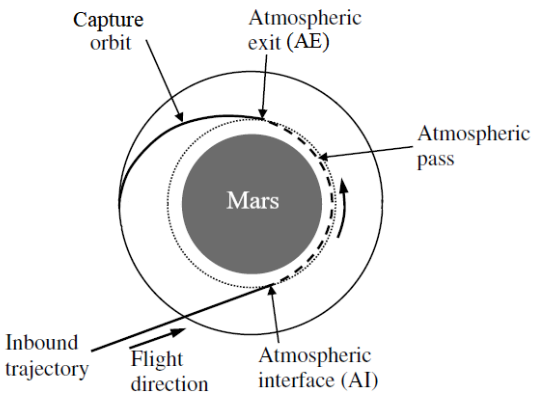


Figure 70 Schematic illustration of the aerocapture maneuver.

Other perturbations act on the trajectory of the spacecraft, such as the inhomogeneous mass distribution within the planet and the gravitational attraction of other bodies in the Solar System. Regarding the former, this study considers the acceleration $a_{J2}$ caused by the second-degree term $J_2$ of the mass distribution of Mars, whereas the third-body perturbation is limited to the contribution $a_{Sun}$ due to the Sun. The expressions for the respective additions to (5.1) are [85]

$$\boldsymbol{a}_{\boldsymbol{J_2}} = -\frac{1}{2}\frac{\mu J_2 R^2}{r^5}[1 - 3\sin^2\varphi]\boldsymbol{r}, \tag{5.4}$$

and

$$\boldsymbol{a}_{\boldsymbol{Sun}} = \mu_{Sun}\left(\frac{\boldsymbol{R}_{\boldsymbol{Sun}} - \boldsymbol{r}}{\|\boldsymbol{R}_{\boldsymbol{Sun}} - \boldsymbol{r}\|^3} - \frac{\boldsymbol{R}_{\boldsymbol{Sun}}}{\|\boldsymbol{R}_{\boldsymbol{Sun}}\|^3}\right). \tag{5.5}$$

Here $R$ is the Mars' radius, $\Phi$ is the geocentric latitude of the spacecraft with respect to Mars, $\mu_{Sun}$ is the standard gravitational parameter of the Sun and $R_{Sun}$ is the position vector of the Sun with respect to Mars' center.

The solutions of (5.1) and those obtained with the addition of the terms given by (5.4) and (5.5) are evaluated numerically by using the explicit Runge-Kutta scheme of 4[th]-5[th] order of the *ode45* solver[8] embedded in MATLAB environment. The use of a

[8] https://it.mathworks.com/help/matlab/ref/ode45.html

higher order scheme, such as the 8th-9th order Runge-Kutta solver presented in Chapter 3, was not required for this application, being its impact on propagation accuracy not significant for typical time intervals of the aerocapture maneuver. The model described by Eq. (5.1) is adopted in the 2D analysis. The extended model, i.e., that including $J_2$ and third-body effects, is used to assess the outcome of the additional perturbations on the trajectories corresponding to the specific mission scenario considered in the 3D study. At atmospheric exit (AE), the orbital parameters are computed to verify if the capture has been achieved, i.e., if the resulting orbit is elliptical.

In the bi-dimensional case, a parametric study is carried out by changing the magnitude $v_\infty$ of the hyperbolic excess velocity $\boldsymbol{v}_\infty$ at Mars arrival and the periapsis altitude $h_\pi$. In this way, a wide range of trajectories can be examined, and general conclusions can be drawn. All the parameters are expressed in the Perifocal Reference Frame centered at Mars (Figure 71): the $\hat{p}$ unit vector points to pericenter, $\hat{w}$ is aligned with the orbital angular momentum and $\hat{q}$ completes the right-handed triad.

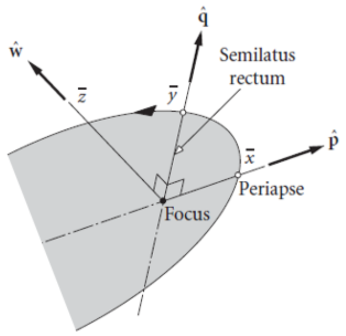


Figure 71 The Perifocal Reference Frame.

The three-dimensional analysis, instead, is carried out for a specific SMS mission scenario. The state vector at Mars' SOI corresponding to an arrival option in September 2025 (and Earth departure 11 months earlier) is used as the initial condition. Since the initial hyperbolic trajectory targets the centre of Mars, an impulsive retargeting manoeuvre is applied at the surface of the SOI. The spacecraft is made to pass through the atmosphere at altitudes that could be suitable for aerocapture while avoiding impact with the surface. All the computations are performed in the Mars

Mean Equator of Date frame based on IAU 2000 Mars Constants (MMEIAU2000) (Figure 72) [145], [146]. The origin of this frame is the centre of Mars and its *xy*-plane is the Mars mean equatorial plane. The *z*-axis is in the direction of the Mars' rotation axis, whose orientation is given as equatorial coordinates in the International Celestial Reference Frame, whereas the *x*-axis is defined by the intersection between Mars' equator and Earth's mean equator of epoch J2000. The *y*-axis completes the right-handed system.

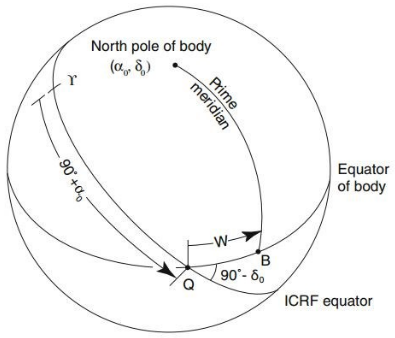


Figure 72 Reference system used to define the orientation of Mars' rotation axis and the MMEIAU2000 frame [146].

### 5.2.1 Mars atmospheric density modelling

Regarding the atmospheric modeling, the density profile chosen for this study is the Mars Global Reference Atmospheric Model (Mars-GRAM) [147], [148], which provides the density for any location (altitude, latitude and longitude) and time (down to daily variations). It is an engineering-oriented empirical model of the Mars atmosphere and it was built with the parametrization of the data collected by Mariner and Viking and the results of NASA Ames Mars General Circulation Model (MGCM) for altitudes between 0 and 80 km, and the University of Arizona Mars Thermospheric General Circulation Model (MTGCM) above 80 km [149], [150]. Mars-GRAM computes atmospheric parameters (temperature, pressure, density), surface physical data, electromagnetic fluxes, atmospheric heating rates, as well as thermodynamic properties of CO2. The 2001 version of Mars-GRAM is the core component of the

Mars Environment Multi-Model (MEMM) [151], an engineering tool developed at the Polytechnic University of Catalonia, which merges existing models of the Mars environment. MEMM outputs the several atmospheric parameters in a unified way.

The adoption of Mars-GRAM follows a detailed comparison with other state-of-the-art density models based on atmospheric data obtained from previous Mars missions. In order to compare the various models and evaluate the capability of Mars-GRAM to simulate all the possible atmospheric conditions, two density profiles have been extracted from MEMM, respectively representing a very high density and a very low density case and corresponding to one hot and one cold case scenario under clear sky conditions, i.e., away of dust storms. The hot case is a summer (Solar Longitude Ls = 270°) midday profile under high solar activity (Solar F10.7 Flux = 300 SFU). The cold case, instead, is a winter (Ls = 90°) nighttime profile at low solar activity (Solar F10.7 Flux = 60 SFU).

A brief review of the models considered in the comparison (Figure 73 Figure 74) is given below. First of all, we have considered the atmospheric density data collected in 1976 by the Viking 1 lander during its atmospheric descent and the profile based on the relevant observations collected continuously between 150 and 10 km of altitude by the Mars Pathfinder lander in 1997 [152]. Then, the density profile provided by COSPAR Mars Reference Atmosphere, as reported in [153], has been considered. ESA's 2003 Mars Express orbiter observed 616 stellar occultations, deducing the amount of CO2, the main constituent of the Martian atmosphere, between the instrument and the star, with its ultraviolet spectrometer SPICAM from January 14, 2004 (Mars Solar Longitude, Ls = 332.8°) to April 11, 2006 (Ls = 37.6°) [154]. In [154], Forget et al. report three density profiles corresponding to different epochs and positions, but only the most extreme profile has been used for the comparison.

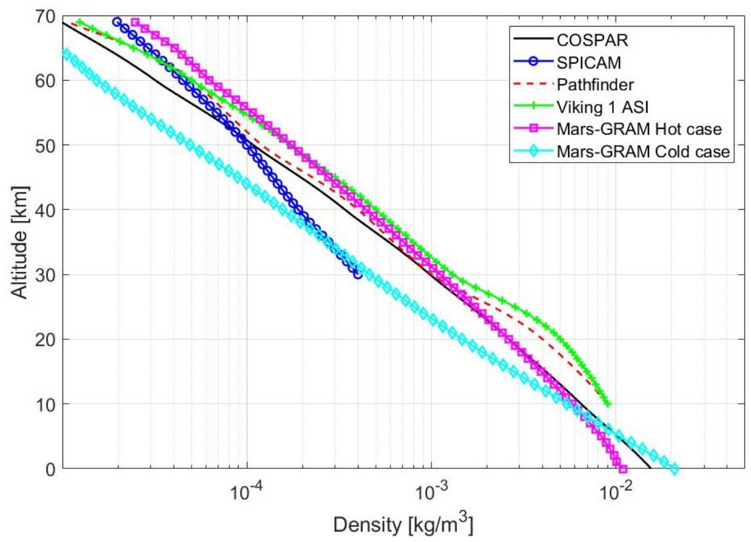


Figure 73 Comparison between Mars atmospheric density profiles as predicted by various models for the altitude range 0 to 70 km. The dashed black line at 125 km indicates the assumed upper limit of the atmosphere.

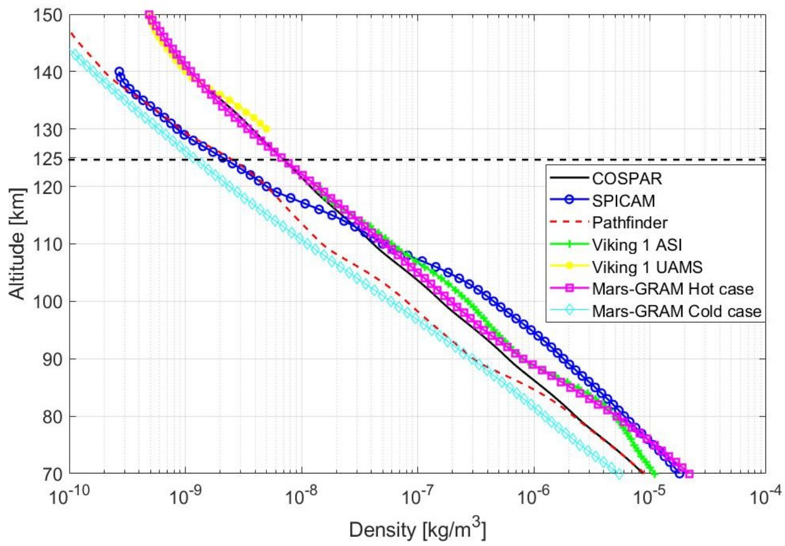


Figure 74 Comparison between Mars atmospheric density profiles as predicted by various models for the altitude range 70 to 150 km. The dashed black line at 125 km indicates the assumed upper limit of the atmosphere

The densities predicted by the several models allow to define a range of values at each altitude. According to Figure 73 and Figure 74, the cold case Mars-GRAM density is always the lowest and for this reason here it has been adopted as the lower bound of the density ranges for all the altitudes of interest. The hot case Mars-GRAM density is not always the highest, instead. First of all, there are altitudes at which the Viking density is higher than the Mars-GRAM hot case, but the differences are small, and Mars-GRAM includes Viking observations as well. There is also a window of altitudes, between 75 and 110 km, in which the SPICAM density profile overtakes the hot case Mars-GRAM profile. A possible explanation for this phenomenon is the variation of the dust content of the lower atmosphere, which causes most of the density seasonal variations. Indeed, other profiles from SPICAM obtained for different Solar Longitudes show lower density values and never exceed Mars-GRAM's hot case [154]. For these reasons and for the sake of simplicity, Mars-GRAM has been adopted also to represent the upper bound of the density range.

## 5.3 Application to Mars scenarios

### 5.3.1 Parametric 2D analysis

The parametric analysis is realized by varying the magnitude $v_\infty$ of the hyperbolic excess velocity $\boldsymbol{v}_\infty$ and the periapsis altitude $h_\pi$. These two quantities uniquely define the shape of the arrival hyperbola. Due to the symmetry of the problem, the study is limited to zero-inclination Mars arrival hyperbolic orbits (i.e., in Mars equatorial plane). The parameters used in these simulations are those of the SMS capsule. In particular the ballistic coefficient $\beta$ is set at 21.23 kg/m$^2$ and $C_D$ = 1 [155]. The parametric analysis is performed for the $v_\infty$ and $h_\pi$ ranges of Table 36 and using the nominal Mars-GRAM atmospheric density profile extracted from MEMM. Then, the uncertainties in the atmospheric density and ballistic coefficient are shown (Table 37). We simulate the density uncertainty by increasing and decreasing the density values by a percentage amount. The Mars-GRAM density profile extracted from MEMM and the density profiles obtained considering uncertainties up to 70% of the nominal value are shown in Figure 75. The uncertainty of 6.38 kg/m$^2$ in the ballistic coefficient reported in Table 37 is representative of variations of about 30% in the aerodynamic drag coefficient and about 10° in $\theta$, including attitude control errors and errors in the shield opening mechanism.

Table 36 $v_\infty$ and $h_\pi$ ranges and resolutions used in the 2D parametric analysis

| Parameter | Range | Increment |
|---|---|---|
| Hyperbolic excess velocity, $v_\infty$, km/s | 2 to 4 | 0.1 |
| Periapsis altitude, $h_\pi$, km | 50 to 110 | 0.1 |

Table 37 Uncertainties in the atmospheric density and ballistic coefficient

| Parameter | Uncertainty |
|---|---|
| Atmospheric density | ±35%, ±50% and ±70% with respect to the nominal density profile |
| Ballistic coefficient, kg/m$^2$ | ±6.38 |

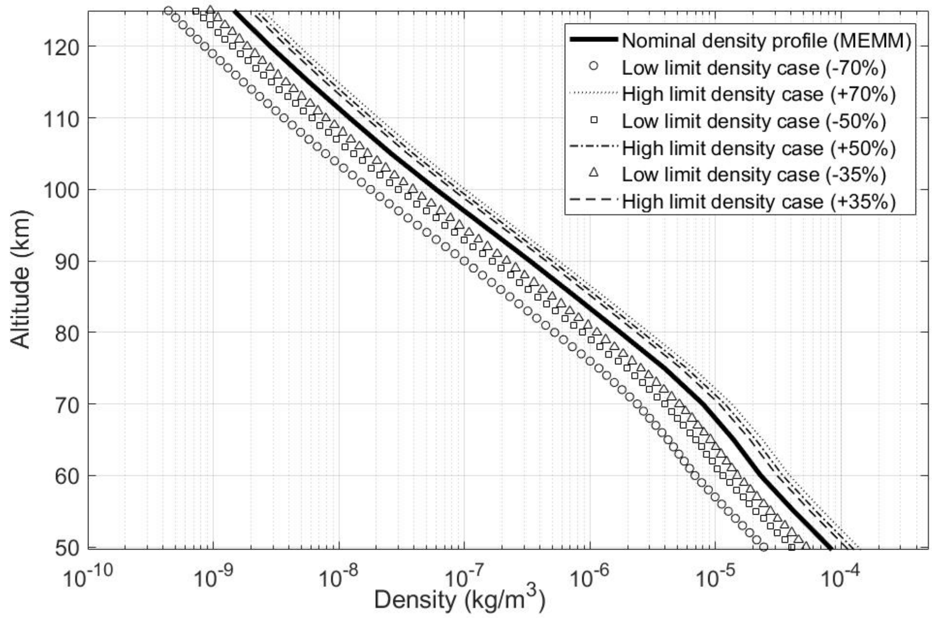


Figure 75 Atmospheric density profiles for the range of altitudes of interest in this study

Each $v_\infty$-$h_\pi$ pair in the selected ranges corresponds to a different hyperbolic arrival trajectory. A first simulation was carried out for nominal atmospheric conditions, i.e., without any uncertainty, and the results show a range of periapsis altitudes producing aerocapture for each arrival velocity in the given interval (Figure 76). It can be noted that as $v_\infty$ increases, the intervals of useful $h_\pi$ shrink and the centers of the intervals move towards lower altitudes. The periapsis altitudes reported in Figure 76 are those of the ideal Keplerian trajectories, whereas the actual periapsis altitudes are slightly lower. The gap between the Keplerian and the real $h_\pi$ varies from more than 0.6 km for altitudes around 75 km to a few tens of meters for altitudes around 95 km.

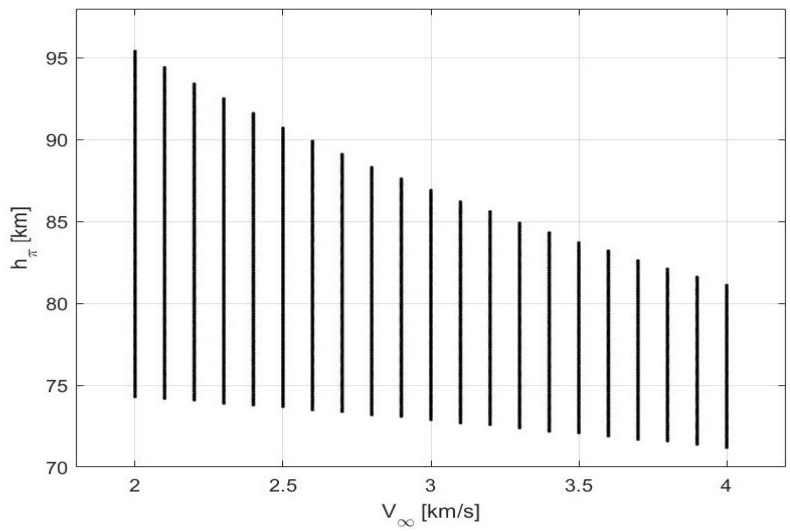


Figure 76 Map of v∞-hπ pairs leading to aerocapture in the nominal scenario.

Figure 77 illustrates the results obtained by considering different levels of atmospheric density uncertainty and keeping the ballistic coefficient at its nominal value. For each uncertainty range, only the two extreme density conditions (vertex analysis) are simulated and only the common solutions are included. The number of successful pairs decreases with increasing level of uncertainty. For uncertainty values higher than 35% there are arrival velocity intervals which do not lead to capture. However, we note that even with 70% atmospheric density uncertainty it is still possible to find viable solutions for aerocapture when the arrival velocity is between 2 and 2.5 km/s and the periapsis is above 80 km altitude.

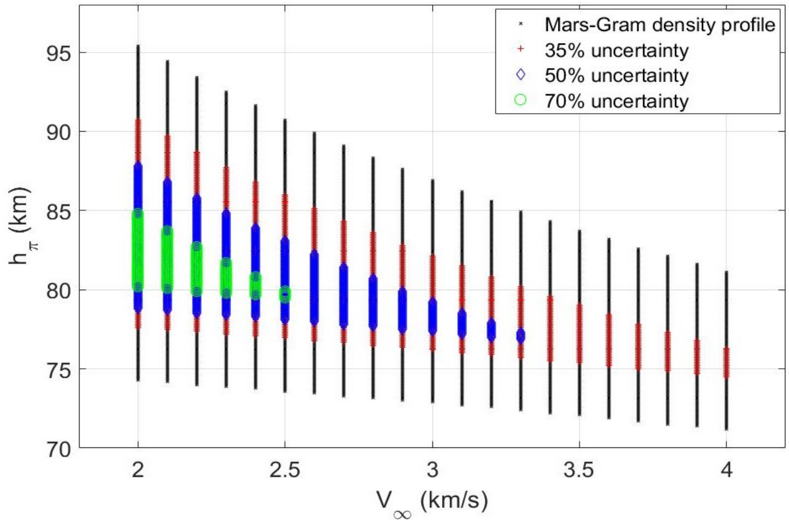


Figure 77 Map of $v_\infty$-$h_\pi$ pairs leading to aerocapture for the nominal scenario and its modification with increasing atmospheric density uncertainty.

Figure 78 shows the effect of the ballistic coefficient uncertainty on the solutions computed with the nominal atmospheric density profile. Also here only common solutions are considered. It can be noticed that, in general, the periapsis altitude range leading to aerocapture is reduced, but an interval for this parameter can still be found for each arrival velocity.

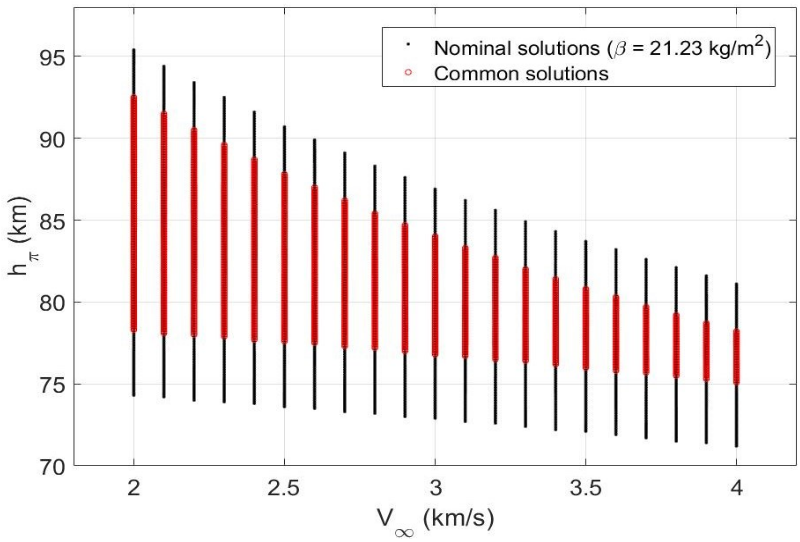


Figure 78 Map of $v_\infty$-$h_\pi$ pairs leading to aerocapture for the nominal scenario and its modification when the uncertainty in the ballistic coefficient is introduced.

Finally, we analyse the simultaneous effect of ballistic coefficient and atmospheric density uncertainties. In this case, aerocapture is achieved only for atmospheric uncertainties within ±35% (Figure 79), but they are limited to Mars arrival velocities up to 2.8 km/s and periapsis altitudes higher than 80 km. It can be noticed the significant narrowing of the altitude ranges producing aerocapture.

In summary, we have found combinations of parameters which guarantee the success of the aerocapture manoeuvre regardless of the uncertainties, when these are within particular ranges, and this represents a general result for the bi-dimensional analysis.

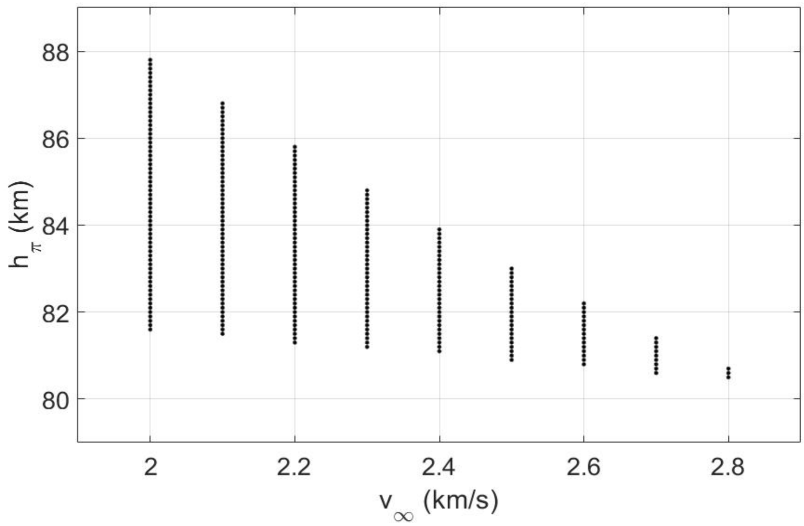


Figure 79 Map of $v_\infty$-$h_\pi$ pairs that lead to captured orbits when both the ballistic coefficient uncertainty and a 35% uncertainty in the atmospheric density are included.

### 5.3.2 Three-dimensional analysis

The initial conditions for the study are the orbital parameters of the spacecraft when it enters the SOI according to the nominal SMS mission [135] (Table 38). They correspond to a $v_\infty$ of 2.455 km/s.

Table 38 Orbital parameters of the hyperbolic trajectory at Mars' SOI

| Parameter | Value |
|---|---|
| UTC Epoch | 29/8/2025 06:42:11 |
| Semi-major axis (km) | -7287.768 |
| Eccentricity | 1.0000274 |
| Inclination (°) | 98.8 |
| Right ascension of the ascending node (°) | 122.5 |
| Argument of perigee (°) | 263.7 |
| True anomaly (°) | 180.4 |

The analysis consists in applying a velocity variation at the SOI of Mars targeting an atmospheric passage at altitudes suitable for aerocapture, in agreement with the 2D parametric analysis. A loop is considered on the three parameters characterizing the manoeuvre, i.e., its magnitude $\Delta V$ and its orientation as expressed by two angles, $\lambda$ and $\delta$ (Table 39), respectively representing longitude and latitude in a reference frame with origin at the spacecraft centre of mass and parallel to MMEIAU2000. The range of variation of $\Delta V$ is consistent with the magnitude of the nominal targeting manoeuvre of SMS and with the propulsive limitations of a platform of its category.

Table 39 Parameters of the targeting manoeuvre

| Parameter | Range | Increment |
|---|---|---|
| Magnitude, $\Delta V$, m/s | 30 to 40 | 0.1 |
| Longitude, $\lambda$, (°) | 0 to 360 | 1 |
| Latitude, $\delta$, (°) | -90 to 90 | 1 |

The values reported in Table 39 are intended for a first-look analysis. In a second phase, ΔV is kept constant and equal to the value that provides continuity in the two angles when these are varied over ranges of interest at increments of 0.1°. Since this value is representative of the angular accuracy attainable in the execution of the manoeuvre, checking the continuity against these smaller angular increments is crucial to ensure the success of the aerocapture even in presence of manoeuvring errors.

The analysis starts from the same nominal atmospheric density profile and ballistic coefficient and the same uncertainties as in Table 37. Applying the manoeuvres of Table 39 to the nominal conditions yields the 3D map of successful captures displayed in Figure 80. It can be noted that aerocapture is successful only when the magnitude of the impulse is 33.4 m/s or larger. Solutions become more and more scattered as ΔV increases. Thus, the manoeuvres with ΔV of 33.4 m/s are the most interesting because they give rise to successful captures over continuous ranges of the two angles. The 2D map of the successful manoeuvres for the selected ΔV is shown in Figure 81.

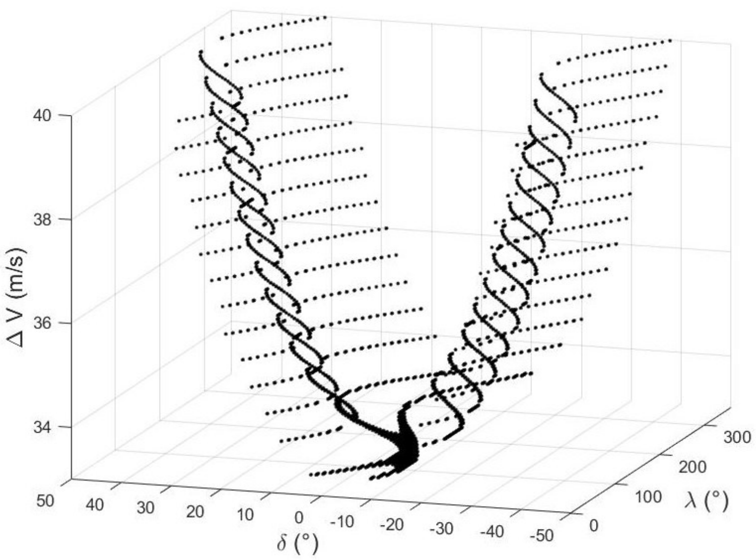


Figure 80 3D map of the manoeuvres leading to aerocapture when considering the ranges and the increments of the maneuver's parameters reported in Table 39.

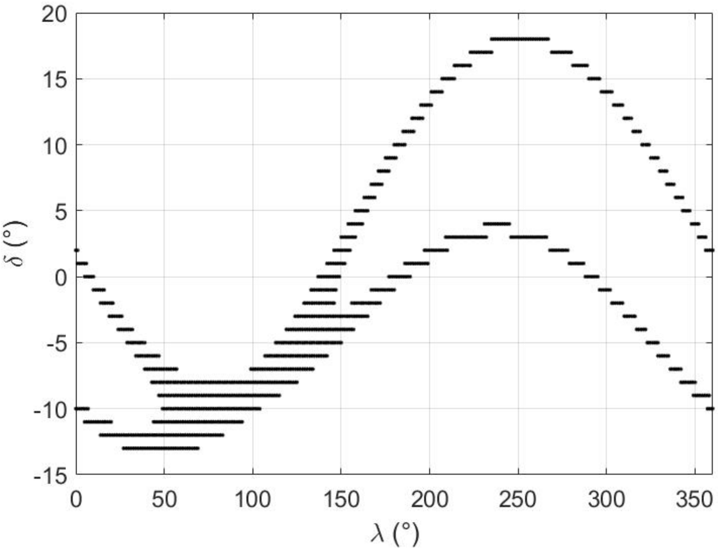


Figure 81 2D map of the successful orientations of the targeting manoeuvre when the impulse has a magnitude ΔV of 33.4 m/s.

The solutions are scattered everywhere except in the region corresponding to the range 20° to 180° in λ and -15° to 0° in δ. In this subset, the continuity is checked against smaller variations in both angles by applying a discretization of 0.1°, representative of the angular accuracy of the manoeuvre. Figure 82 shows that the continuity of the successful manoeuvre orientations persists at this higher angular resolution.

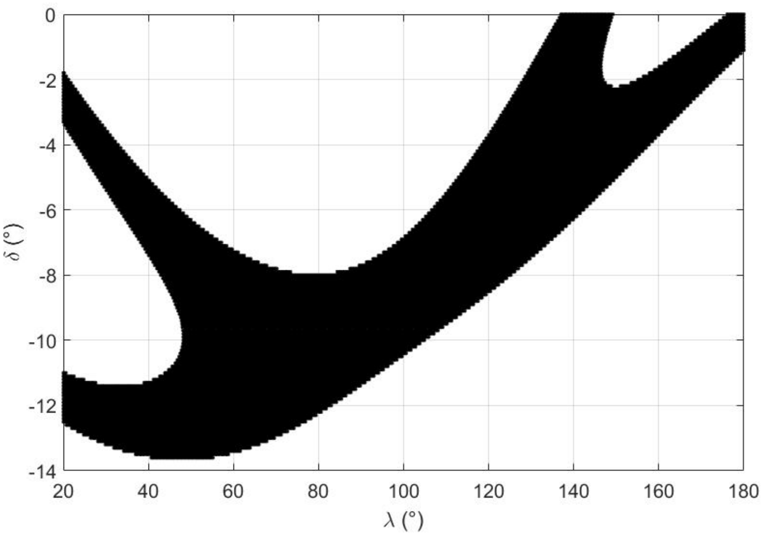


Figure 82 2D map of the successful orientations of the targeting manoeuvre when the impulse has a magnitude ΔV of 33.4 m/s and the angular resolution is 0.1°.

Figure 83 illustrates the periapsis altitudes $h_\pi$, i.e., the minimum altitudes reached in atmosphere, of the hyperbolic trajectories obtained after application of the velocity variation at Mars' SOI for the ranges of the parameters that ensure continuity in the higher angular resolution exploration. The outcome is in good agreement with the results obtained in the 2D analysis for the same nominal scenario (Figure 76).

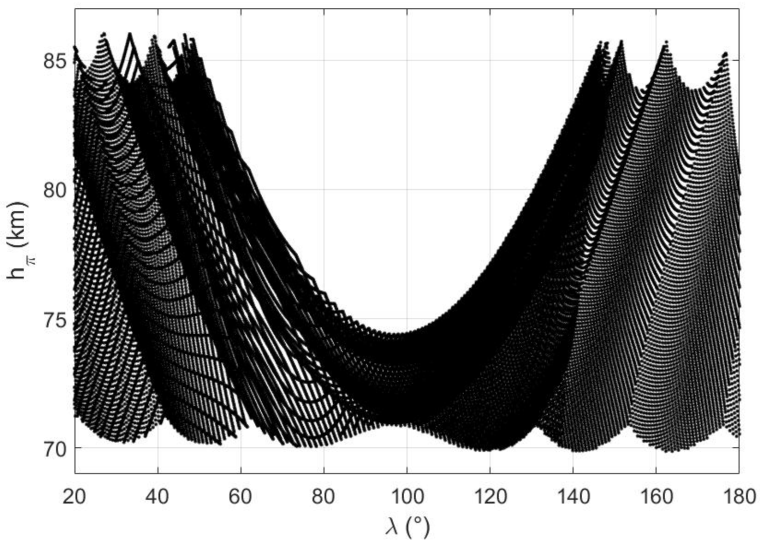


Figure 83 Map of periapsis altitudes hπ of the hyperbolic trajectories suitable for aerocapture after the application of the manoeuvre at Mars' SOI.

Then, keeping fixed the ballistic coefficient at the nominal value, the influence of the different levels of atmospheric density uncertainty on the distribution of solutions in the λ-δ map of Figure 82 has been investigated. Like for the parametric analysis, for each uncertainty level, we accept only the solutions in common to the two vertex density conditions. The results are shown in Figure 84. The ±70% uncertainty case gives no solutions. The reason is that at -70% uncertainty, the atmosphere is very thin and does not cause a sufficient deceleration. Also, in the 2D analysis the number of solutions obtained for this level of uncertainty is small (see Figure 77). Figure 84 has been obtained with increasing atmospheric density uncertainty (nominal, 35% and 50%): the number of successful combinations of parameters decreases as indicated by the shrinking of the corresponding areas in the map. The initial continuity is lost.

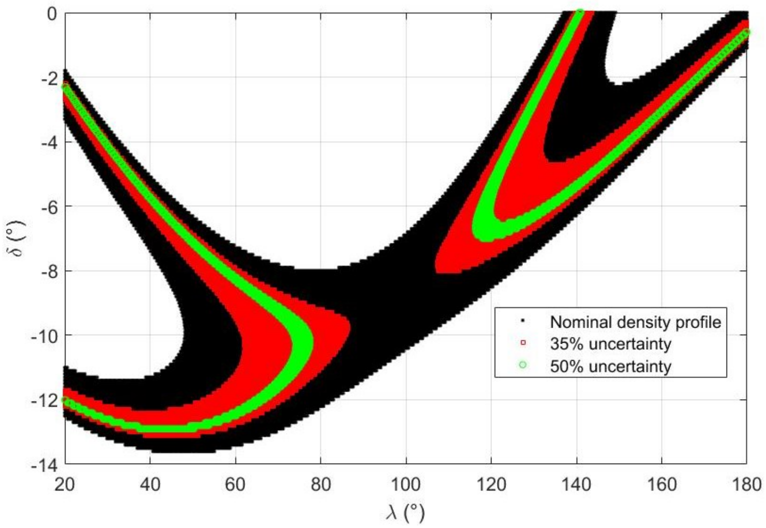


Figure 84 2D map of the successful orientations of the targeting manoeuvre with increasing atmospheric density uncertainty (nominal, 35% and 50%).

Since at uncertainties of -50% and -70% the number of successful parameter combinations is very low, we have limited the analysis to uncertainties between -35% and +70%. The corresponding map is displayed in Figure 85. The simulations carried out for the two extreme density cases in this uncertainty interval lead to very different elliptical orbits in terms of eccentricity $e$ and apocenter altitudes $h_\alpha$ , as shown in Figure 86Figure 87. When assuming +70% of density uncertainty, the resulting orbits have $e$ lower than 0.3 and $h_\alpha$ limited to 2500 km, while, for the -35% density uncertainty case, the eccentricities are higher than 0.9.

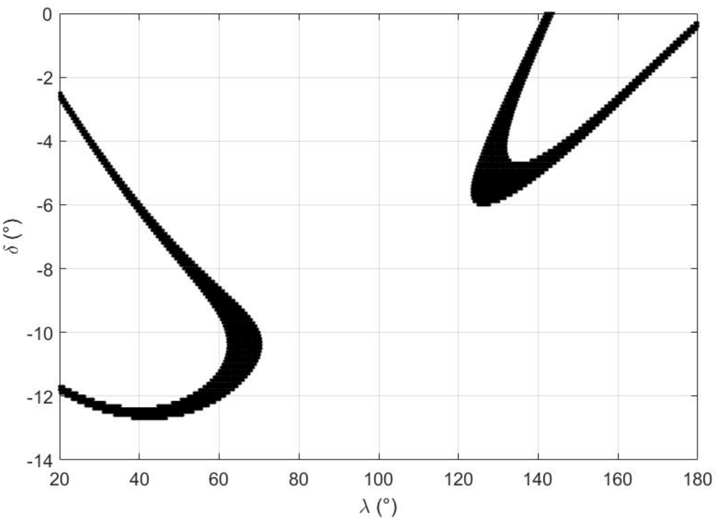


Figure 85 2D map of the successful orientations of the targeting manoeuvre for atmospheric density uncertainties between -35% and +70%.

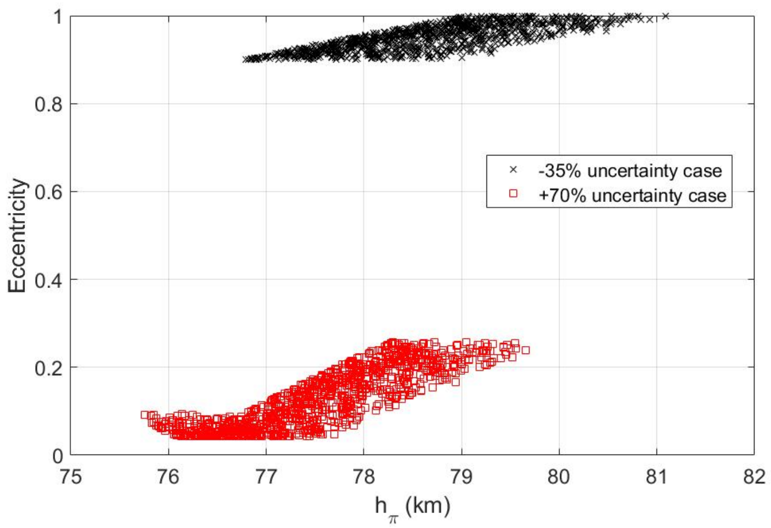


Figure 86 Eccentricities of the captured orbits at -35% (black crosses) and +70% (red squares) density uncertainty, respectively, versus the minimum heights reached in the atmosphere.

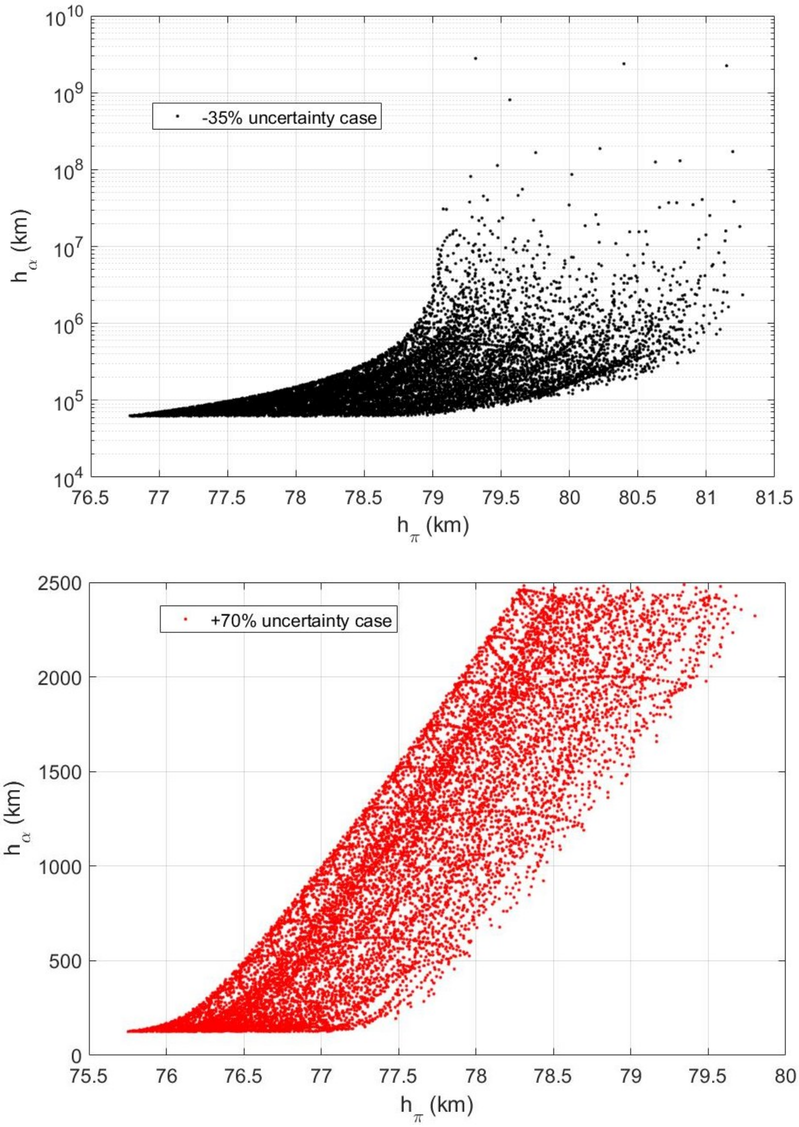


Figure 87 Apocenter altitudes of the captured orbits at -35% and +70% density uncertainty, respectively in the top and bottom plots, versus the minimum heights reached in the atmosphere.

Finally, Figure 88 illustrates the effect of the uncertainty in the ballistic coefficient. When the ballistic coefficient is lower or higher than the nominal value, the areas of successful parameter combinations become wider and tend to shift slightly. This is very interesting since a changing ballistic coefficient can be achieved by increasing or reducing the drag cross section through in-flight modulation of the aperture of the DHS.

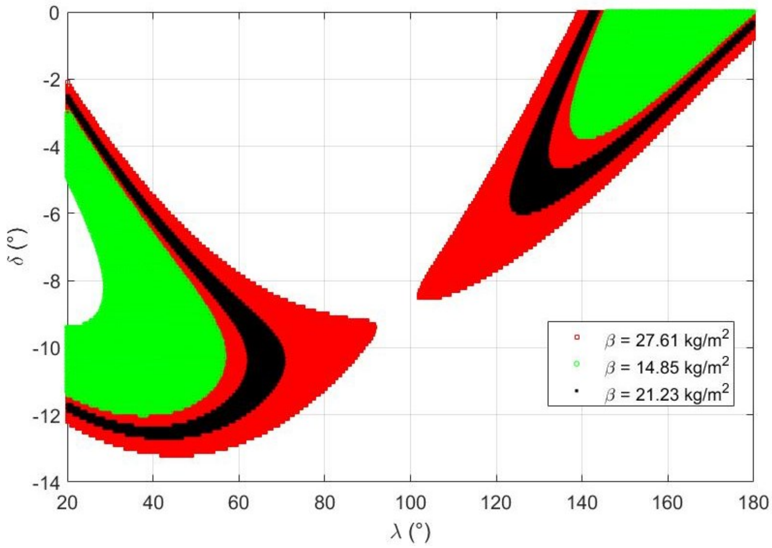


Figure 88 Effect of the ballistic coefficient uncertainty on the combinations of angles that correspond to captured orbits for density uncertainties between -35% and +70%.

For the sake of completeness, an example of circularization manoeuvre is presented in the following to derive the order of magnitude of the ΔV budget of the entire mission for a case of possible scientific interest. Considering the nominal scenario, applying for instance the manoeuvre characterized by λ = 100° and δ = -10.2°, the spacecraft exits the atmosphere in an orbit with $h_\alpha$ of 692.8 km and $e$ of 0.0871. The periapsis raising manoeuvre needed to circularize this orbit has a size of 144.2 m/s, which brings the total ΔV budget to 177.6 m/s.

# 6. Conclusions and future developments

This thesis presented the research activity aimed at the development and the performance assessments of advanced astrodynamics techniques and tools to be applied in Space Surveillance and Tracking and Space Exploration contexts.

Space Surveillance and Tracking applications

In the context of SST and SSA, a numerical orbit propagation environment has been developed, as a useful tool to deal with SST applications in general, and its implementation has been discussed. An accuracy-computational cost trade-off study has been carried out, to identify adaptability criteria as a first step towards the integration of such propagation environment in a modular architecture, capable to take both the requirements of specific SST tasks and the involved propagation uncertainties into account. The study has supported the definition of adaptability criteria, suggesting that, for low LEO propagations, it is advisable to consider a reduced number of gravity field harmonics and to remove third-body and SRP perturbations, as long as position errors up to 1 km for a 7-days propagation can be accepted. Indeed, this configuration allows to save around 30% of computational time and it is particularly convenient when dealing with a large number of objects, i.e., propagation of fragments coming from a fragmentation event.

Exploiting the modularity of the propagation environment, various applications have been addressed, tailoring the propagation settings on the different requirements of the specific SST task. The main contribution has concerned the development of a method, called Uncertainty-aware Cube method, for the evaluation of the medium-term collision frequency for space objects in LEO. It is a new version of the non-covariance-based Cube method, modified to take the objects' position errors generated by propagation-related uncertainties in the conjunction detection process into account, thus representing a hybrid between the covariance-based and non-covariance-based methods. The global aim was to provide realistic pictures of the potential conjunctions occurring in the near future, to support sensor tasking operations and to identify the most endangered assets in medium-term scenarios. The Uncertainty-aware Cube method resulted to be capable to detect the conjunctions even in presence of significant *A/M* uncertainties, provided that these are consistent with the position errors computed through the uncertainty evaluation process. The proposed method proved to be suitable for the medium-term screening task, being capable to reduce the missed detection rate by accounting for propagation uncertainties. Clearly, this approach usually causes an increase in the false alarm rate, which would represent a problem for collision avoidance application, but results to be less critical for screening operations. From a computational point of view, with respect to standard Cube implementation, the Uncertainty-aware approach requires a larger computational effort, which depends on the cube size and the magnitude of the uncertainties involved and increases when reducing the cube size and when considering lower altitudes, as the uncertainty magnitude increases.

With regards to the uncertainty evaluation process required by the Uncertainty-aware Cube, an analytical method has been developed to estimate the position errors coming from uncertainties in medium-term LEO propagations. The proposed method is based on the DOPs formulation of the Hill's equations. Since the drag perturbation is dominant in LEO, the uncertainty in its input parameters is modeled as a sort of differential drag, which causes an accumulation of both the semi-major axis error and the along-track position error. The proposed method, taking as input the state vectors coming from propagation with a standard value of the $K$ parameter and a percentage of $K$ uncertainty, provides in output the time evolutions of the predicted along-track and semi-major axis errors. The results suggest that the prediction performance of the method clearly improves for increasing orbit altitude, being also less significant the effect of the differential drag perturbation. Therefore, while the method always shows very good accuracy for altitudes higher than 600 km, at lower altitudes its usage should be limited to less than 30 days when the involved uncertainty is equal or higher than 100%. However, in these cases, the method always overestimates the error due to the input uncertainty. This behavior is convenient if the tool is applied together with the Uncertainty-aware Cube or, in general, in an operative context in which the collision frequency of assets of interest must be foreseen. A conservative estimation of the errors can be useful in such context not to lose information about potential risk, even if it could imply an increase of the computational time. Future developments of this method could include a more specific modelling of the uncertainties, in particular those related to the bad forecast of the EUV and geomagnetic indices, as well as accounting for the effects of differential SRP at higher LEO altitudes, to improve the global performance of the method and its range of applicability.

The thesis also presented a sensor calibration tool to perform the metrological characterization of ground-based sensors to support SST applications and sensor tasking services. The tool implemented an iterative method for the computation of the sensor time bias, based on the minimization of the along-track error and it is capable to evaluate the residuals for all the metric observations. The performance assessment has shown results that are consistent with the values expected for a calibration of a SST radar and in the same order of magnitude of the residuals admissible to accept tracklets during a correlation process.

Finally, an algorithm for the evaluation of satellite coverage over area of interest has been developed and tested generating the required ephemerides using the developed propagator, to support RSP applications.

<u>Feasibility study of Mars aerocapture</u>

A modified and simplified version of the numerical propagator has been developed for Mars environment and, in particular, to deal with the aerocapture problem. In this context, a simulation environment has been developed to assess the feasibility of aerocapture at Mars for small satellites using a deployable drag device, whose aperture can be modulated in flight. The study focused on the impact that atmospheric density and ballistic coefficient uncertainties have on the success of the aerocapture maneuver and it has involved two type of analysis: first a parametric bi-dimensional study, useful to draw general considerations about aerocapture feasibility and to design possible aerocapture "corridors", in terms of hyperbolic arrival velocity and pericenter altitude; then, a three-dimensional analysis for a specific Mars mission scenario, aimed at identifying the most suitable targeting maneuvers leading to successful aerocapture.

The analyses show the strong influence of the uncertainties related to atmospheric density and ballistic coefficient, which significantly narrow the solution space.

However, viable solutions for aerocapture were identified even in the worst uncertainty scenarios, thus proving the deployable drag device to be suitable to perform aerocapture successfully.

Improvements to the current model can include the possibility to implement drag-modulation strategies, by modulating the aperture of the shield during the atmospheric pass, in order to widen the aerocapture "corridors" and increase the number of successful maneuver leading to aerocapture.

# Bibliography


[1] “ESA - Space debris by the numbers.” https://www.esa.int/Space_Safety/Space_Debris/Space_debris_by_the_numbers (accessed Jul. 25, 2022).

[2] D. L. Oltrogge and S. Alfano, “The technical challenges of better Space Situational Awareness and Space Traffic Management,” *Journal of Space Safety Engineering*, vol. 6, no. 2, pp. 72–79, 2019, doi: https://doi.org/10.1016/j.jsse.2019.05.004.

[3] T. Donath, T. Schildknecht, V. Martinot, and L. Del Monte, “Possible European systems for space situational awareness,” *Acta Astronaut*, vol. 66, no. 9–10, pp. 1378–1387, 2010, doi: 10.1016/j.actaastro.2009.10.036.

[4] UNOOSA, “Space Debris Mitigation Guidelines of the Committee on the Peaceful Uses of Outer Space,” *United Nations*, 2010.

[5] J. A. Kennewell and B. N. Vo, “An overview of space situational awareness,” in *Proceedings of the 16th International Conference on Information Fusion, FUSION 2013*, 2013, pp. 1029–1036.

[6] H. Klinkrad, *Space debris : models and risk analysis*, 1st ed. Springer, 2006. doi: 10.1007/3-540-37674-7.

[7] D. J. Kessler, “Derivation of the collision probability between orbiting objects: the lifetimes of jupiter’s outer moons,” *Icarus*, vol. 48, no. 1, pp. 39–48, Oct. 1981, doi: 10.1016/0019-1035(81)90151-2.

[8] J. C. Liou, “Collision activities in the future orbital debris environment,” *Advances in Space Research*, vol. 38, no. 9, pp. 2102–2106, Jan. 2006, doi: 10.1016/J.ASR.2005.06.021.

[9] D. Vaughan, H. Miller, B. Griffin, B. James, and M. Munk, “A Comparative Study of Aerocapture Missions with a Mars Destination,” *41st*

*AIAA/ASME/SAE/ASEE Joint Propulsion Conference & Exhibit*, 2005, doi: 10.2514/6.2005-4110.

[10] H. S. Wright *et al.*, "Mars Aerocapture Systems Study," no. NASA/TM-2006-214522, 2006.

[11] R. R. Rohrschneider and R. D. Braun, "Survey of ballute technology for aerocapture," *J Spacecr Rockets*, vol. 44, no. 1, pp. 10–23, 2007, doi: 10.2514/1.19288.

[12] G. D. Walberg, "A survey of aeroassisted orbit transfer," *J Spacecr Rockets*, vol. 22, no. 1, pp. 3–18, 1985, doi: 10.2514/3.25704.

[13] J. L. Hall, M. A. Noca, and R. W. Bailey, "Cost-benefit analysis of the aerocapture mission set," *J Spacecr Rockets*, vol. 42, no. 2, pp. 309–320, 2005, doi: 10.2514/1.4118.

[14] W. J. O'Neil, J. F. Jordan, J. W. Zielenbach, S. K. Wong, R. T. Mitchell, and P. E. Koskela, "Mariner 9 Navigation," no. NASA JPL/TR-32-1586, 1973.

[15] D. T. Lyons, J. G. Beerer, P. Esposito, M. D. Johnston, and W. H. Willcockson, "Mars Global Surveyor: Aerobraking mission overview," *J Spacecr Rockets*, vol. 36, no. 3, pp. 307–313, 1999, doi: 10.2514/2.3472.

[16] J. E. Graf, R. W. Zurek, J. K. Erickson, B. Jai, M. D. Johnston, and R. de Paula, "Status of Mars Reconnaissance Orbiter Mission," *Acta Astronaut*, vol. 61, no. 1–6, pp. 44–51, 2007, doi: 10.1016/j.actaastro.2007.01.032.

[17] G. Falcone, J. W. Williams, and Z. R. Putnam, "Assessment of aerocapture for orbit insertion of small satellites at Mars," *J Spacecr Rockets*, vol. 56, no. 6, pp. 1–15, 2019, doi: 10.2514/1.A34444.

[18] A. Austin *et al.*, "SmallSat Aerocapture to Enable a New Paradigm of Planetary Missions," *2019 IEEE Aerospace Conference*, 2019, doi: 10.1109/AERO.2019.8742220.

[19] G. R. Woodcock and B. Sherwood, "Engineering aerobrakes for exploration missions," *Acta Astronaut*, vol. 21, no. 6–7, pp. 397–404, 1990, doi: 10.1016/0094-5765(90)90057-R.

[20] D. J. Kessler and B. G. Cour-Palais, "COLLISION FREQUENCY OF ARTIFICIAL SATELLITES: THE CREATION OF A DEBRIS BELT.," *J Geophys Res*, 1978, doi: 10.1029/JA083iA06p02637.

[21] D. J. Kessler, "Collisional cascading: The limits of population growth in low earth orbit," *Advances in Space Research*, vol. 11, no. 12, pp. 63–66, 1991, doi: 10.1016/0273-1177(91)90543-S.

[22] D. J. Kessler, N. L. Johnson, J. C. Liou, and M. Matney, "The Kessler Syndrome: Implications to Future Space Operation," *Advances in the Astronautical Sciences*, vol. 137, no. 8, 2010.

[23] J. C. Dolado-Perez, B. Revelin, and R. Di-Costanzo, "Sensitivity Analysis of The Long-Term Evolution of the Space Debris Population in Leo," *Journal of Space Safety Engineering*, vol. 2, no. 1, pp. 12–22, 2015, doi: https://doi.org/10.1016/S2468-8967(16)30035-0.

[24] J.-C. Liou *et al.*, "STABILITY OF THE FUTURE LEO ENVIRONMENT – AN IADC COMPARISON STUDY," in *Proceedings of the 6th European Conference on Space Debris*, 2013. doi: 10.13140/2.1.3595.6487.

[25] J. C. Liou, D. T. Hall, P. H. Krisko, and J. N. Opiela, "LEGEND - A three-dimensional LEO-to-GEO debris evolutionary model," *Advances in Space Research*, vol. 34, no. 5, pp. 981–986, 2004, doi: 10.1016/J.ASR.2003.02.027.

[26] C. Martin, R. Walker, and H. Klinkrad, "The sensitivity of the ESA DELTA model," *Advances in Space Research*, vol. 34, no. 5, pp. 969–974, 2004, doi: https://doi.org/10.1016/j.asr.2003.02.028.

[27] T. J. Muelhaupt, M. E. Sorge, J. Morin, and R. S. Wilson, "Space traffic management in the new space era," *Journal of Space Safety Engineering*, vol. 6, no. 2, pp. 80–87, Jun. 2019, doi: 10.1016/J.JSSE.2019.05.007.

[28] M. D. Hejduk, D. E. Snow, and L. K. Newman, “Satellite Conjunction Assessment Risk Analysis for ‘Dilution Region’ Events: Issues and Operational Approaches,” in *Space Traffic Management Conference 2019*, 2019. [Online]. Available: https://commons.erau.edu/stm

[29] S. Alfano, “A Numerical Implementation of Spherical Object Collision Probability,” *J Astronaut Sci*, vol. 53, no. 1, pp. 103–109, 2005, doi: 10.1007/BF03546397.

[30] K. Alfriend, M. Akella, J. Frisbee, J. Foster, D.-J. Lee, and M. Wilkins, “Probability of Collision Error Analysis,” *Space Debris*, vol. 1, no. 1, pp. 21–35, 1999, doi: 10.1023/A:1010056509803.

[31] N. Bérend, “Estimation of the probability of collision between two catalogued orbiting objects,” *Advances in Space Research*, vol. 23, no. 1, pp. 243–247, Jan. 1999, doi: 10.1016/S0273-1177(99)00009-5.

[32] F. K. Chan, *Spacecraft Collision Probability*. American Institute of Aeronautics and Astronautics, Inc., 2008. doi: 10.2514/4.989186.

[33] J. Foster and H. S. Estes, “A parametric analysis of orbital debris collision probability and maneuver rate for space vehicles,” NASA, National Aeronautics and Space Administration, Lyndon B. Johnson Space Center, Houston, Texas, 1992. Accessed: Feb. 17, 2022. [Online]. Available: https://purl.stanford.edu/dg552pb6632.

[34] R. P. Patera, “General Method for Calculating Satellite Collision Probability,” *Journal of Guidance, Control, and Dynamics*, vol. 24, no. 4, pp. 716–722, Jul. 2001, doi: 10.2514/2.4771.

[35] S. Alfano and D. Oltrogge, “Probability of Collision: Valuation, variability, visualization, and validity,” *Acta Astronaut*, vol. 148, pp. 301–316, Jul. 2018, doi: 10.1016/J.ACTAASTRO.2018.04.023.

[36] A. B. Poore *et al.*, “Covariance and Uncertainty Realism in Space Surveillance and Tracking,” 2016.

[37] E. J. Öpik, "Collision Probabilities with the Planets and the Distribution of Interplanetary Matter," *Proceedings of the Royal Irish Academy. Section A: Mathematical and Physical Sciences*, vol. 54, pp. 165–199, Feb. 1951, [Online]. Available: http://www.jstor.org/stable/20488532

[38] G. W. Wetherill, Wetherill, and G. W., "Collisions in the Asteroid Belt," *J Geophys Res*, vol. 72, no. 9, pp. 2429–2444, May 1967, doi: 10.1029/JZ072I009P02429.

[39] J. Radtke *et al.*, "Revision of Statistical Collision Analysis for Objects Inside of Satellite Constellations," in *Proceedings of the 64th International Astronautical Congress*, Sep. 2013.

[40] J. Radtke, S. Mueller, V. Schaus, and E. Stoll, "LUCA2-AN ENHANCED LONG-TERM UTILITY FOR COLLISION ANALYSIS," in *Proceedings of the 7th European Conference on Space Debris*, 2017.

[41] A. Rossi, L. Anselmo, C. Pardini, R. Jehn, and G. B. Valsecchi, "The new space debris mitigation (SDM 4.0) long term evolution code," in *Proceedings of the 5th European Conference on Space Debris*, Mar. 2009, vol. 5.

[42] A. B. Jenkin, M. E. Sorge, J. P. McVey, G. E. Peterson, and B. Y. Yoo, "MEO Debris Environment Projection Study," in *Proceedings of the 6th European Conference on Space Debris*, Apr. 2013.

[43] A. B. Jenkin, J. P. McVey, and M. E. Sorge, "Assessment of time spent in the LEO, GEO, and semi-synchronous zones by spacecraft on long-term reentering disposal orbits," *Acta Astronaut*, vol. 193, pp. 579–594, 2022, doi: https://doi.org/10.1016/j.actaastro.2021.07.048.

[44] J.-C. Liou, D. J. Kessler, M. Matney, and G. Stansbery, "A New Approach to Evaluate Collision Probabilities Among Asteroids, Comets,and Kuiper Belt Objects," in *34th Annual Lunar and Planetary Science Conference*, Mar. 2003. [Online]. Available: https://ui.adsabs.harvard.edu/abs/2003LPI....34.1828L

[45] X. Wang and J. Liu, "An Introduction to a New Space Debris Evolution Model: SOLEM," *Advances in Astronomy*, vol. 2019, pp. 1–11, May 2019, doi: 10.1155/2019/2738276.

[46] A. Petit, A. Rossi, and E. M. Alessi, "Assessment of the close approach frequency and collision probability for satellites in different configurations of large constellations," *Advances in Space Research*, vol. 67, no. 12, pp. 4177–4192, Jun. 2021, doi: 10.1016/J.ASR.2021.02.022.

[47] H. G. Lewis, S. Diserens, T. Maclay, and J. P. Sheehan, "Limitations of the Cube Method for Assessing Large Constellations," in *First International Orbital Debris Conference*, Dec. 2019, vol. 2109.

[48] S. Diserens, H. G. Lewis, and J. Fliege, "Assessing collision algorithms for the newspace era," *Journal of Space Safety Engineering*, vol. 7, no. 3, pp. 274–281, Sep. 2020, doi: 10.1016/J.JSSE.2020.07.021.

[49] N. Cimmino *et al.*, "Tuning of NASA Standard Breakup Model for Fragmentation Events Modelling," *Aerospace 2021, Vol. 8, Page 185*, vol. 8, no. 7, p. 185, Jul. 2021, doi: 10.3390/AEROSPACE8070185.

[50] H. Peng, X. Bai, H. Peng, and X. Bai, "Recovering area-to-mass ratio of resident space objects through data mining," *AcAau*, vol. 142, pp. 75–86, Jan. 2018, doi: 10.1016/J.ACTAASTRO.2017.09.030.

[51] P. H. Krisko and J. C. Liou, "NASA Long-Term Orbital Debris Modeling Comparison: LEGEND and EVOLVE," in *54th International Astronautical Congress of the International Astronautical Federation, the International Academy of Astronautics, and the International Institute of Space Law*, Sep. 2003. doi: doi:10.2514/6.IAC-03-IAA.5.2.03.

[52] D. A. Vallado and D. Finkleman, "A critical assessment of satellite drag and atmospheric density modeling," *Acta Astronaut*, vol. 95, no. 1, pp. 141–165, Feb. 2014, doi: 10.1016/J.ACTAASTRO.2013.10.005.

[53] M. D. Hejduk and D. E. Snow, "The Effect of Neutral Density Estimation Errors on Satellite Conjunction Serious Event Rates," *Space Weather*, vol. 16, no. 7, pp. 849–869, Jul. 2018, doi: https://doi.org/10.1029/2017SW001720.

[54] S. Casali and W. Barker, "Dynamic Calibration Atmosphere (DCA) for the High Accuracy Satellite Drag Model (HASDM)," in *AIAA/AAS Astrodynamics Specialist Conference and Exhibit*, Aug. 2002. doi: doi:10.2514/6.2002-4888.

[55] J. T. Emmert, H. P. Warren, A. M. Segerman, J. M. Byers, and J. M. Picone, "Propagation of atmospheric density errors to satellite orbits," *Advances in Space Research*, vol. 59, no. 1, pp. 147–165, 2017, doi: https://doi.org/10.1016/j.asr.2016.07.036.

[56] L. Sagnieres and I. Sharf, "Uncertainty Characterization of Atmospheric Density Models for Orbit Prediction of Space Debris," in *7th European Conference on Space Debris*, 2017.

[57] F. Schiemenz, J. Utzmann, and H. Kayal, "Propagation of grid-scale density model uncertainty to orbital uncertainties," *Advances in Space Research*, vol. 65, no. 1, pp. 407–418, 2020, doi: https://doi.org/10.1016/j.asr.2019.10.013.

[58] S. Hilton, F. Cairola, A. Gardi, R. Sabatini, N. Pongsakornsathien, and N. Ezer, "Uncertainty Quantification for Space Situational Awareness and Traffic Management," *Sensors* , vol. 19, no. 20. 2019. doi: 10.3390/s19204361.

[59] C. D. Bussy-Virat, A. J. Ridley, and J. W. Getchius, "Effects of Uncertainties in the Atmospheric Density on the Probability of Collision Between Space Objects," *Space Weather*, vol. 16, no. 5, pp. 519–537, May 2018, doi: https://doi.org/10.1029/2017SW001705.

[60] Y. Hao, S. Zhang, X. Zheng, and J. Qu, "Influence of atmospheric density and area-to-mass errors on orbit prediction accuracy," *J Phys Conf Ser*, vol. 2252, no. 1, p. 12073, 2022, doi: 10.1088/1742-6596/2252/1/012073.

[61] S. J. Casali *et al.*, “Effect of cross-correlation of orbital error on probability of collision determination,” in *AAS/AIAA Astrodynamics Specialist Conference*, 2018, vol. 272.

[62] V. T. Coppola, J. Woodburn, and R. Hujsak, “Effects of cross correlated covariance on space-craft collision probability,” in *AAS/AIAA Spaceflight Mechanics Meeting*, 2004, vol. 181.

[63] R. Peldszus and P. Faucher, “European Union Space Surveillance & Tracking (EU SST): State of Play and Perspectives,” *Space Policy*, vol. 62, p. 101503, 2022, doi: https://doi.org/10.1016/j.spacepol.2022.101503.

[64] E. J. Choi *et al.*, “Performance analysis of sensor systems for space situational awareness,” *Journal of Astronomy and Space Sciences*, 2017, doi: 10.5140/JASS.2017.34.4.303.

[65] P. Faucher, R. Peldszus, and A. Gravier, “Operational space surveillance and tracking in Europe,” *Journal of Space Safety Engineering*, vol. 7, no. 3, pp. 420–425, 2020, doi: 10.1016/j.jsse.2020.07.005.

[66] T. M. Johnson, “SSA Sensor Calibration Best Practices,” in *Proceedings of the Advanced Maui Optical and Space Surveillance Technologies Conference*, 2014.

[67] D. A. Vallado, R. S. Hujsak, T. M. Johnson, J. H. Seago, and J. W. Woodburn, “ORBIT DETERMINATION USING ODTK VERSION 6,” in *4th International Conference on Astrodynamics Tools and Techniques*, 2010.

[68] A. Milani, G. Tommei, D. Farnocchia, A. Rossi, T. Schildknecht, and R. Jehn, “Correlation and orbit determination of space objects based on sparse optical data,” *Mon Not R Astron Soc*, 2011, doi: 10.1111/j.1365-2966.2011.19392.x.

[69] K. Fujimoto and D. J. Scheeres, “Correlation of optical observations of Earth-orbiting objects and initial orbit determination,” *Journal of Guidance, Control, and Dynamics*, 2012, doi: 10.2514/1.53126.

[70] A. D. Jaunzemis, M. J. Holzinger, and K. K. Luu, “Sensor tasking for spacecraft custody maintenance and anomaly detection using evidential reasoning,” *Journal of Aerospace Information Systems*, 2018, doi: 10.2514/1.I010584.

[71] E. Vellutini *et al.*, “Monitoring the final orbital decay and the re-entry of Tiangong-1 with the Italian SST ground sensor network,” *Journal of Space Safety Engineering*, vol. 7, no. 4, pp. 487–501, Dec. 2020, doi: 10.1016/J.JSSE.2020.05.004.

[72] V. Morand, C. Yanez, and J. Dolado, *BAS3E: A framework to Conceive, Design, and Validate Present and Future SST Architectures*. 2019.

[73] I. Urdampilleta Aldama, D. Lubián Arenillas, I. Grande Olalla, and F. Pina Caballero, “MACHINE LEARNING APPLIED TO THE OPTIMIZATION OF SST SENSOR TASKING,” in *Proceedings of the 8th European Conference on Space Debris*, Apr. 2021.

[74] G. Purpura *et al.*, *Development of a Software Suite for Performance Assessment of SST Sensor Networks*. 2021.

[75] P. M. Siew and R. Linares, “Optimal Tasking of Ground-Based Sensors for Space Situational Awareness Using Deep Reinforcement Learning,” *Sensors 2022, Vol. 22, Page 7847*, vol. 22, no. 20, p. 7847, Oct. 2022, doi: 10.3390/S22207847.

[76] G. Purpura, A. de Vittori, R. Cipollone, L. Facchini, P. di Lizia, and M. Massari, *GA-based optimal tasking for SST sensor networks in the SENSIT tool*. 2022.

[77] T. Blake, “Space Domain Awareness (SDA),” in *Advanced Maui Optical and Space Surveillance Technologies Conference*, Sep. 2011, p. E3.

[78] M. Jah, “Space Surveillance, Tracking, and Information Fusion for Space Domain Awareness,” in *NATO STO-EN-SCI-292*, 2016.

[79] E. Blasch, G. Chen, D. Shen, C. C. Insaurralde, and K. Pham, “Space track ontology elements for space domain awareness,” in *Sensors and Systems for*

*Space Applications XV*, Jun. 2022, vol. 12121, p. 121210A. doi: 10.1117/12.2619580.

[80] "SatCen - The Recognized Space Picture (RSP) Display study." https://www.satcen.europa.eu/page/the-recognized-space-picture-rsp-display-study (accessed Jan. 18, 2023).

[81] L. Leveque, "Space Situational Awareness and Recognized Picture," in *Handbook of Space Security: Policies, Applications and Programs*, P. L. and R. J. and M. D. and G. C. Schrogl Kai-Uwe and Hays, Ed. New York, NY: Springer New York, 2015, pp. 699–715. doi: 10.1007/978-1-4614-2029-3_46.

[82] D. Brouwer, "Solution of the problem of artificial satellite theory without drag," *Astron J*, vol. 64, p. 378, Nov. 1959, doi: 10.1086/107958.

[83] Y. Kozai, "Second-order solution of artificial satellite theory without air drag," *Astron J*, vol. 67, p. 446, Sep. 1962, doi: 10.1086/108753.

[84] R. H. Lyddane, "Small eccentricities or inclinations in the Brouwer theory of the artificial satellite," *Astron J*, vol. 68, p. 555, Oct. 1963, doi: 10.1086/109179.

[85] D. A. Vallado and W. D. McClain, *Fundamentals of astrodynamics and applications*, 4th ed. Space Technology Library, 2013.

[86] Y. Kozai, "The motion of a close earth satellite," vol. 64, p. 367, Nov. 1959, doi: 10.1086/107957.

[87] D. Brouwer and G.-I. Hori, "Theoretical evaluation of atmospheric drag effects in the motion of an artificial satellite," vol. 66, p. 193, Jun. 1961, doi: 10.1086/108399.

[88] M. H. Lane and K. H. Cranford, "An improved analytical drag theory for the artificial satellite problem," in *Astrodynamics Conference*, Aug. 1969. doi: doi:10.2514/6.1969-925.

[89] M. H. Lane and F. R. Hoots, "General Perturbations Theories Derived from the 1965 Lane Drag Theory," Dec. 1979.

[90] F. R. Hoots and R. L. Roehrich, "Models for Propagation of NORAD Element Sets," 1980.

[91] F. R. Hoots, P. W. Schumacher, and R. A. Glover, "History of Analytical Orbit Modeling in the U. S. Space Surveillance System," *Journal of Guidance, Control, and Dynamics*, vol. 27, no. 2, pp. 174–185, Mar. 2004, doi: 10.2514/1.9161.

[92] D. Vallado, P. Crawford, R. Hujsak, and T. S. Kelso, "Revisiting Spacetrack Report #3," in *AIAA/AAS Astrodynamics Specialist Conference and Exhibit*, American Institute of Aeronautics and Astronautics, 2006. doi: doi:10.2514/6.2006-6753.

[93] "Space-Track.Org." https://www.space-track.org/ (accessed Mar. 09, 2023).

[94] "CelesTrak." https://celestrak.org/ (accessed Mar. 09, 2023).

[95] D. Oltrogge and J. Ramrath, "Parametric Characterization of SGP4 Theory and TLE Positional Accuracy," in *Advanced Maui Optical and Space Surveillance Technologies Conference*, Sep. 2014, p. E87.

[96] T. S. C. Kelso, "1 AAS 07-127 VALIDATION OF SGP 4 AND IS-GPS-200 D AGAINST GPS PRECISION EPHEMERIDES," 2007.

[97] J. F. San-Juan, I. Pérez, M. San-Martín, and E. P. Vergara, "Hybrid SGP4 orbit propagator," *Acta Astronaut*, vol. 137, pp. 254–260, 2017, doi: https://doi.org/10.1016/j.actaastro.2017.04.015.

[98] D. Vallado and P. Cefola, "Two-line element sets - Practice and use," *Proceedings of the International Astronautical Congress, IAC*, vol. 7, pp. 5812–5825, Jan. 2012.

[99] R. H. Battin, *An Introduction to the Mathematics and Methods of Astrodynamics, Revised Edition*. American Institute of Aeronautics and Astronautics, Inc., 1999. doi: 10.2514/4.861543.

[100] O. Montenbruck and E. Gill, *Satellite Orbits*, vol. 1. 2000. doi: 10.1007/978-3-642-58351-3.

[101] B. A. Jones and R. L. Anderson, "A Survey of Symplectic and Collocation Integration Methods for Orbit Propagation," in *AAS/AIAA SPace Flight Mechanics Meeting*, 2012.

[102] J. Aristoff and A. Poore, "Implicit Runge-Kutta Methods for Orbit Propagation," in *AIAA/AAS Astrodynamics Specialist Conference*, American Institute of Aeronautics and Astronautics, 2012. doi: doi:10.2514/6.2012-4880.

[103] B. K. Bradley, B. Jones, G. Beylkin, and P. Axelrad, "A new numerical integration technique in astrodynamics," *Advances in the Astronautical Sciences*, vol. 143, pp. 1709–1728, Jan. 2012.

[104] M. M. Berry and L. M. Healy, "Implementation of Gauss-Jackson Integration for Orbit Propagation," *J Astronaut Sci*, vol. 52, no. 3, pp. 331–357, 2004, doi: 10.1007/BF03546367.

[105] G. Metris and P. Exertier, "Semi-analytical theory of the mean orbital motion.," *Astron Astrophys*, vol. 294, pp. 278–286, Feb. 1995, [Online]. Available: https://ui.adsabs.harvard.edu/abs/1995A&A...294..278M

[106] P. CEFOLA, "Equinoctial orbit elements - Application to artificial satellite orbits," in *Astrodynamics Conference*, American Institute of Aeronautics and Astronautics, 1972. doi: doi:10.2514/6.1972-937.

[107] D. A. Danielson, B. Neta, and L. W. Early, "Semianalytic Satellite Theory (SST): Mathematical algorithms," Jan. 1994. [Online]. Available: https://ui.adsabs.harvard.edu/abs/1994nps..reptR....D

[108] S. Setty, P. Cefola, O. Montenbruck, and H. Fiedler, "Application of Semi-analytical Satellite Theory Orbit Propagator to Orbit Determination for Space Object Catalog Maintenance," *Advances in Space Research*, vol. 57, Mar. 2016, doi: 10.1016/j.asr.2016.02.028.

[109] B. Cazabonne and P. Cefola, *Towards Accurate Orbit Determination using Semi-analytical Satellite Theory*. 2021.

[110] G. Baù, C. Bombardelli, and J. Pelaez, "Adaptive scheme for accurate orbit propagation," *Journal of Aerospace Engineering, Sciences and Applications*, vol. 4, Apr. 2012, doi: 10.7446/jaesa.0402.02.

[111] G. Baù and C. Bombardelli, "Time elements for enhanced performance of the DROMO orbit propagator," *Astron J*, vol. 148, p. 1, Sep. 2014, doi: 10.1088/0004-6256/148/3/43.

[112] J. Peláez, J. M. Hedo, and P. R. de Andrés, "A special perturbation method in orbital dynamics," *Celest Mech Dyn Astron*, vol. 97, no. 2, pp. 131–150, 2007, doi: 10.1007/s10569-006-9056-3.

[113] D. Amato, C. Bombardelli, G. Baù, V. Morand, and A. J. Rosengren, "Non-averaged regularized formulations as an alternative to semi-analytical orbit propagation methods," *Celest Mech Dyn Astron*, vol. 131, no. 5, p. 21, 2019, doi: 10.1007/s10569-019-9897-1.

[114] G. Baù, J. Hernando-Ayuso, and C. Bombardelli, "A generalization of the equinoctial orbital elements," *Celest Mech Dyn Astron*, vol. 133, no. 11, p. 50, 2021, doi: 10.1007/s10569-021-10049-1.

[115] C. Bombardelli, G. Baù, and J. Peláez, "Asymptotic solution for the two-body problem with constant tangential thrust acceleration," *Celest Mech Dyn Astron*, vol. 110, no. 3, pp. 239–256, 2011, doi: 10.1007/s10569-011-9353-3.

[116] C. Bombardelli, "Analytical formulation of impulsive collision avoidance dynamics," *Celest Mech Dyn Astron*, vol. 118, no. 2, pp. 99–114, 2014, doi: 10.1007/s10569-013-9526-3.

[117] J. Hernando-Ayuso, C. Bombardelli, G. Baù, and A. Martínez-Cacho, "Near-Linear Orbit Uncertainty Propagation Using the Generalized Equinoctial Orbital Elements," *Journal of Guidance, Control, and Dynamics*, pp. 1–12, Dec. 2022, doi: 10.2514/1.G006864.

[118] N. K. Pavlis, S. A. Holmes, S. C. Kenyon, and J. K. Factor, "The development and evaluation of the Earth Gravitational Model 2008 (EGM2008)," *J Geophys Res Solid Earth*, vol. 117, no. B4, p. 4406, Apr. 2012, doi: 10.1029/2011JB008916.

[119] J. T. Emmert, "Thermospheric mass density: A review," *Advances in Space Research*, vol. 56, no. 5, pp. 773–824, 2015, doi: https://doi.org/10.1016/j.asr.2015.05.038.

[120] L. ~G. Jacchia, "New Static Models of the Thermosphere and Exosphere with Empirical Temperature Profiles," *SAO Special Report*, vol. 313, May 1970.

[121] L. ~G. Jacchia, "Revised Static Models of the Thermosphere and Exosphere with Empirical Temperature Profiles," *SAO Special Report*, vol. 332, May 1971.

[122] C. E. Roberts, "An analytic model for upper atmosphere densities based upon Jacchia's 1970 models," *Celestial mechanics 1971 4:3*, vol. 4, no. 3, pp. 368–377, Dec. 1971, doi: 10.1007/BF01231398.

[123] J. M. Picone, A. E. Hedin, D. P. Drob, and A. C. Aikin, "NRLMSISE-00 empirical model of the atmosphere: Statistical comparisons and scientific issues," *J Geophys Res Space Phys*, vol. 107, no. A12, p. SIA 15-1, Dec. 2002, doi: 10.1029/2002JA009430.

[124] L. G. Jacchia, "Thermospheric Temperature, Density, and Composition: New Models," *SAO Special Report*, vol. 375, Mar. 1977, [Online]. Available: https://ui.adsabs.harvard.edu/abs/1977SAOSR.375.....J

[125] B. R. Bowman, W. K. Tobiska, F. A. Marcos, C. Y. Huang, C. S. Lin, and W. J. Burke, "A new empirical thermospheric density model JB2008 using new

solar and geomagnetic indices," in *AIAA/AAS Astrodynamics Specialist Conference and Exhibit*, 2008. doi: 10.2514/6.2008-6438.

[126] J. H. Verner, "Explicit Runge-Kutta Methods with Estimates of the Local Truncation Error," *SIAM J Numer Anal*, vol. 15, no. 4, pp. 772–790, 1978, [Online]. Available: http://www.jstor.org/stable/2156853

[127] V. Schaus, E. M. Alessi, G. Schettino, A. Rossi, and E. Stoll, "On the practical exploitation of perturbative effects in low Earth orbit for space debris mitigation," *Advances in Space Research*, vol. 63, no. 7, pp. 1979–1991, Apr. 2019, doi: 10.1016/J.ASR.2019.01.020.

[128] N. L. Johnson, P. H. Krisko, J. C. Liou, and P. D. Anz-Meador, "NASA's new breakup model of evolve 4.0," *Advances in Space Research*, vol. 28, no. 9, pp. 1377–1384, Jan. 2001, doi: 10.1016/S0273-1177(01)00423-9.

[129] G. Fasano and M. D'Errico, "Modeling orbital relative motion to enable formation design from application requirements," *Celest Mech Dyn Astron*, vol. 105, no. 1, p. 113, 2009, doi: 10.1007/s10569-009-9230-5.

[130] R. Opromolla, G. Fasano, G. Rufino, and M. Grassi, "Design of relative trajectories for in orbit proximity operations," *Acta Astronaut*, vol. 145, pp. 342–356, 2018, doi: https://doi.org/10.1016/j.actaastro.2018.01.062.

[131] B. Reihs, A. Vananti, T. Schildknecht, J. A. Siminski, and T. Flohrer, "Application of attributables to the correlation of surveillance radar measurements," *Acta Astronaut*, vol. 182, pp. 399–415, 2021, doi: https://doi.org/10.1016/j.actaastro.2021.01.059.

[132] T. R. Spilker *et al.*, "Qualitative assessment of aerocapture and applications to future missions," *J Spacecr Rockets*, vol. 56, no. 2, pp. 536–545, 2019, doi: 10.2514/1.A34056.

[133] T. Percy, E. Bright, and A. Torres, "Assessing the Relative Risk of Aerocapture Using Probabilistic Risk Assessment," *41st AIAA/ASME/SAE/ASEE Joint Propulsion Conference & Exhibit*, 2005, doi: 10.2514/6.2005-4107.

[134] Z. R. Putnam and R. D. Braun, “Drag-modulation flight-control system options for planetary aerocapture,” *J Spacecr Rockets*, vol. 51, no. 1, pp. 139–150, 2014, doi: 10.2514/1.A32589.

[135] E. Fantino *et al.*, “The Small Mars System,” *Acta Astronaut*, vol. 137, pp. 168–181, 2017, doi: 10.1016/j.actaastro.2017.04.024.

[136] P. Pasolini *et al.*, “Small Mars satellite: A low-cost system for Mars exploration,” *Proceedings of the 67th International Astronautical Congress (IAC)*, 2016.

[137] R. Savino *et al.*, “IRENE PRELIMINARY STUDY (ITALIAN RE-ENTRY NACELLE PRELIMINARY STUDY),” *10TH INTERNATIONAL PLANETARY PROBE WORKSHOP*, 2013, doi: 10.1067/mmt.2003.21.

[138] M. Iacovazzo, V. Carandente, R. Savino, and G. Zuppardi, “Longitudinal stability analysis of a suborbital re-entry demonstrator for a deployable capsule,” *Acta Astronaut*, vol. 106, pp. 101–110, 2015, doi: 10.1016/j.actaastro.2014.10.014.

[139] A. Fedele, R. Gardi, and G. Pezzella, “Aerothermodynamics and thermal design for on-ground and in-flight testing of a deployable heat shield capsule,” *CEAS Space Journal*, vol. 12, no. 3, pp. 411–428, 2020, doi: 10.1007/s12567-020-00312-w.

[140] A. Fedele and S. Mungiguerra, “Aerodynamics and flight mechanics activities for a suborbital flight test of a deployable heat shield capsule,” *Acta Astronaut*, vol. 151, pp. 324–333, 2018, doi: https://doi.org/10.1016/j.actaastro.2018.05.044.

[141] R. D. Braun and R. M. Manning, “Mars exploration entry, descent, and landing challenges,” *J Spacecr Rockets*, vol. 44, no. 2, pp. 310–323, 2007, doi: 10.2514/1.25116.

[142] A. M. Cassell *et al.*, "ADEPT, A Mechanically Deployable Re-Entry Vehicle System, Enabling Interplanetary CubeSat and Small Satellite Missions," in *Small Satellite Conference*, 2018.

[143] E. Venkatapathy *et al.*, "Adaptive deployable entry and placement technology (ADEPT): A feasibility study for human missions to mars," in *21st AIAA Aerodynamic Decelerator Systems Technology Conference and Seminar 2011*, 2011. doi: 10.2514/6.2011-2608.

[144] S. P. Parvathi and R. v. Ramanan, "Direct transfer trajectory design options for interplanetary orbiter missions using an iterative patched conic method," *Advances in Space Research*, vol. 59, no. 7, pp. 1763–1774, 2017, doi: 10.1016/j.asr.2017.01.023.

[145] M. A. Hapgood, "Space physics coordinate transformations: A user guide," *Planet Space Sci*, vol. 40, no. 5, pp. 711–717, 1992, doi: 10.1016/0032-0633(92)90012-D.

[146] B. A. Archinal *et al.*, "Report of the IAU Working Group on Cartographic Coordinates and Rotational Elements: 2009," *Celest Mech Dyn Astron*, vol. 109, pp. 101–135, 2011, doi: 10.1007/s10569-010-9320-4.

[147] C. G. Justus *et al.*, "Mars-GRAM 2000: A Mars atmospheric model for engineering applications," *Advances in Space Research*, vol. 29, no. 2, pp. 193–202, 2002, doi: 10.1016/S0273-1177(01)00569-5.

[148] C. G. Justus and D. L. Johnson, "Mars Global Reference Atmospheric Model (Mars-GRAM) Version 2001: Users Guide," no. NASA/TM-2001-210961, 2001.

[149] C. G. Justus, "Mars global reference atmospheric model for mission planning and analysis," *J Spacecr Rockets*, vol. 28, no. 2, pp. 216–221, 1991, doi: 10.2514/3.26233.

[150] C. G. Justus, A. L. Duvall, and D. L. Johnson, “Global MGS TES data and Mars-GRAM validation,” *Advances in Space Research*, vol. 35, no. 1, pp. 4–7, 2005, doi: 10.1016/j.asr.2003.02.044.

[151] D. de la Torre Sangrà, “Study of the Martian environment for application to the design of a greenhouse,” Polytechnic University of Catalonia (UPC), 2014.

[152] M. Alexander, “Mars transportation environment definition document,” no. NASA/TM-2001-210935, 2001.

[153] C. G. Justus and R. D. Braun, “Atmospheric Environments for Entry, Descent and Landing (EDL),” *5th International Planetary Probes Workshop and Short Course*, 2007.

[154] F. Forget *et al.*, “Density and temperatures of the upper Martian atmosphere measured by stellar occultations with Mars Express SPICAM,” *Journal of Geophysical Research E: Planets*, vol. 114, no. E1, 2009, doi: 10.1029/2008JE003086.

[155] J. R. Cruz and J. S. Lingard, “Aerodynamic decelerators for planetary exploration: Past, present, and future,” *AIAA Guidance, Navigation, and Control Conference 2006*, 2006, doi: 10.2514/6.2006-6792.

# List of publications

## Journal papers

- G. Isoletta, M. Grassi, E. Fantino, D. de la Torre Sangrà, J. Peláez, "Feasibility study of aerocapture at Mars with an Innovative Deployable Heat Shield", Journal of Spacecraft and Rockets 2021, Vol. 58, Num. 6 (https://doi.org/10.2514/1.A35016)
- N. Cimmino, G. Isoletta, R. Opromolla, G. Fasano, A. Basile, A. Romano, M. Peroni, A. Panico, and A. Cecchini, "Tuning of NASA Standard Breakup Model for Fragmentation Events Modelling.", Aerospace 2021, 8, 185 (**https://doi.org/10.3390/aerospace8070185**)
- G. . Isoletta, R. Opromolla, G. Fasano, "Uncertainty-aware Cube algorithm for medium-term collision risk assessment", Advances in Space Research, Vol. 71, pp. 539-555, 2023 (https://doi.org/10.1016/j.asr.2022.09.017)

## Conference papers

- G. Isoletta, M. Grassi, E. Fantino, J. Peláez, "Analysis of Mars aerocapture with a deployable drag device", in Proceedings of 71st International Astronautical Congress (IAC), The CyberSpace edition, 12-14 October 2020
- G. Isoletta, C. Lombardi, R. Opromolla, G. Fasano, M. Peroni, A. Panico, A. Cecchini, A. Romano, A. Basile, W. Matta, "Metrological Characterization of Ground-based Sensors for Space Surveillance and Tracking," in Proceedings of the 2021 IEEE 8th International Workshop on Metrology for AeroSpace (MetroAeroSpace), 2021, pp. 585-590 (https://doi.org/10.1109/MetroAeroSpace51421.2021.9511662)
- V. Porrino, A. Argirò, M. Chiariello, A. Contaldi, A. Cristiano, L. D'Albenzio, B. De Leonardis, C. Di Mauro, F. J. Fernàndez Fernàndez, M. Gargiulo, R. Guida, C. R. Ibello, G. Montano, L. Zennamo, G. Isoletta, A. Nocerino, A. Renga, "SCORE: a scientific mission for the exploration of

a long period comet with micro/nano satellites”, in Proceedings of the AIDAA 2021 XXVI International Conference

- L. Falanga, G. Caso, A. Ciccarelli, F. Cuomo, S. De Masi, F. Della Vecchia, D. Di Maio, S. Gala, S. Piatti, A. Saveriano, M. Scamardella, D. Scilla, R. Tarone, A. Renga, G. Isoletta, A. Nocerino. “A Microsatellite mission to a long-period comet in a heliocentric inner orbit”, in Proceedings of the AIDAA 2021 XXVI International Conference
- G. Isoletta, N. Cimmino, R. Opromolla, G. Fasano, A. Romano, A. Basile, O. Pesacane, M. Peroni, A. Panico, A. Cecchini, “Orbital propagation challenges and solutions for SST fragmentation services”, in Proceedings of the 72nd International Astronautical Congress (IAC), Dubai, 25-29 October 2021
- G. Isoletta, N. Cimmino, R. Opromolla, G. Fasano, “Uncertainty Evaluation Tool for Medium-Term Low-Earth Orbit Propagation”, in Proceedings of the 73$^{rd}$ International Astronautical Congress (IAC), Paris (France), 18-22 September 2022
- N. Cimmino, G. Isoletta, R. Opromolla, G. Fasano, “Performance and Sensitivity Analysis of Machine Learning-based Approaches for Resident Space Object Characterization”, 73rd International Astronautical Congress (IAC), Paris, 18-22 September 2022

# Acknowledgments

Scrivere dei ringraziamenti significa andare a pescare dei momenti, degli attimi che, in qualche modo, hanno reso unico il percorso.

E le persone spuntano in quegli attimi,
nei ricordi appaiono i loro volti.

Ecco, ad esempio, il chiasmo l'ho studiato a scuola, certo, ma alla fine me l'ha insegnato Guccini cosa fosse davvero, quando ero effettivamente pronto per comprenderlo. Il chiasmo è mettere in discussione, non accontentarsi di una sola versione dei fatti, cambiare il punto di vista, è la ricerca di un'alternativa. Credo di essere riuscito a fare mio questo insegnamento inconsapevole e spero di essere riuscito a portarlo anche in questo mio percorso. Questo per dire che conta tanto l'inclinazione personale, ma contano altrettanto i Maestri e il contesto, e a questi ultimi vanno i miei ringraziamenti.

Ringrazio innanzitutto i miei tutor, Roberto e Giancarmine, non solo per la qualità e la quantità di insegnamenti tecnici ed accademici, ma anche e soprattutto per la vostra profonda umanità e per avermi trasmesso dei valori che vanno ben oltre la formazione accademica, tra i quali spiccano la cultura del lavoro e l'onestà intellettuale. Lavorare con voi è stimolante e divertente al contempo (talvolta anche un po' stressante, ma tutto ok). Grazie di tutto.

Un grande ringraziamento va poi a tutto il gruppo dei Sistemisti e in particolare a Michele, Alfredo e Daniela per i tanti momenti di confronto e di "goliardia" durante i pranzi assieme al Sesto Piano.

Ringrazio poi tutti i miei colleghi dottorandi passati e presenti tra Tecchio e Via Claudio (un grazie alla regina Federica per ringraziare di conseguenza anche tutti i suoi sudditi), la mia assegnista preferita Flavia, e i borsisti, anche chi è passato da qui solo per pochi mesi.

Dedico poi un ringraziamento speciale a tre "colleghi": ad Alessia, con la quale ho condiviso questo percorso dall'inizio alla fine e, in verità, condivido le aule universitarie da tempo immemore ormai, grazie per i confronti e gli sfoghi reciproci; a Marco, nel quale ho trovato un amico profondo e sincero, oltre che un competente ricercatore, un fantastico musicista, un accanito lettore, e una vasta gamma di aggettivi+sostantivi che comunque non basterebbero a descriverti; a Nicola, mio caro compagno di "attività varie" in questi anni, tra progetti, ricerca, supporto ai tesisti, lavorare (e chiacchierare…) con te è sempre un grande piacere.